UC San Diego
UC San Diego Electronic Theses and Dissertations

Title

Investigating the effect of mechanical forces on invertebrate development and behavior

Permalink

https://escholarship.org/uc/item/9g18s3sx

Author

Goel, Tapan

Publication Date

2022

Peer reviewed|Thesis/dissertation

UNIVERSITY OF CALIFORNIA SAN DIEGO

Investigating the effect of mechanical forces on invertebrate development and behavior

A dissertation submitted in partial satisfaction of the
requirements for the degree
Doctor of Philosophy

in

Physics with specialization in Quantitative Biology

by

Tapan Goel

Committee in charge:

Eva-Maria S. Collins, Chair
Patrick H. Diamond, Co-Chair
Wouter-Jan Rappel
Karl Willert

2022

The dissertation of Tapan Goel is approved, and it is acceptable in quality and form for publication on microfilm and electronically.

University of California San Diego

2022

DEDICATION

To Dada, Dadi, Nana and Nani

TABLE OF CONTENTS

LIST OF FIGURES

LIST OF TABLES

ACKNOWLEDGEMENTS

As a teenager, I completely bought into the myth of the lone genius. Scientists were older men (of course they were men) who sat in imposing leather chairs in dark rooms surrounded by books. They would think hard about ideas, have epiphanies on the regular and write them down for mere mortals to understand, sometimes centuries into the future. These last six years have summarily rid me of this false notion.

I have been lucky to be surrounded by some incredibly generous and kind people who for some miraculous reason saw me worthy of their time, effort and expertise. Foremost among them is my advisor, Eva-Maria. I came to her with only my enthusiasm for biological physics and zero wet lab experience. She still agreed to take me on and train me in doing all the things I needed to do to conduct research in the lab. And then, two years later, when I walked into her office to tell her that I could not and did not want to do wet lab work anymore, she worked with me so that I could switch to more data driven and computational work. She has been my mentor, guide, teacher, friend, boss, tormentor and supporter these past six years. Her work ethic, kindness and optimism will always be an inspiration for me.

I also owe an unpayable debt of gratitude to Pat. He has invested deeply in my success since I first took his class as a incoming grad student. He used to mark out portions of books from his personal library and give them to me to better understand what he was teaching in class. I will cherish that forever. He has taught me how to get rid of the clutter and ask the simple but important questions while dealing with scientific problems. He has also generously guided me through the professional aspects of being a scientist. I do not have the right words but suffice to say, Pat is one of main reasons I've been able to finish graduate school.

Many thanks to my dissertation committee members, past and present, for their valuable feedback through the course of my PhD - Dr. Massimo Vergasolla, Dr. Jeremie Palacci, Dr. Wouter-Jan Rappell and Dr. Karl Willert.

I've had the privilege to work with some amazing people in the Collins lab: Rui, Danielle,

Everyone needs role models. I have mine: Dr. Sameer Agarwal, Dr. Shyam Sunder and Dr. Vishwesha Guttal. Thank you for setting an example and for your timely advice.

Last but most important: my family. I love you.

Chapter 2, in full, is a reprint of the material with minor edits, as it appears in: Goel T., Ireland D., Shetty V., Diamond P.H., Collins E-M.S., "Let it rip: the mechanics of self-bisection in asexual planarians determines their population reproductive strategies", *Physical Biology*, 19 (1), 016002, (2021). The dissertation author was the co-primary author of this paper.

Chapter 3, in full, is a reprint of the material with minor edits, as it appears in: Wang R., Goel T., Khazoyan K. Sabry Z., Quan H.J., Diamond P.H., Collins E-M.S.,"Mouth function determines the shape oscillation pattern in regenerating *Hydra* tissue spheres", *Biophysical Journal*, 117 (6), 1145-1155, (2019). The dissertation author was the co-primary author of this paper.

Chapter 4, in full, is currently being prepared for submission for publication of the material: Goel T., Adams E., Tran C.M., Martin S., Diamond, P.H., Collins E-M.S.,"Non-linear elastodynamics of *Hydra* mouth opening". The dissertation author is the primary author of this paper.

Appendix A, in full, is a reprint of the material with minor edits, as it appears in: Goel T., Wang R., Martin S., Lanphear E., Collins E-M. S.,"Linalool acts as a fast and reversible anesthetic in *Hydra*", *PLoS one*, 14(10), e0224221, (2019). The dissertation author was the co-primary author of this paper.

VITA

2012-2016	B. S. in Physics (Minor: Biology), Indian Institute of Science, Bangalore, India
2016-2022	Graduate Teaching Assistant, University of California San Diego
2016-2022	Ph. D. in Physics with specialization in Quantitative Biology, University of California San Diego

PUBLICATIONS

Stowell N.C., Goel T., Shetty V., Noveral J., Collins E-M. S., "Quantitative planarian behavior as an introduction to object tracking and signal processing", *The Biophysicist*, 2 (3), 1-17, (2021).

Goel T., Ireland D., Shetty V., Rabeler C., Diamond P.H., Collins E-M.S., "Let it rip: the mechanics of self-bisection in asexual planarians determines their population reproductive strategies", *Physical Biology*, 19(1), 016002, (2021).

Goel T., Wang R., Martin S., Lanphear E., Collins E-M.S., "Linalool acts as a fast and reversible anesthetic in *Hydra*", *PloS one*, 14(10), e0224221, (2019).

Wang R., Goel T., Khazoyan K., Sabry Z., Quan H.J., Diamond P.H., Collins E-M.S., "Mouth function determines the shape oscillation pattern in regenerating *Hydra* tissue spheres", *Biophysical Journal*, 117(6), 1145-1155, (2019).

ABSTRACT OF THE DISSERTATION

Investigating the effect of mechanical forces on invertebrate development and behavior

by

Tapan Goel

Doctor of Philosophy in Physics with specialization in Quantitative Biology

University of California San Diego, 2022

Eva-Maria S. Collins, Chair
Patrick H. Diamond, Co-Chair

Mechanical forces play a fundamental role in shaping biological structure and function. They set limits to length and timescales for these processes. In turn, the dynamical response of biochemical signalling pathways and genetic circuits to these mechanical forces create feedback loops that lead to interesting non-linear effects on the stress-strain relationship of biological materials. In this dissertation, I present three studies on the consequences of these complex feedback loops at the population, organismal and tissue levels over timescales ranging from months to hours to minutes.

In chapter 2, we use live imaging to compare and contrast the kinematics of self bisection in three different planarian species. We show how they used body shape changes and substrate adhesion to generate the stresses necessary to overcome the ultimate tensile strength of the tissue. We also show how mechanical constraints affect resource allocation to the offspring produced by this self bisection process and develop predictive models to relate the number and size of the offspring to the size of the parent.

In chapter 3, we use gain-of-function and loss-of-function experiments to show how a transition in the period and amplitude of osmotically driven shape oscillations in regenerating *Hydra* tissue spheres is caused by the formation of an actively regulated mouth structure.

In chapter 4, we use a combination of experiments and mathematical modelling to study the dynamics of mouth opening in *Hydra*. We show how mechanical nearest-neighbor coupling can be sufficient to generate long range order over long timescales from underlying short range stochastic forces. We also show how anharmonic elasticity affects can modulate the long range order of the deformation and its timescale in non-intuitive ways.

In appendix A, we develop the chemical linalool as a powerful, reversible anesthetic that can be for imaging *Hydra* and performing surgical manipulations on them. We characterize the activity of the linalool, tested it for its short term and long term health effects on the animals and validated its utility in imaging and surgical applications.

Together, these studies show how non-linear effects produced by the interplay of bio-chemical signalling, shape changes and mechanical stresses lead to a range of complex dynamical patterns and behaviors in biological systems.

Chapter 1

Introduction

In his seminal work, 'On Growth and Form' [1], D'Arcy Wentworth Thompson argued that mechanical forces are the primary factors shaping biological structures. For instance, Thompson showed how the physics of deformable fluid filled cavities dictates the shape of eggs - spherical ones for owls and ellipsoidal ones for pelicans. He argued why surface tension must governs the shape of cells in aggregates and in isolation. He explained how scaling relationships between surface area and volume might set limits on the size of animals, why smaller animals can carry weights much larger than their own and why the hummingbird is capable of stationary flight while the albatross is not. Drawing on examples from across the tree of life, across scales of length and time, Thompson showed how the shape and function of living things are governed by the same mechanical principles that govern the structure and motion of inanimate objects [2, 3]. In fact, he claimed that these principles were the main determinants of the form and function of living things.

During the century since the publication of his work, we have developed a much more sophisticated view of the factors that shape life. We now understand that the structure and physiology of living matter are products of the interplay between heredity, gene regulation, biochemical signaling and mechanical forces. I focus specifically on how coupling between

mechanical strain and biochemical reaction-diffusion systems affects biology.

Reaction-diffusion systems typically involve two or more types of particles that react with each other locally and diffuse through space at different rates. Alan Turing famously showed how a simple reaction-diffusion system consisting of two cross-reacting chemical 'morphogens' diffusing at different rates through tissue could generate stable (Turing) patterns [4]. Depending on the geometry of the tissue, reaction rates and diffusion constants of the morphogens, Turing showed how the system could generate a variety of patterns - spots on a leopard's coat, stripes on a zebra and rings on a cat's tail. Mathematically, these systems can are represented by a set of coupled partial differential equations of the type:

$$\frac{\partial a_i}{\partial t} = f_i(a_1, a_2....., a_n) + D_i \nabla^2 a_i \tag{1.1}$$

where a_i is the concentration of the i-th morphogen, f_i is a function that encapsulates the production and chemical interactions between the morphogens, serving as a source/sink term and D_i is the diffusion constant of the ith species.

To understand how such patterns are generated, consider a two-morphogen system where morphogen A activates the production of itself and of morphogen B while morphogen B inhibits the production of A. Let us assume also that B diffuses faster than A. Such a system might be described the following equations:

$$\frac{\partial A}{\partial t} = \kappa_{AA}A - \kappa_{AB}B + D_A \nabla^2 A \tag{1.2a}$$

$$\frac{\partial B}{\partial t} = \kappa_{BA}A + D_B \nabla^2 B \tag{1.2b}$$

Here, κ_{pq} denote positive reaction rates and $D_A < D_B$ denote diffusion constants of A and B respectively. To begin with, let us assume that the distribution of the morphogens is

homogeneous. Furthermore, assume that the morphogens are at local equilibrium with each other. Consider a fluctuation at some point in space that leads to an increase in the local concentration of A. This will lead to further local increase in the concentration of A and, the concentration of B. As a result, the morphogens will start diffusing into their surroundings. Since B diffuses away faster than A, it will not significantly suppress the local production of A near the source of the fluctuation. Further away from the source however, the concentration of B will increase due to diffusion but the concentration of A will not increase as much, since A diffuses slowly. As a result, a region of high concentration of A will form near the source of the fluctuation with a region of high concentration of B surrounding it (Figure 1.1). Multiple such local fluctuations, depending on the specific reaction rates, diffusion constants and tissue geometry, can generate the variety of patterns alluded to in the preceding paragraph.
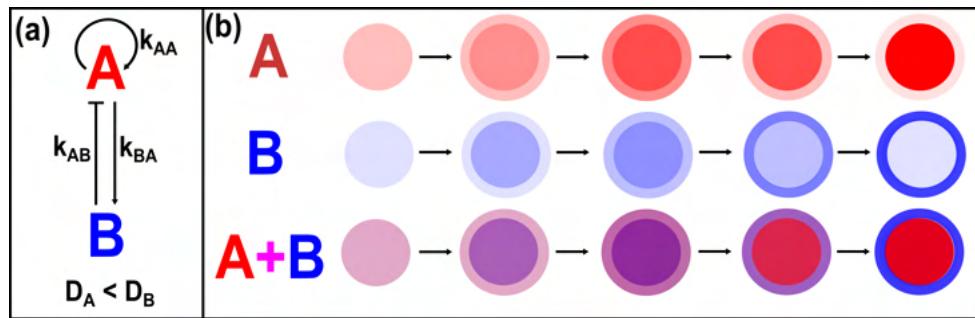
Figure 1.1: Formation of a Turing pattern (a) Schematic of the reaction diffusion system described by eq. 1.2. 'A' self activates and activates 'B'. 'B' inhibits 'A'. 'B' diffuses faster than 'A'. (b) Changes in the concentrations of A (top), B (middle) and A+B combined (bottom) over time as described by eq. 1.2. The color intensity is a proxy for concentration. Note the formation of central spot of 'A' surrounded by an annulus of 'B' in the final pattern.

More recent work has shown how 'Turing patterns' created by such reaction-diffusion systems, coupled with mechanical stress-strain response, are important for embryonic development [5, 6], tumor growth [7, 8] and other biological processes [9, 10]. This coupling can be due to tissue strain affecting the diffusion constants or the morphogen production/reaction rates. For example: (1) tissue strain changes the shape of the tissue (and therefore the metric of the surface) over which the morphogens are diffusing, effectively changing their local diffusion

constant(s) [11]. This leads to modifications of the morphogen patterns which then have downstream implications for local cell size, shape and fate. (2) Cadherin molecules, which sense and transmit tension between cells, affect recruitment and activation of downstream proteins that manage the ATP budget of individual cells [12]. Among other things, the change to the ATP budget slows actin polymerization, changing cytoskeletal structure. The change in cytoskeletal structure changes the stiffness of individual cells and that of the tissue as a whole. Note how this mechanism also links tissue level mechanical stress to intracellular biochemical regulation.

I present three studies in this dissertation that look at different ways in which the coupling of reaction diffusion systems and mechanical stresses affect biological function. We used two different freshwater invertebrates - *Hydra* and planarians - in these studies. Both are famous for their ability to regenerate completely from small tissue fragments. This allowed us to perform a range of *in vivo* surgical manipulations that would be impossible to do in other commonly used model organisms. Furthermore, their small size and aquatic habitat make pharmacological manipulations easy. Thus, we were able to use a range of tools to dissect the relationship between mechanics and biology without having to resort to more artificial systems like tissue culture.

In chapter 1, we used planarian fission to understand how tissue mechanics sets constraints on decisions that also depend on chemical reaction-diffusion patterns. Planarians reproduce asexually by splitting themselves transversally along one or more division planes using only substrate traction and their own musculature. Each of the segments so created, regenerate into new adults. The survival and reproductive success of these new adults has been shown to depend on the biomass allocated to them as a result of the location of the division plane(s) [13]. The survival and reproductive success of the individuals in turn affects the overall growth and survival of the population. This system presents two important problems: (1) How do planarians accomplish this feat of self-bisection and, (2) what sets the location of the division planes. These problems are of interest in soft tissue mechanics and population biology.

While the first problem has remained largely untouched in recent years, the second problem has attracted attention from biologists. The solutions proposed rely on the diffusion driven graded expression of certain biochemicals such as Wnt, TGFβ and Hox proteins [14, 15]. More recently, an attempt was made to explain experimental observations of the timing and biomass allocation during self-bisection using a Turing-pattern type mechanism [16]. However, in the absence of reliable candidate molecules for the mechanism and experimental measurements, it was not possible to constrain the model parameters to a biologically and physically reasonable range.

Using time-lapse imaging and mechanical perturbations, we observed different mechanisms by which planarians self-bisect (Figure 1.2) and obtained bounds on the positions of the division planes. We identified three distinct phases of the self bisection process. Across the species, we observed key differences in morphological changes associated with each phase, leading to differences in how the necessary tensile stress is generated. We also found important similarities - prior to division, each species creates a narrow waist region flanked by adhesion patches that stick to the substrate. The constriction of the waist serves to amplify the tensile stress produced by muscles to overcome the tensile strength of the tissue in the waist region. Using mechanical perturbation experiments, we also show that the planarians are able to modulate their substrate traction. Based on these mechanical processes and anatomical constraints set by the stiffness of the pharynx, we obtained upper and lower bounds in the location of the division plane across the species. These bounds limit the number and size of the offspring each individual can produce and consequently, the average survival and reproductive rates of the species. We also verified that these constraints are consistent with the observed differences in the population dynamics of the three species. More generally, this study links individual level mechanical behavior on minute to hour long timescales (self-bisection) with population level behavior on weeks to month long timescales (population dynamics). Our study shows that while we cannot discount the role of a reaction diffusion mechanism in deciding where

planarians divide, mechanical factors set reliable constraints on this decision.
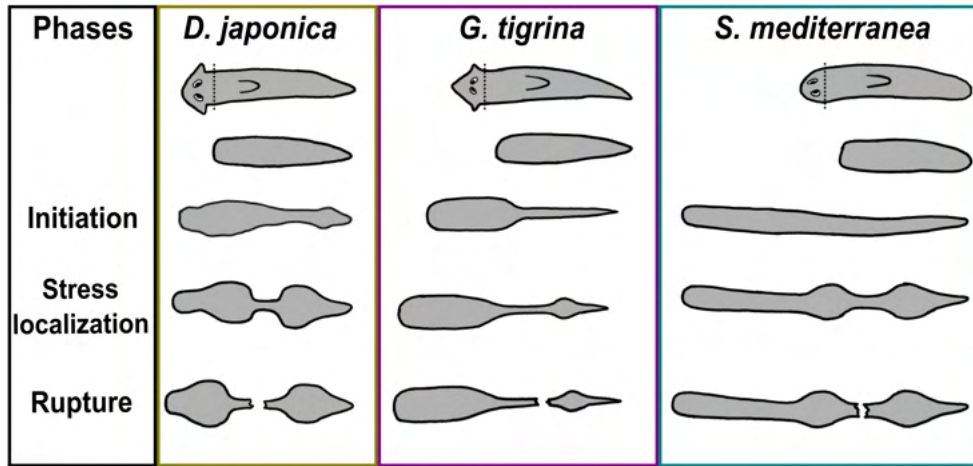
Figure 1.2: Phases of planarian self-bisection Schematic shows the main phases of self bisection for three planarian species: *Dugesia japonica* (left), *Girardia tigrina* and *Schmidtea mediterranea* (right). Planarians were decapitated to increase the likelihood of self bisection. Figure adapted from [17].

In chapter 2, we used body axis formation in *Hydra* to understand how mechano-chemical coupling at short length scales affects mechanical response at the tissue level. *Hydra* is centimeter long freshwater cousin of the jellyfish (Figure 1.3). It can regenerate completely from a small piece of tissue. The tissue piece first rounds up into a hollow sphere. The sphere undergoes osmotically driven cycles of gradual swelling and abrupt shrinking (shape oscillations). Over the course of several cycles, the tissue sphere breaks shape symmetry, first becoming ellipsoidal and then a cylinder (Figure 1.4). Concurrently, diffusion of morphogens on the evolving tissue surface also leads to the formation of biochemical patterns on the tissue sphere, generating an inhomogeneous concentration profile. The inhomogeneous concentration profile breaks the symmetry of the biochemical pattern. This symmetry breaking event has been associated with an abrupt transition in the period and amplitude of the shape oscillations.

Several models have been developed that couple the mechanisms of chemical and mechanical symmetry breaking in *Hydra*. The most recent of these is by Mercker *et al* [19]. The model involves a reaction diffusion system consisting of a short range activator morphogen
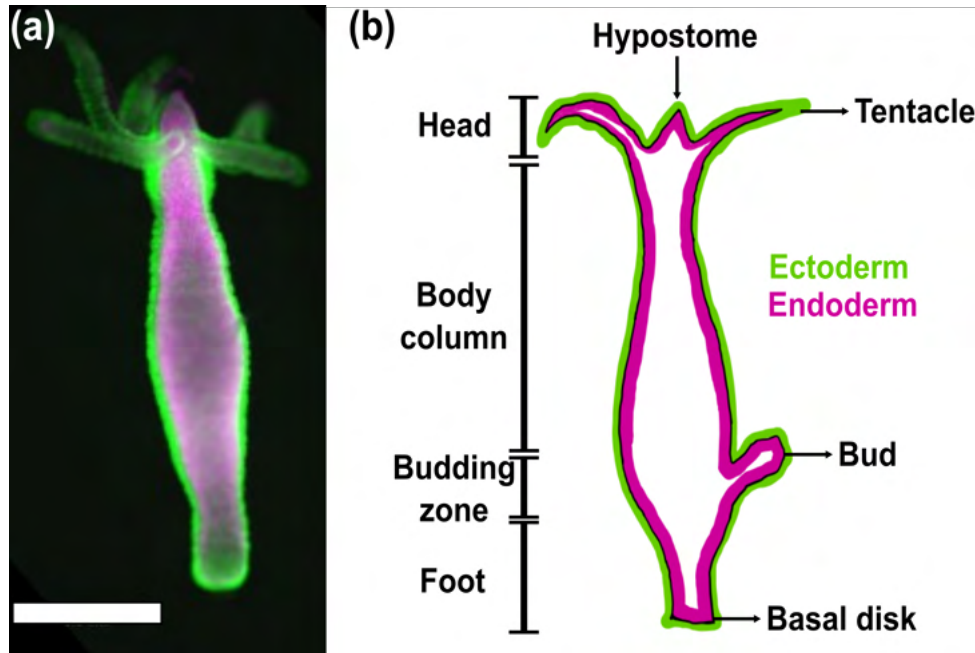
Figure 1.3: Basic anatomy of *Hydra* (a) Image of fluoresently labelled *Hydra*. Ectoderm is labelled with GFP (green) and endoderm is labelled with DsRed2 (red). Scale bar: 500 μm (b) Diagram showing basic anatomy of *Hydra*. Figure adapted from [18].

(shown to be the Wnt molecule in *Hydra* [20]) and a long range inhibitor morphogen (as yet undetermined), similar to one proposed by Gierer and Meinhardt [21]. The Mercker model treats the regenerating *Hydra* tissue sphere as a visco-elastic, hollow, fluid filled shell. The shell deforms under the action of osmotic pressure, with the morphogens diffusing on this evolving surface. They propose that an increase in the concentration of the activator leads to a decrease in the stretch stiffness of the tissue, while the stretching of the tissue increases the diffusion constant of the inhibitor. A small increase in activator concentration makes the tissue more compliant. As a result it stretches more in response to osmotic pressure. The increased strain causes the inhibitor to diffuse away more quickly leading to an increase in the activator concentration. Thus a positive feedback loop is established between the concentration of the activator and tissue strain. This loops amplifies small perturbations to the activator causing the initially spherical tissue sphere to become ellipsoidal over time. Mercker *et al* showed that their model reproduces the experimentally observed swelling-rupture cycles but fails to explain the

observed relationship between the time of the transition in the oscillations and the size of the sphere.
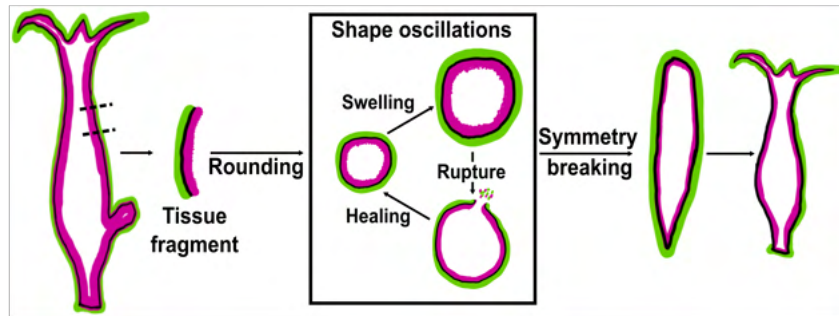
Figure 1.4: Shape oscillations during *Hydra* regeneration A tissue piece excised from the body column of a *Hydra* first rounds up into a hollow sphere. The sphere undergoes shape oscillations until it breaks symmetry to form an ellipsoid and eventually an adult animal. Figure adapted from [18].

We showed experimentally, how the transition in the period and amplitude of the swelling-rupture cycles is actually caused by the development of a significant physiological function, namely, the ability to actively regulate mouth opening. This oscillation pattern transition had previously been assumed in the Mercker model and others to be a signature of the time of symmetry breaking. Once the regenerating animal is able to actively control mouth opening, it can vent fluid built-up in the lumen before the tissue ruptures, effectively reducing the maximum osmotic pressure the tissue can withstand. This in turn reduces the size to which the sphere expands before rupture, producing the small amplitude, high frequency shape oscillations. Our results suggest that symmetry breaking actually happens earlier than the transition of amplitude and period in the shape oscillations. This study sets important constraints on mechano-chemical models of tissue regeneration in *Hydra* and calls into question previous metrics that have been used to validate theoretical models.

In chapter 3, we used *Hydra*'s mouth opening response to understand the role of non-linear elasticity in chemo-mechanically coupled systems. *Hydra* feeds itself by ripping open a hole in its epithelium and ingesting its prey. The hole - "mouth" - is up to ten cell diameters wide and is generated in the span of a minute before closing back up. This large, symmetric

deformation of the tissue is produced by active forces produced by the contraction of short supra-cellular actin fibers. We showed that these forces are short range and uncorrelated over short timescales.
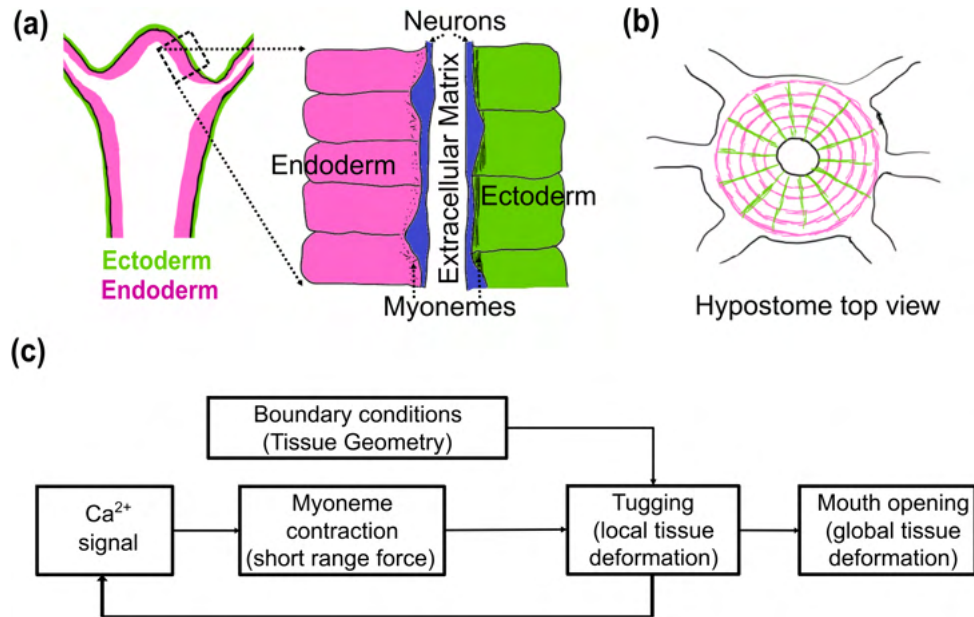
Figure 1.5: Key elements of *Hydra* mouth opening (a) Schematic cross section of the hypostome tissue: ectoderm in green, endoderm in magenta. Neurons in blue. (b) Myoneme arrangement as seen in a top-down view of the hypostome. (c) Flow chart shows the feedback loop between calcium signaling, active force generation and epithelial tissue deformation during mouth opening.

In a recent paper, Wang *et al* modelled the mechanics of *Hydra* epithelium using hyperelastic model coupled to a reaction diffusion mechanism for a Ca^{2+} signal that leads to the generation of active forces [22]. The Ca^{2+} is assumed to be the result of neuronal signaling. While the model presents a useful framework to understand how long range order is generated from short range forces in the context of locomotion in *Hydra*, it suffers from having too many undetermined parameters.

In Chapter 3, we developed a much simpler model of the epithelial tissue to show how elastic coupling between nearest neighbors alone - in the absence of the Ca^{2+} signaling mechanism - can produce long range order, and how non-linear elasticity modules the macroscopic

dynamics of tissue deformation. Using loss-of-function experiments, we showed that the nervous system is not necessary to coordinate the mouth opening process. To perform these experiments, we developed a new non-toxic, easy to use, fast acting and reversible anesthetic tool called linalool. We characterized its long term and short term effects on *Hydra* health. We also demonstrated its usefulness in long term and short term imaging experiments. We directly compared linalool to currently used anesthetics in the field and showed its superior performance. We reported this tool, its effects and uses in a journal article [23]. The article is presented here in Appendix A.

To further understand the dynamics of mouth opening, we developed a simple computational model of the mouth tissue consisting of a 2-D network of anharmonic springs (to mimic the composite of the tissue layers) subject to stochastic, independent, external forces (mimicking the forces generated by the myonemes). We demonstrated that (constrained by experimentally obtained parameter values) this model is able to reproduce experimentally observed mouth area, opening time and degree of mouth symmetry. The nearest neighbor interaction creates a cascade effect which generates the characteristic logistic shape of the observed mouth area-time curve. The model shows how elastic nearest neighbor coupling is sufficient to coordinate mouth opening and produce a symmetric deformation.

The model also manifests the non-intuitive role of strain stiffening in generating larger global deformation and modulating the timescale of mouth opening. Strain stiffening is the phenomenon whereby tissues become stiffer as they become more stretched. This is attributed to an effect similar to the coil-stretch transition of the cytoskeletal polymers due to tissue deformation. We find that strain stiffening allows for larger forces to be transmitted from the boundary of the mouth tissue to its center, thereby generating larger mouth openings. As the tissue stretches, the increase in effective stiffness also reduces the visco-elastic relaxation timescale of the tissue. This effect makes mouth opening faster.

In the specific context of *Hydra*, our model provides a useful null model to understand

the role of the reaction-diffusion of the Ca^{2+} signal in the biomechanics of the epithelial tissues. More generally, the study shows how simple mechanical interaction between cells can generate large, coordinated deformations of tissue from short range stochastic forces in biological systems. It also shows how a non-linear elastic stress-strain relationship affects the length and timescales of tissue deformation.

While all three studies are concerned with systems involving chemo-mechanical coupling, they are very different in scope and scientific approach. They address different length and time scales. Chapter 1 ties together individual level, second-to-minute timescale processes to population level, weeks-to-month long processes. Chapter 2 addresses how cellular level, minute timescale processes affect tissue level, hours long processes. Chapter 3 shows how forces acting over a few milliseconds and over a few cell diameters are coordinated to produce tissue level deformations at the second timescale.

These studies also involve very different research approaches. Chapter 1 is largely an observational study. We used imaging data to quantitatively describe the self bisection process. We combined this information with existing anatomical knowledge to set theoretical bounds on the location of the division plane, which we then verified using observational data about the population statistics of the planarian species. Chapter 2 is an experimental study. We formulated clear hypotheses about the role of mouth development in causing the transition in the shape oscillation pattern. We then used gain-of-function and loss-of-function experiments to test these hypotheses. Chapter 3 uses a combination of observational, experimental and computational methods to ascertain the role of non-linear elasticity in coordinating the *Hydra* mouth opening response. We used imaging data to obtain length and timescales for the active forces, loss-of-function experiments to figure out the the role of the nervous system and computational models to understand the role of non-linear elasticity.

Despite the differences in approach and scales, these studies serve to illuminate how chemo-mechanical coupling affects biological function.

Chapter 2

Let it rip: The mechanics of self-bisection in asexual planarians determines their population reproductive strategies

2.1 Abstract

Asexual freshwater planarians reproduce by transverse bisection (binary fission) into two pieces. This process produces a head and a tail, which fully regenerate within 1-2 weeks. How planarians split into two offspring - using only their musculature and substrate traction – is a challenging biomechanics problem. We found that three different species, *Dugesia japonica*, *Girardia tigrina* and *Schmidtea mediterranea*, have evolved three different mechanical solutions to self-bisect. Using time lapse imaging of the fission process, we quantitatively characterize the main steps of division in the three species and extract the distinct and shared key features. Across the three species, planarians actively alter their body shape, regulate substrate traction, and use their muscles to generate tensile stresses large enough to overcome the ultimate tensile strength of the tissue. Moreover, we show that how each planarian species divides dictates

how resources are split among its offspring. This ultimately determines offspring survival and reproductive success. Thus, heterospecific differences in the mechanics of self-bisection of individual worms explain the observed differences in the population reproductive strategies of different planarian species.

2.2   Introduction

Freshwater planarians – famous for their regenerative potential – are free-living, soft bodied invertebrates [24]. Their slender body structure (length   3-30 mm, width   1-2 mm and height   0.3-0.5 mm) leads to a large surface area-to-volume ratio, allowing planarians to function without a circulatory system: oxygen is absorbed through the body wall and nutrients are absorbed via a muscular feeding tube (pharynx) in the mid-region of the body that connects to an extensive digestive tract [24]. Like many other soft bodied animals, they maintain their body shape via a dense network of circular, longitudinal and diagonal muscle fibers and hydrostatic pressure from internal fluids [25].

Some species of freshwater planarians reproduce asexually by ripping themselves transversally into a head and a tail piece, which then regenerate the missing body parts. How planarians self-bisect – using only their musculature and substrate traction – is an intriguing biomechanics problem that even sparked the interest of Michael Faraday [26]. However, study of this behavior has been hindered by its experimental inaccessibility. There are no known inducers of planarian division and the time between divisions (reproductive waiting time (RWT)) can range from a few days to many months (Table **??**), making it impossible to predict when a planarian will divide. Moreover, planarians will abort the division process upon any type of disturbance. Therefore, many studies have focused on the population level to gain insights into planarian reproductive dynamics [13, 27–31].

Long-term population studies have revealed that how planarians split up their body and

allocate biomass among their offspring determines the offspring's survival and reproductive success. Previous work has shown that *Dugesia japonica* (J-planarians), *Schmidtea mediterranea* (S-planarians) and *Girardia tigrina* (G-planarians) allocate resources differently among their offspring (Table 2.1, area at birth). Interestingly, area at birth – not area at division – determines offspring survival outcomes and population growth dynamics [13, 30]. J-planarians reproduce ("fission") approximately once every month. Both offspring types have narrow distributions of RWTs, with the larger head offspring dividing on average twice as fast as tail offspring. Both offspring have negligible death rates [13]. In contrast, S-planarians display wide RWT distributions for both head and tail offspring, with tail offspring dividing on average only once every 2.5 months. S-planarian offspring death rates are significantly higher than J-planarian offspring death rates [13]. The dramatic head/tail differences in RWTs and mortality rates are a consequence of the reproductive strategy of S-planarians. The majority of S-planarians "fragment": individuals produce one or more trunk (middle piece) offspring within 5 days after the first division – i.e., before regeneration is complete (Figure 2.8). These middle pieces are comparable to tail offspring in size and reproductive behavior [27]. Finally, G-planarians display a third strategy: They allocate their resources primarily to the head offspring [13]. This allows the head offspring to divide the most rapidly of all 3 species (on the order of once every 2 weeks). This rapid reproduction comes at the cost of small tail offspring with the highest death rates (Table 2.1). Notably, the population reproductive strategies of J- and G-planarians have previously been described using mixed models of timer, adder, and sizer strategies [30]. Moreover, while population growth rates are affected by feeding frequency [28], population density and competition between species [13], these parameters do not change the underlying mode of division or the relative biomass allocation among offspring.

Two recent studies on the mechanism of self-bisection of J-planarians [32] and S-planarians [15] have used large-scale, long-term imaging to record self-bisection. They found that these two species split using different biomechanical mechanisms. J-planarians use rhyth-

mic pulsations of the anterior end to create longitudinal stress in the waist. Using traction force measurements, Malinowski *et al* showed that two opposing traction forces act to generate a tensile stress in the waist, on the order of 2000 Pa immediately before rupture [32]. The rupture location for J-planarians was found to be determined by the position of the pharynx and by substrate friction [32]. Arnold *et al* showed that S-planarians elongate to create tension in the waist and proposed that in S-planarians the division plane is pre-specified through the existence of mechanical weak spots that can be identified via mechanical compression. These "compression planes" are distributed equidistantly along the head-tail axis [15]. Their number and spacing is influenced by Hox gene expression patterns [14]. The spacing between compression planes was found to be independent of S-planarian length, but the number of compression planes was positively correlated with length. This theory can explain the observations that S-planarian tail offspring length appears to be independent of parent length [15] and that larger S-planarians tend to make more offspring [27]. However, this is impossible to test directly as observation of compression planes requires killing the planarian.

Given that J- and S-planarians have similar tissue mechanics and are both limited by the same constraints of using only their musculature and substrate adhesion to divide, we found it surprising that they have evolved such different solutions to tear themselves apart. Because S-, J- and G-planarian species differ in their reproductive strategies [13], we hypothesized that each species had evolved a distinct mechanism of self-bisection tailored to their unique reproductive strategies. To test this, we first characterized and quantified how individual planarians of the three species self-bisect at unprecedented spatial and temporal resolution. This provided the first quantitative description of the kinematics of G-planarians self-bisection and the necessary quantitative parameters of S-planarian self-bisection, which were lacking in previous studies.

We observed key differences in how the tensile stress required for division is generated in each species. However, we also identified two conserved features that are indispensable for planarian self-bisection: (1) the formation of a local constriction, or "waist", to amplify the

tensile stress and (2) the formation of adhesion patches anterior and posterior to the waist to prevent slipping and to maintain stress in the waist. Using a simple biomechanical argument and experimental data, we can predict where the waist forms in J- and G-planarians and demonstrate how anatomical constraints can explain why these species rarely fragment. Our results link the minute-long individual-level mechanics of planarian division to the generational, weeks-long reproductive behavior of the population. We show that how individual planarians self-bisect can explain much of the reproductive strategies of the different planarian species.

2.3   Materials and Methods

2.3.1   Planarian maintenance

Clonal asexual *Dugesia japonica* (J-planarians), *Schmidtea mediterranea* (S-planarians), or *Girardia tigrina* (G-planarians) were used for all experiments. Planarians were stored in Tupperware containers in the dark in a temperature-controlled Panasonic incubator at 20℃. J- and G-planarians were kept in $0.5\,\mathrm{g\,L^{-1}}$ Instant Ocean Salts (Spectrum Brands, Blacksburg, VA, USA). S-planarians were kept in 1x Montjuic salts [33]. The solution used for each respective species will be referred to as "planarian water" and can be considered equivalent media. It has previously been shown that using slightly different planarian water formulations does not change the fission dynamics of J-planarians [32]. Planarians from all species were fed organic beef liver from a local farm 1-2 times per week. Worms were cleaned 2 h and again 2 days after feeding and starved for at least 5 days before being used for experiments.

2.3.2   Experimental considerations

Planarian self-bisection is difficult to study due to the different time scales involved in the process. The timescale of interest for investigating the mechanics of self-bisection (as shown in this study) ranges from 0.1 s (to study tissue rupture) to tens of minutes (to study

elongation and waist formation). However, as shown in Table 2.1, reproduction naturally occurs on average only about 1 in 20 days, with some worms not dividing for months, making it impossible to predict when a given planarian will divide. The long timescales prevent us from physically constraining planarians and waiting for division, as worms would get sick under such conditions and no longer divide. Thus, we monitored and recorded hundreds of planarians that were freely moving around in a few cm wide arenas (see section 2.3.3) for several months to obtain the reproductive events that were quantified here. This setup meant that we could not simultaneously image dividing planarians from the top and the side to get volumetric measurements. From separate side and top view recordings, we made assumptions and simplifications of the planarian body shapes. Because these assumptions were made for all 3 species, these do not change the relative differences. Furthermore, we continuously recorded at high frame rates and resolution, generating terabytes of data, because attempts to use body shape changes to detect the onset of division were not fruitful. There are no known inducers of planarian self-bisection. However, planarians were decapitated, because decapitation has been reported to increase the likelihood of division in the presence of light [34] and a brain is not necessary for self-bisection. Cuts were performed with a clean razor blade perpendicular to the head–tail axis and as close to the head as possible. No differences were observed in the division dynamics between intact and decapitated animals (Movies S1- S3). Therefore, we will use the term 'head' to denote the anterior end for both decapitated and intact specimen. Because planarians cease to divide upon the slightest disturbance, they cannot be manipulated directly. If disturbed, self-bisection comes to an abrupt halt, and depending on where in the process the disturbance occurs, can result in a plastic deformation of the body at the site where division would have occurred (Figure 2.9(a)). Contrary to older claims of contact inhibition preventing division [35–38], we found that in all three species physical contact with conspecifics did not prevent division (Figure 2.9(b-d)). So, recording was done at low density conditions so that overlapping planarians did not obstruct tracking of individuals' division dynamics.

2.3.3   Video recording of reproduction

Videos of reproduction events were recorded similar to (10) using either a Flea3 USB3 or a Grasshopper USB3 camera (FLIR Systems Inc., Wilsonville, OR), mounted on ring stands and controlled by a custom MATLAB 2019a (MathWorks, Natick, MA, USA) script. Images were recorded at 7-10 frames per second (fps). Three to four experimental setups were run in parallel, each containing 2-4 planarians, depending on the size of the arena (wells of 6-well plates, 30 mm petri dishes, contact lens containers [39], or Polydimethylsiloxane (PDMS) blocks [32]. For high-resolution imaging of rupture, we used 2 planarians in contact lens containers (Wohlk Contactlinsen GmbH, Schonkirchen, Germany). Planarians were replaced after division or at least every week. The wells were replenished with planarian water twice every day to account for evaporation loss. Total water exchanges happened at least 1x/week.

Lengths and areas of various regions in dividing planarians were quantified from the video recordings using built-in tools (thresholding, analyze particles, skeletonize) in the Fiji distribution of ImageJ [40]. The widths of various parts of the worm – adhesion patches, waist, resting width – were measured manually using the line tool (Figure 2.10(a)). Because the waist region is thinner than neighboring regions, it is easily identified via its shape and its higher pixel brightness values. In contrast, adhesion patches were identified as darker tissue regions (lower pixel values due to increased tissue density [32]) immediately anterior and posterior to the waist that did not start moving immediately before or after waist rupture was complete.

Custom MATLAB scripts were used to measure the body lengths and areas of the planarians during division as functions of time. The scripts and corresponding documentation are available at https://github.com/Collinslab-swat/LetItRip. Briefly, the images of the worms were first binarized by thresholding grayscale values. The centerline and center of mass of the binarized image were identified using standard MATLAB functions. The head and tail along the centerline were defined manually for the first image and then tracked using a nearest neighbor algorithm in successive images. The shape of the worm was parameterized as the distance

between points on the centerline to their respective nearest points on the boundary of the worm. These steps were applied to each image, using nearest neighbor tracking to track a single individual.

2.3.4 Imaging S-planarian offspring post-reproduction

Planarians were maintained individually in 100 mm plastic petri dishes (Simport Scientific) in approximately 25 mL planarian water and fed and cleaned as described in section 2.3.1. Planarians were imaged individually 0-3 days post-division in their respective dishes using a Leica stereo microscope (Leica Microsystems, Wetzlar, Germany) equipped with a Flea3 USB3 camera (FLIR Systems Inc.) and Pointgrey software.

2.3.5 Stickiness assay

On Day 0, planarians (approx. 0.5-2 cm length) of each species were loaded into 48-well plates (Genesee Scientific, San Diego, CA) such that each well contained one planarian and 200 μL of planarian water. Relative differences in substrate adhesion ("stickiness") were tested by shaking the plate using a fixed rotation speed (452 rotations per minute (rpm) for 3 s) on an orbital shaker (Big Bear Automation, Santa Clara, CA) similar to in [41]. The plate was imaged from above by a Flea3 USB3 camera mounted on a ring stand and imaged at 20 fps. Each individual planarian was manually scored as either "unstuck" (displaced by the water flow) or "stuck" (not displaced). Planarians which were dead, on the side of the well, or not visible were not scored and excluded from the analysis. After stickiness was assayed on Day 0, the plates were either stored (control) or agitated on an orbital shaker (see section 2.3.6) for 3 days. Stickiness was assayed again on Day 3. Each species and condition were tested in 3 separate plates with n = 24-48 per plate. These data were analyzed in two ways: 1) to compare stickiness between the three species and 2) to compare, within each species, how stickiness changed due to the incubation on the orbital shaker. To compare the stickiness across the three

species, we calculated the percentage of control planarians of each species that remained stuck to the substrate after shaking. Thus, populations with a larger percentage of adhered worms were considered "stickier". These population-level comparisons were done with the control populations on Day 3 as G-planarians had much fewer adhered worms when first placed into the multi-well plates (Figure 2.11), possibly due to disruption to the mucus during pipetting.

To compare how stickiness changed due to incubation on the orbital shaker within each species, we scored individual planarians as stuck or unstuck on Day 0 (D0) and Day 3 (D3). We were able to track individual planarians since they were loaded into the 48-well plates with only one worm per well. Thus, to express the change in stickiness over time, each worm was classified as either having increased stickiness (D3>D0, i.e., unstuck on D0 and stuck on D3), decreased stickiness (D3<D0, i.e., stuck on D0 and unstuck on D3) or having the same stickiness on both days (D3=D0, i.e., stuck/stuck or unstuck/unstuck). Statistical significance between groups was determined using a Fisher's exact test comparing the number of planarians with increased stickiness vs the number of planarians with decreased or unchanged stickiness on Day 3 compared to Day 0.

2.3.6   Centrifugal force experiments

Individual intact planarians were placed in single wells of a tissue culture treated 6-well plate (Genesee Scientific), with each well containing approximately 3 mL planarian water and one planarian. For each experiment, planarians of comparable size (approx. 1-1.5 cm length) were used. Centrifugal forces were introduced using a Spindrive orbital shaker platform (SP Bel-Art, Wayne, NJ, USA) on a magnetic stirrer. The angular speed of the shaker in rpm was determined using a video recording of the motion with a cell phone camera. Shaking was performed in the dark. The plates were checked every 2-3 days for divisions and divided planarians were exchanged with intact ones. Planarian water was exchanged at least once a week. Planarians were continuously kept on the shaker for a maximum of 3 weeks. Offspring,

defined as all the pieces in the dish including the anterior most segment, were imaged in a 100 mm petri dish using a Vividia Andonstar HM-302 digital microscope (Oasis Scientific Inc, Taylors, SC, USA). The offspring were allowed to stretch out and glide before imaging. The areas and lengths of the individual offspring were quantified in Fiji [40]. The images were cropped to isolate the worm offspring of interest, converted to greyscale and thresholded to identify the worm from the background. Areas were then measured using the analyze particles tool and lengths were measured using the segmented line tool. If thresholding was not possible, the polygon tool was used. The parent area was calculated as the sum of the offspring areas. For each speed setting (J-planarians: 0, 70 and 100 rpm, G-planarians: 0, 100, 120 and 140 rpm, and S-planarians: 0, 100 and 120 rpm), a new set of planarians was used.

2.3.7 Predicting number of offspring

J-planarian offspring were imaged using a Leica stereo microscope (Leica Microsystems) with a Basler A601f CCD camera (Basler AG, Ahrensburg, Germany) and Basler Pylon Viewer. G-planarian offspring resulting from a fission were imaged as in section 2.3.6. The location of the pharynx was determined manually, and the area of the offspring was divided into pre-pharyngeal, pharyngeal, and post-pharyngeal areas (Figure 2.10(b)). To predict whether a G-planarian would fragment or not, the post-pharyngeal area of the head offspring was measured. If this area was greater than 25% of the area of the head offspring, we assumed that this head offspring could fragment.

For J-planarians, we assumed that the worms could fragment if the area of the head offspring was above an absolute minimum area. This minimum cutoff area was estimated from head offspring areas of fragmentation events. From imaging data of trunk and tail offspring of J-planarians, we found that the trunk offspring area scales with the tail offspring area. Based on this scaling relationship, we estimated the size of a theoretical trunk offspring for J-planarians which underwent fission. This theoretical trunk area was subtracted from the area of the fission

head offspring to estimate the size of the theoretical final head offspring resulting from a second division. This theoretical head offspring area must exceed the cutoff head offspring area to permit fragmentation (Figure 2.12). S-planarian offspring from fissions and fragmentations were imaged as in section 2.3.4. To predict the number of offspring an S-planarian could produce, we divided the parent worm area by the average area of the tail offspring and compared it to the actual observed number of offspring of the same S-planarians.

2.3.8   Data analysis

Data from video recordings and centrifugal force experiments were analyzed using MATLAB 2021a (MathWorks, Natick, MA, USA). Linear regressions were conducted using the fitlm function in MATLAB. Statistical tests were conducted using inbuilt MATLAB functions. Parameters obtained from linear fits and normally distributed data are reported as mean $\pm$ standard deviation and compared using the 2-sample t-test (ttest2 in MATLAB). All other parameters and non-normal data are reported as median (25th percentile, 75th percentile) and compared using the Wilcoxon rank sum test which is equivalent to the Mann Whitney U-test (ranksum in MATLAB). Root mean squared errors were calculated as described in supplementary methods. For measurements of lengths and areas during fission in *D. japonica*, data published in [32] were also used in addition to new measurements made as described in the preceding sections. Population data such as RWTs of head and tail offspring, and their areas at birth, previously published in [13] was also used in addition to our newly acquired data.

2.4   Results

2.4.1   The kinematics of planarian division

Using video recording at unprecedented spatial and temporal resolution, we observed the details of how individual planarians of the three species (J-, G-, and S-planarians) self-

bisect. Across species, the tensile stress needed for rupture is created through elongation and amplified using local constriction. Asexual reproduction can be divided into 4 phases (Figure 2.1): Rest (Phase 0); Initiation (Phase 1); Stress Localization, with a distinct hourglass shape (waist formation; Phase 2); and Rupture (Phase 3). We will briefly summarize how each species divides and then compare the different mechanisms for each phase.

J-planarians

As previously shown [32], J-planarians begin to form a waist-like constriction in Phase 1 (Figure 2.1(bi)), mediated by contraction of circular muscles. Waist formation is completed during Phase 2 and is accompanied by the appearance of wide adhesion patches – regions of tissue contact with the substrate – anterior and posterior to the waist. Longitudinal pulsations of the head then build tensile stress in the waist [32]. The head experiences large length changes of about 40% during the pulsations [32], which generates the longitudinal stress in the waist that is necessary for rupture [32]. In Phase 3, the waist ruptures once the longitudinal stress exceeds the ultimate tensile strength of the tissue, and division is complete.

G-planarians

While division in G-planarians shares key steps with J-planarian division, it displays unique features (Figure 2.1(a)): To initiate division (Phase 1), G-planarians constrict their posterior to form a thin tail, giving them a popsicle-like appearance (Figure 2.1(bii)). Similar to J-planarians, this constriction is achieved through active contraction of circular muscles, because G-planarians maintain this shape while gliding. During Phase 2, a short section of the thinned posterior adheres to the substrate while the wider anterior continues to move forward, forming a waist region. Head pulsations are not observed. Instead, once a part of the anterior also adheres to the substrate, the tissue in the waist ruptures rapidly.

S-planarians

As described in [14, 15], S-planarian division relies on extreme longitudinal extension (Figure 2.1(biii)). While the other two species initiate division by local constriction, S-planarians initiate division by extending their anterior forward while keeping the tail in place. Elongation is followed by waist formation in Phase 2. The head continues to extend while the adhesion patches remain stationary. This extension builds tensile stress, which is amplified by the constriction of the waist, eventually leading to rupture in Phase 3. The kinematics of S-planarian division are the same for divisions producing tail and trunk offspring, suggesting that, for all practical purposes, trunks and tails can be treated the same.

2.4.2 Phase 1: Initiation

J- and G-planarians initiate division by forming a local constriction (Figure 2.2(a-b)). In J-planarians, the constricted region begins to resemble the distinctive hourglass shape of the future waist (Figure 2.2(a)). In contrast, G-planarians initially constrict almost the entire posterior, assuming a popsicle-like shape (Figure 2.2(b)). J-planarians form the constriction at $69\% \pm 7\%$ (mean $\pm$ standard deviation) and G-planarians at $66\% \pm 9\%$ of their body length along the anterior-posterior (A-P) axis (Figure 2.2(a-b)). The constricted region will become the waist in Phase 2. Thus, where J- and G-planarians divide and how they allocate resources between offspring is constrained and specified at the onset of fission. In contrast, S-planarians do not constrict during Initiation (Figure 2.2(c)). Instead, S-planarians elongate to almost twice their rest length (Figures S2.13 and 2.7). This is achieved through a "crawling" motion consisting of successive series of adhesion and de-adhesion (Figure 2.14(a)). This is often accompanied by the formation of undulations where portions of the tissue rise off the substrate (Figure 2.14(a)), previously called "contortions" [14]. A-P directed peristaltic waves have been observed concomitantly with the formation of these undulations [14]. Peristalsis [42] is induced by
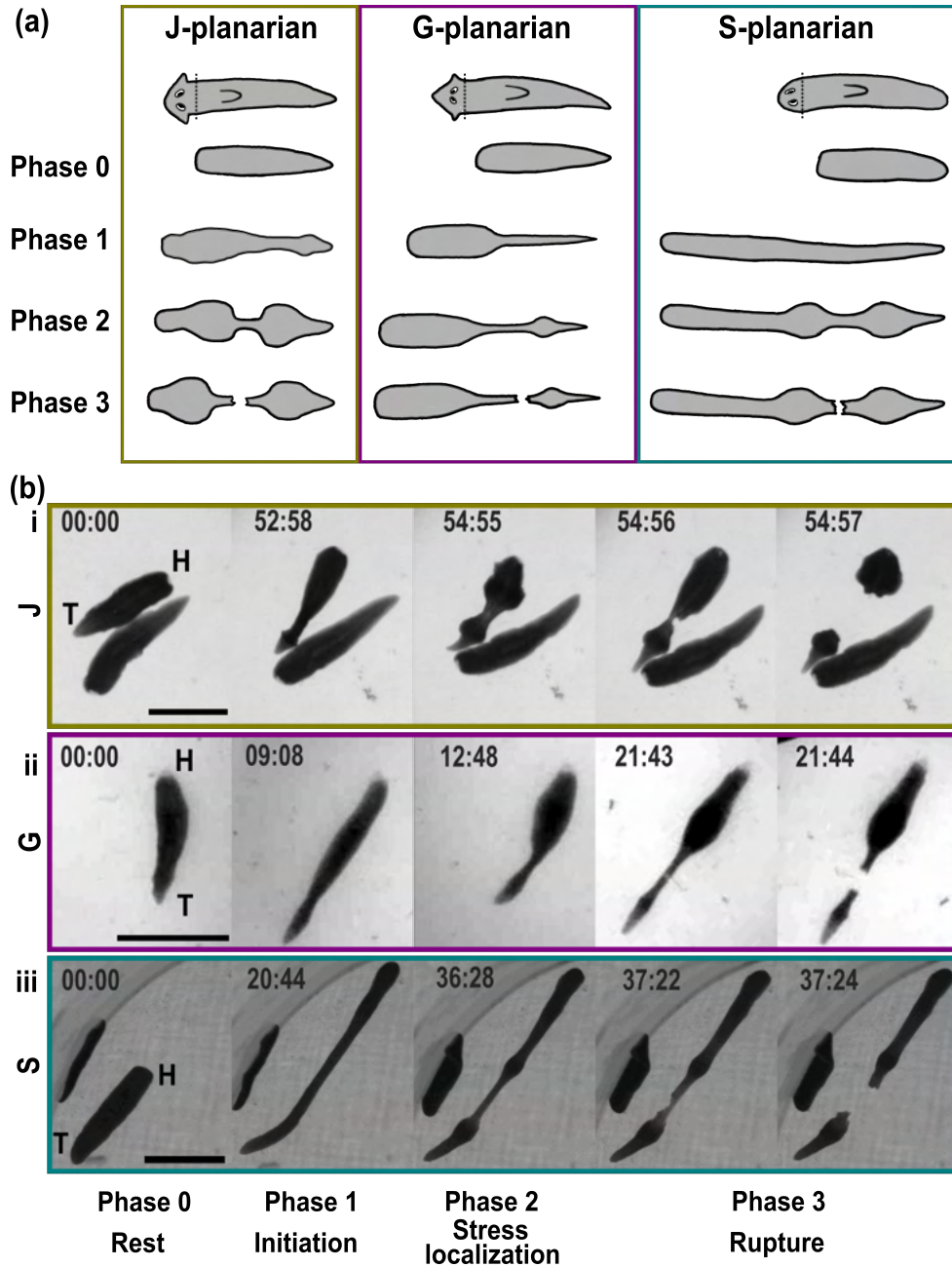
Figure 2.1: Overview of the division process in J-, G- and S-planarians. (a) Schematic comparing the main phases of division in the 3 species. We decapitated the planarians to increase the likelihood of division in the presence of light. Anterior is to the right. (b) Example image sequences of the phases of division in (i) J-planarians, (ii) G- planarians and (iii) S-planarians. Scale bar: 5 mm. H: head, T: tail. Time stamps are minutes: seconds.

compression of planarian longitudinal muscles. Therefore, we suspect that these undulations are

a result of the planarian body buckling under compressive forces generated by the longitudinal

muscles. The S-planarian elongation process follows a characteristic sigmoidal time course (Section 2.7.2, Figure 2.13). J- and G-planarians do not elongate (Figure 2.14(b, c)).
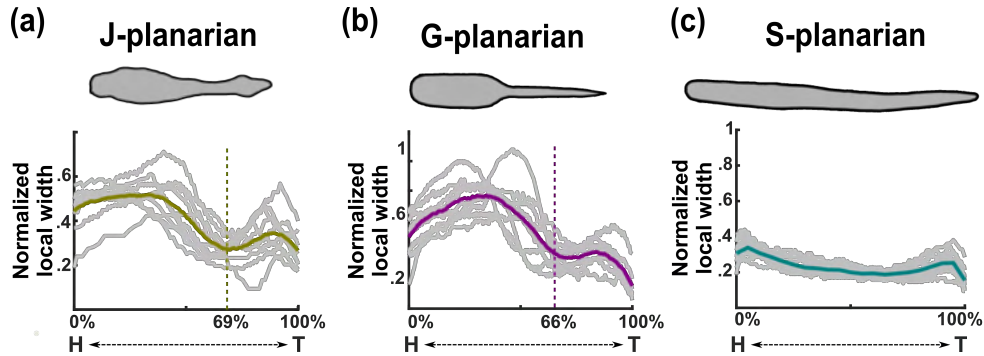
Figure 2.2: Phase 1 – Initiation. (a-b) Local width, normalized to the rest width, along the normalized length of the planarian for a) J-planarians (n=10), b) G-planarians (n=9) and c) S-planarians (n=13). Data for individual planarians are shown as grey lines. The average is shown as a green, magenta, and blue line for (a), (b) and (c), respectively. Dotted lines denote the local minimum normalized width, averaged over all gray curves. Note that S-planarians do not create a local minimum.

2.4.3   Phase 2: Stress Localization

Waist formation is critical to self-bisection. It localizes and amplifies tensile stress through the large difference in cross-sectional area between the narrow waist and the wide adhesion patches. The adhesion patches pull on either side of the waist, generating tensile stress in the waist. In turn, the adhesion patches feel a tensile force due to the waist, balanced by the friction between the substrate and the adhesion patches, which sets the upper limit to the tension force that the adhesion patches can exert on the waist. While the magnitude of the tension force is the same for the (posterior) adhesion patch and the waist, the smaller cross-sectional area of the waist means that it experiences a larger stress. This increased stress due to the same tension force is quantified by a multiplicative stress amplification factor, calculated from the ratio of the cross-sectional areas of the adhesion patch and the waist (Supplementary methods). Estimates of the stress amplification factor (Figure 2.3 and Figure 2.15(a-c)) were similar for S- and G-planarians ($p > 0.05$, unpaired 2-tailed t-test) but significantly higher in J-planarians (p

< 0.01, unpaired 2-tailed t-test). However, the ultimate tensile strength of the waist - estimated from the product of the stress amplification factor and the linear strain (Supplementary methods) – is not statistically different across the three species (J-planarians: 3.2 ± 2.7, G-planarians: 3.2 ± 1.7 and S-planarians: 5.3 ± 2.0 (mean $\pm$ root mean squared error), p > 0.05, 2-tailed t-test). It is expected that the species have similar tensile strengths, given their similar tissue properties.
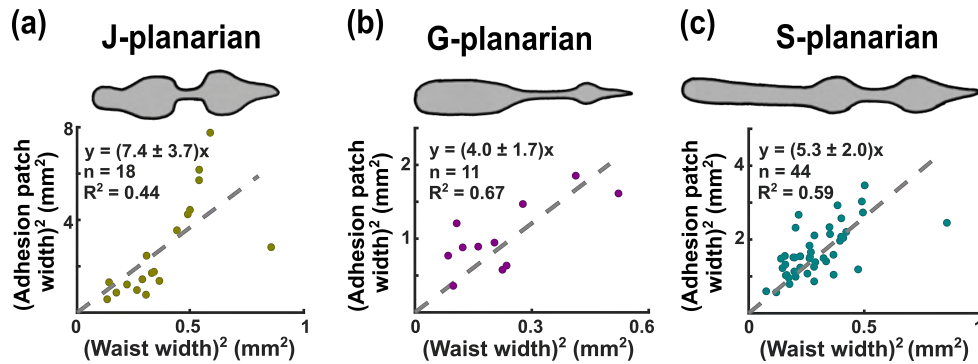
Figure 2.3: Phase 2 – Stress localization.(a-c) The square of the tail adhesion patch width plotted against the square of the width of the waist for a) J-planarians, b) G-planarians and c) S-planarians. Dashed lines represent linear fits. The slopes (shown as mean $\pm$ std) are used as estimates of the stress amplification factor.

For J- and G-planarians, waist formation is driven by active contraction of muscles. The initial constriction that appears during Phase 1 takes on the distinctive hourglass shape in Phase 2 when the adhesion patches form. Substrate adhesion is not necessary to create or maintain the waist in J- and G-planarians. This idea is supported by the observation that in both species, the shape of the waist is maintained even as the planarian continues to glide on the substrate and even after one of the adhesion patches slips and the tension is decreased (Figure 2.16(a, b)). However, substrate adhesion is indispensable for S-planarian waist formation. If one of the adhesion patches slips, the waist disappears, the S-planarian fails to rupture and must start elongating all over again (Figure 2.9; Figure 2.16(c)). Additionally, S-planarians frequently form several adhesion patches, resulting in formation of multiple evenly spaced temporary waists (Figure 2.16(d)). Eventually, one of these waists remains and the others disappear. This behavior suggests that in S-planarians: 1) waist formation is a passive result of elongation and, 2) there

appear to be multiple possible division planes which are evenly spaced, consistent with the presence of compression planes [15].

All three species use active, longitudinal motion to stretch the waist and build the necessary stress to initiate rupture. However, the three species use distinct mechanisms: J-planarians use asymmetric longitudinal head pulsations [32], G-planarians stretch their waist by attaching the tail to the substrate while the head moves away, and S-planarians continue to elongate, which stretches and thins the tissue in the waist (Figure 2.1(biii)). Importantly, substrate adhesion is critical for all these processes to build the tensile stress in the waist necessary for rupture. Substrate adhesion and behaviorally mediated tensile stress generation are also important for transverse fission in some species of acoels [43], suggesting that these are key, conserved aspects of self-bisection.

2.4.4   Phase 3: Rupture

Once the stress in the waist exceeds the ultimate tensile strength of the tissue, the tissue ruptures (Figure 2.4(a)). A small defect forms somewhere within the waist and then propagates across the waist until rupture and division are complete. The rupture process is significantly slower in S-planarians (2.9 (1.4,8.0) s, median (25th, 75th percentiles), n = 44, p $< 1 \times 10^{-4}$, Wilcoxon rank sum test) than in J- and G-planarians (0.5 (0.2,1.0) s, n = 14; 0.4 (0.2,0.7) s, n=12, respectively) (Figure 2.4(a)). To characterize the force balance within the waist, we compared the location of the initial rupture site in each species. Along the medio-lateral axis, all three planarian species showed rupture initiation at both the center and at the lateral edge of the waist (Figure 2.4(b)). This suggests that fracture nucleation is not tied to a fixed anatomical feature. For all species, the rupture plane lies close to the center of the waist along the A-P axis irrespective of the length of the waist (Figure 2.17). This suggests that the tensile forces on either end of the waist must be equal and opposite, assuming the tissue in the waist itself is homogeneous.

After rupture, the stretched tissue on either side of the rupture plane passively recoils to release the stored elastic energy. For all three species, the separation between the recoiling tissues follows an exponential saturation in time (Figure 2.4(c)). This recoil could be active or passive movement. While we cannot rule out contribution from active motion because we cannot visualize muscle activity during self-bisection, the exponential saturation suggests that the recoil is passive viscoelastic relaxation. Thus, treating the tissue as a Kelvin-Voigt material, we obtain relaxation times from the exponential fits, which are similar for J- and G-planarians ($p > 0.05$, Wilcoxon rank sum test) but significantly larger for S-planarians ($p < 0.001$, Wilcoxon rank sum test) (Figure 2.4(c)). The longer timescales observed in S-planarians, both for rupture and for recoil, suggest that the drag forces for S-planarians are larger than the other two species. Notably, the waist region is not in contact with the substrate during rupture and recoil (Figure 2.14(a)) and only interacts with the water surrounding it, which can be neglected. Therefore, since relaxation time is the ratio of the viscosity and Young's modulus, the longer timescales suggest increased viscosity of the S-planarian waist tissue or a decreased Young's modulus of the S-planarian tissue compared to the other species, either due to actual differences in material properties or, more likely, due to changes in properties induced during the division process. Imaging at a higher spatial and temporal resolution is needed to uncover the microscopic details of the fracture process – both to study fracture initiation and fracture propagation.

2.4.5   Biomechanical constraints govern offspring size and number

Offspring area scales with parent area in J- and G-planarians but not S-planarians

In J- and G- planarians, which primarily reproduce through fission, the area of the tail offspring scales linearly with parent area (Figure 2.5(a-b)). The slopes in Figure 2.5 correspond to the fraction of parent area that forms the tail offspring. In contrast, in S-planarians, which primarily reproduce through fragmentation creating multiple offspring, tail offspring area is
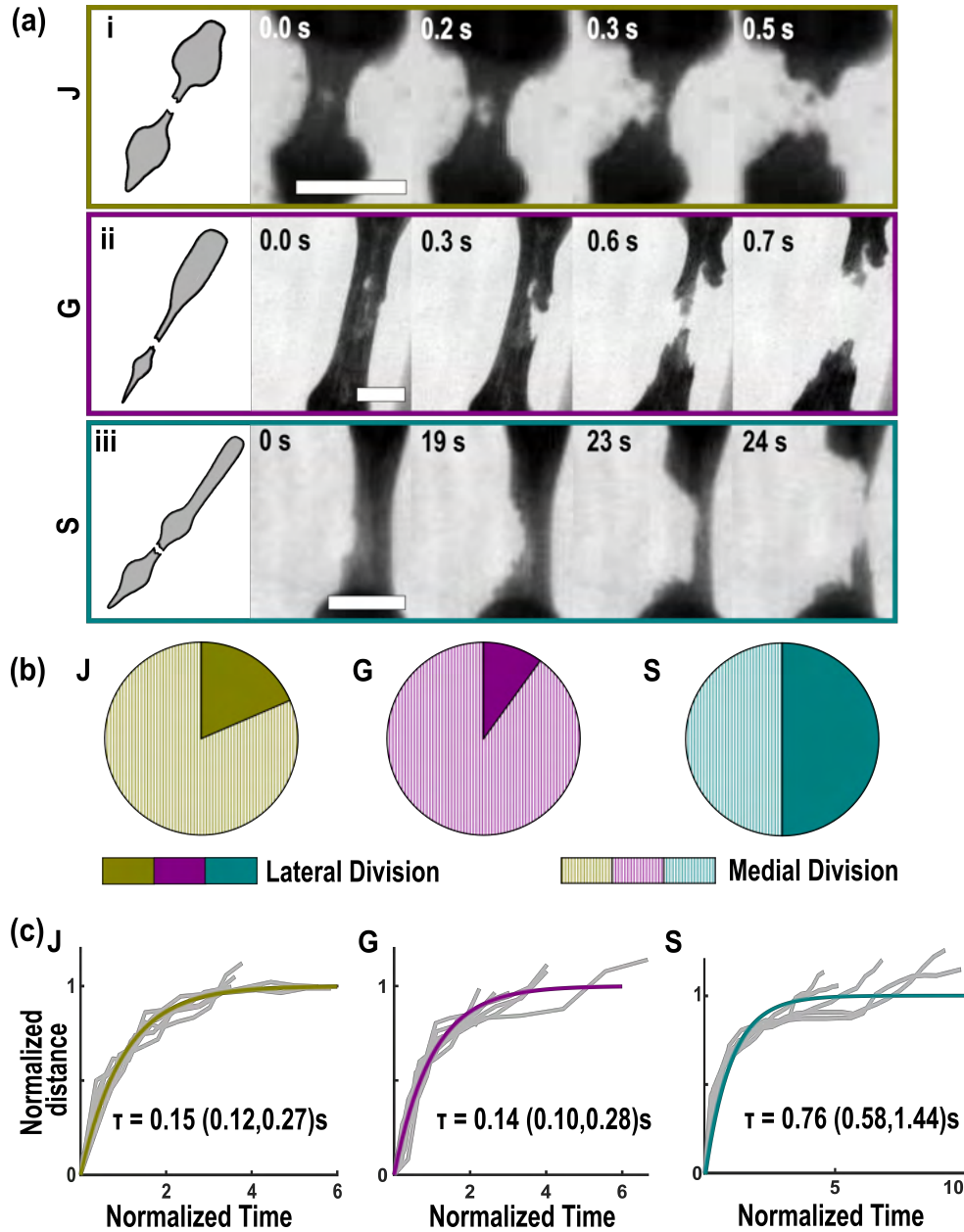
Figure 2.4: Rupture dynamics. (a) Example image sequence of rupture for a (i) J-planarian, (ii) G- planarian and (iii) S-planarian. Scale bar: 1 mm. (b) Fraction of medial and lateral rupture initiations for J-planarians (n = 25), G-planarians (n = 10) and S-planarians (n = 36). (c) Normalized distance between recoiling tissue pieces post-rupture as a function of normalized time for J-planarians (n = 12), G-planarians (n = 12) and S-planarians (n = 12). The grey lines indicate normalized recoil curves for each planarian. The colored solid lines indicate the curve $y = 1 - e^{-t}$. τ is the viscoelastic relaxation timescale reported as median (25th percentile, 75th percentile).

largely independent of the parent area and instead roughly constant (Figure 2.5(c)). Similar results were also found for trunk offspring of S-planarians and when using length as a measure of size instead of area (Figure 2.18), consistent with previous reports [15, 27, 29].

Notably, these relationships suggest that given the area of the parent, one can predict the size of the tail offspring for all three planarian species.
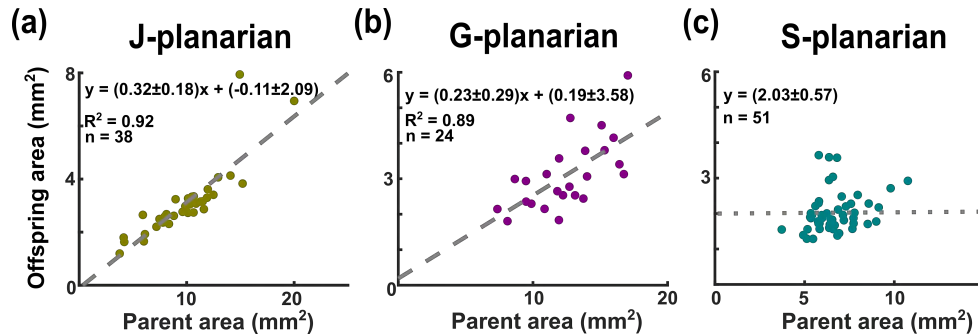
Figure 2.5: Planarian tail offspring area as a function of parent area. Tail offspring area plotted against parent area for (a) J-planarians, (b) G-planarians and (c) S-planarians. Linear fits are shown as dashed grey lines in (a) and (b). Slope and intercept for the fits are provided as mean ± standard deviation. Dotted line in (c) indicates average offspring area for S-planarians (mean ± standard deviation).

Planarians modulate substrate adhesion to maintain offspring size

Regenerating J-, G- and S-planarians show differences in relative substrate adhesion or "stickiness", with G-planarians being the stickiest and J-planarians the least sticky [41]. This trend is also true for intact planarians (Figure 2.6(a)). This trend in relative stickiness (J < S < G) is anti-correlated with relative tail offspring size (G < S < J) [13], i.e., the smallest tail offspring is created by the planarian species with the greatest stickiness (G-planarians). This observation suggests that with greater stickiness, a smaller adhesion patch area (and therefore a smaller tail offspring) is required for division. We tested how changing the effective tensile force, achieved by culturing planarians on an orbital shaker rotating at fixed angular frequencies, affected tail offspring area, relative to the static condition.

Increasing angular frequencies would introduce larger centrifugal forces on the planari-

ans. Considering the forces acting on the region posterior to the waist, which is at rest relative to the substrate at the time of rupture, the centrifugal force, the friction due to substrate adhesion and the tension from the waist need to balance out. To prevent slipping, the planarians would have to increase their total substrate adhesion to balance the centrifugal force now acting in addition to the tensile stress on the adhesion patches. We hypothesized that this would require the planarians to make larger adhesion patches and therefore larger tail offspring. However, none of the angular frequencies tested had a biologically meaningful effect on tail offspring area (Figure 2.6(b)). J- and S-planarians placed on frequencies higher than those shown in Figure 2.6 (120 and 140 rpm, respectively) did not divide during the observation time (3 weeks). Additionally, we found that more planarians had increased relative stickiness after being incubated on the shaker at 100 rpm for 3 days than when incubated without shaking (Figure 2.6(c), section 2.3.5), though this effect was not statistically significant for S-planarians. These results suggest that planarians can actively modulate their stickiness in response to external forces, thus preserving offspring size.

Constraints on waist formation mediate offspring number

Given the differences in the mechanisms of self-bisection between the three planarian species, we sought to determine whether these differences could explain the species' different reproductive strategies (see Introduction, Figure 2.8 and [13]).

J-planarians We observed three biomechanical constraints for J-planarian division. First, the position of the pharynx, a muscular feeding tube in the middle of the planarian body, is a restricted zone in which waist formation and division are not observed [32]. About 90% of J-planarian fissions occur post-pharyngeally (Figure 2.2(a) and [32]). If the post-pharyngeal tissue is insufficient to create appropriately sized adhesion patches, J-planarians divide pre-pharyngeally (Figures S2.12, S2.19). These pre-pharyngeal events account for the remaining
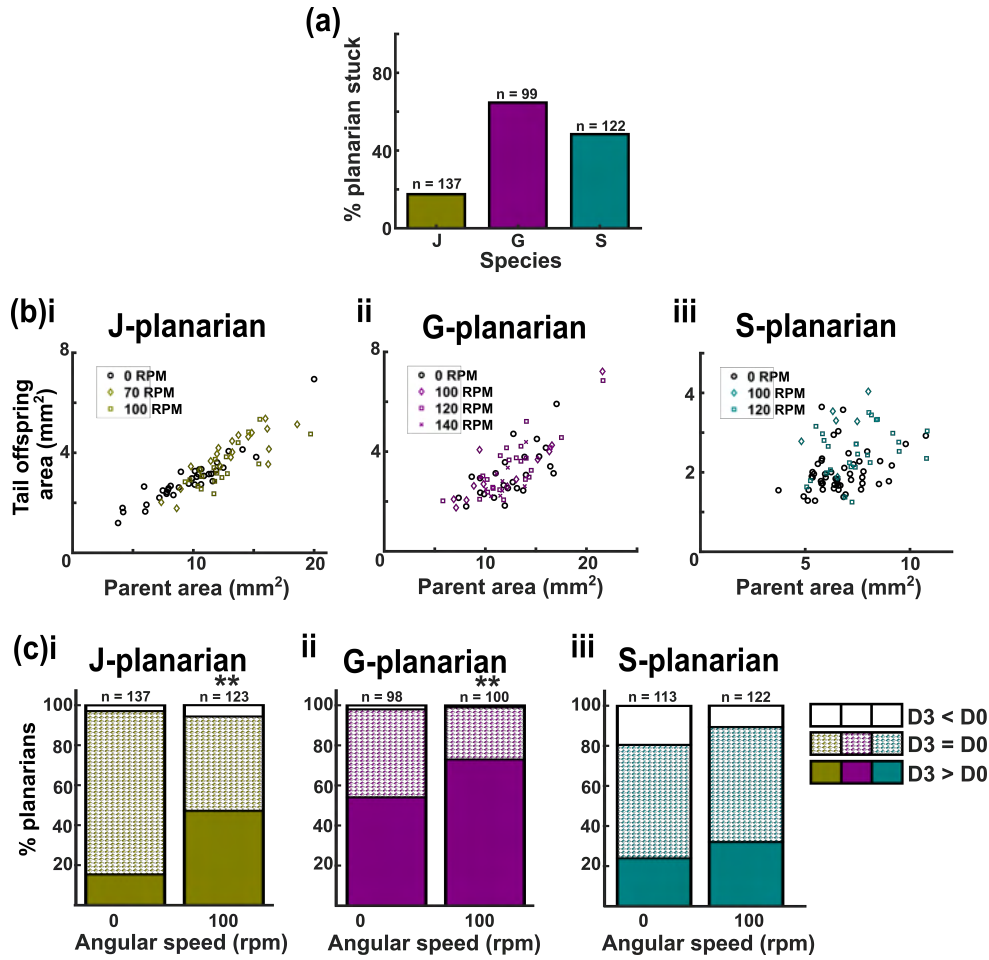
Figure 2.6: Response to centrifugal forces. (a) Percentage of planarians that remain stuck to the substrate at the end of the stickiness assay. Species with stronger substrate adhesion ("stickiness") have a higher percentage of stuck planarians. (b) Tail offspring area plotted against parent area for planarians that divided while being cultured on an orbital shaker at the specified angular speeds (rpms). No differences in the relationship between tail offspring area and parent area were observed for different angular speeds for any of the three species. (c) Comparison of change in relative stickiness between day 0 (D0) and after 3 days of culturing (D3) at 0 and 100 rpm of (i) J-planarians, (ii) G-planarians and (iii) S-planarians. This data is based on tracking individual worms. Solid bars indicate worms that had increased stickiness on D3, dotted bars indicate worms with the same level of stickiness on D3, and white bars indicate worms with decreased stickiness on D3 (see Section 2.3.5). (*) denotes $p < 0.05$ and (**) denotes $p < 0.01$ in comparison to the corresponding control (Fisher's exact test).

10% of J-planarian fissions in [32]. Second, we observed that the area of the tail offspring from a J-planarian fragmentation can be used to predict the area of the corresponding trunk offspring due to a linear scaling, constraining where a possible second division plane can form.

By comparing the observed and predicted trunk offspring area for a subset of the fragmentation events (Figure 2.20), we verified that the linear scaling is a good predictor of the trunk offspring area given the tail offspring area. The pharynx was always found in the trunk offspring of imaged offspring from J-planarian fragmentations (n = 21), demonstrating that a second division must be pre-pharyngeal (Figure 2.19). Third, using the scaling of trunk area with tail area of fragmentations, we calculated the areas of a theoretical trunk (Figure 2.7(a)) and head offspring (Figure 2.7(b)) resulting from a theoretical second division in J-planarians that only fissioned, albeit being of comparable size to J-planarians that fragmented. We found that the areas of these theoretical head offspring were generally smaller than those of J-planarians that fragmented (Figure 2.7(a-b)). This suggests that most of the planarians that only divided once did not have had sufficient pre-pharyngeal tissue for a second division. A small fraction of J-planarians appear to theoretically have had sufficient tissue to divide again and fragment, but did not do so, suggesting that other, non-mechanical factors influence the decision between fission versus fragmentation.

G-planarians G-planarian fission is initiated by tail constriction, creating a popsicle-like shape. The area of the tail of the popsicle has a fixed proportionality to the parent area (Figure 2.7(c)). We and others [31, 44, 45] have only observed post-pharyngeal divisions in this species, suggesting that, like J-planarians, G-planarians will not form a waist containing the pharynx. Considering G-planarian head offspring resulting from a fission, we find that there is insufficient post-pharyngeal tissue to form the constriction necessary for a second division (Figures 2.7(d) and S2.12). Two of 22 (9%) G-planarians imaged post-division had sufficient post-pharyngeal tissue to potentially divide again (data points within the error bars in Figure 2.7(d)), suggesting that this is the possible fragmentation rate in this species. This is consistent with previous large scale population data showing that fragmentation accounts for 6% of G-planarian reproductive events [13].
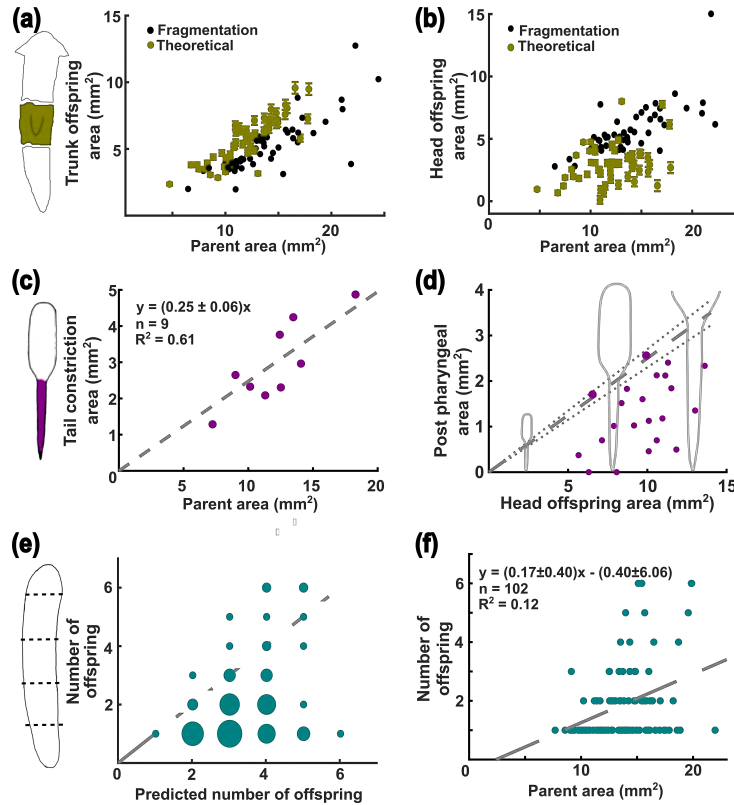
Figure 2.7: Offspring number is directed by constraints on waist formation. (a) Area of actual trunk offspring observed in fragmentation events and theoretical trunk offspring expected after fission events as a function of parent area for J-planarians. Error bars are twice the width of the standard error in theoretical predictions. (b) Area of the actual head offspring observed in fragmentation events and theoretical head offspring expected in fission events as a function of the parent area. Most theoretical head offspring are smaller than those observed from fragmentation of J-planarians of comparable parent size. (c) Area of tail constriction as a function of gliding area of the parent G-planarian. Dashed line represents a linear fit, with the slope provided as mean ± standard deviation. (d) Area of the post-pharyngeal region of G-planarian head offspring immediately after division as a function of the head offspring area. The dashed line is $y = 0.25x$, corresponding to the linear fit line in (c). Dotted lines indicate the bounds of the standard error. Only planarians whose post-pharyngeal area lies above the lower dotted line would be able form a tail constriction of the required size to be able to fragment. Because the planarians were not observed post first division, we do not know whether the two worms that are big enough ultimately fragmented. (e) Experimentally observed number of offspring plotted against predicted number of offspring for n = 102 S-planarians. Offspring number is predicted by dividing the parent area by the average tail offspring area. Dashed line represents the 1:1 line for a visual guide. Size of circles corresponds to the frequency of a particular (x, y) pair. (f) Number of offspring as a function of parent area for S-planarians. Dashed line represents a linear fit, with the slope and intercept provided as mean ± standard deviation.

S-planarians Unlike J- and G-planarians, S-planarians primarily fragment and produce multiple offspring per reproduction event. Since S-planarian tail/trunk offspring are of roughly constant size (Figures 2.5(c) and S2.18), we can predict the number of offspring an S-planarian could theoretically produce by dividing the parent area by the average tail offspring area (Figure 2.7(e)). Interestingly, this largely overpredicts the number of offspring produced (Figures 2.7(e), S2.18(c)). S-planarian parent area and length only have a weak positive correlation with offspring number (Figures 2.7(f), S2.18(d)), consistent with previous reports [15, 27, 29] and the number of offspring produced is highly variable for an S-planarian of a given size (Figures 2.7(e), S2.18(c)). Thus, size is not a predictor of the number of offspring that will be produced, as even very large S-planarians sometimes only fission (Figures 2.7(f), S2.18(d)) [27, 29]. These data suggest that - like what we observed for J-planarians - other, size-independent factors affect how many offspring are produced in a given reproductive event.

2.5   Discussion

Through continuous large-scale, long-term imaging at unprecedented temporal and spatial resolution, we investigated the mechanics of self-bisection across three planarian species (J-, G- and S-planarians). Two characteristics were found to be critical for division in all three species: (1) formation of a narrow waist to amplify stress and (2) the need for sufficient substrate adhesion to maintain the tensile stress in the waist to allow for rupture.

To our surprise, we found that the planarian species accomplished these tasks through distinct mechanisms. Most notably, how the waist forms differs across the species. J- and G-planarians actively constrict their circular muscles at specific relative locations along the length of the worm (Figure 2.2(a)). This constraint on where the waist forms directly dictates the distribution of biomass among the offspring, as evidenced by the scaling relationship of tail offspring to parent area (Figure 2.5). In contrast, waist formation in S-planarians occurs

primarily because of elongation and depends on the adhesion patches. S-planarians that lose adhesion and slip must restart the division process, whereas J- and G-planarians create and maintain their waist independently of the adhesion patches (Figure 2.16).

While J- and G-planarians do not require the adhesion patches for waist formation, substrate adhesion is critical in all three species for successful rupture. All three species regulate their substrate adhesion in response to external forces to maintain offspring size (Figure 2.6). These species have wide ecological ranges where they would encounter substrates of different physical properties (roughness, stiffness). However, changing substrates (soft and sticky PDMS versus hard and roughened plastic) had no obvious effects on fission dynamics, in agreement with the findings reported in [32], where J-planarian fission was studied on hard plastic and extremely soft PDMS, without any difference in dynamics. Since the size of the offspring influences their survival and reproductive success, it makes sense that the planarians can modulate other factors to maintain offspring size. Planarians interact with the substrate through a layer of secreted mucus. Thus, substrate adhesion can be regulated by changes to the quantity and/or composition of the mucus—something planarians also do in response to chemical exposure [32, 41, 46]. Thus, we tried to modulate mucus by exposing the planarians to the detergent Triton-X 100, which was previously shown to increase mucus production and stickiness in J-planarians [32]. However, because we can neither predict nor induce planarian self-bisection, this required long-term Triton-X 100 exposure which caused adverse health effects such that the planarians no longer divided.

Understanding how each of these planarian species self-bisects and the subsequent relationships between offspring and parent size allows us to predict the size of the posterior offspring for each species. For J- and G-planarians, if given the size of the parent, the tail offspring size can be predicted based on the demonstrated scaling relationship. The scaling relationship for J-planarians is only based on post-pharyngeal divisions, which constitute most division events. Pre-pharyngeal divisions are a small minority of division events (approximately

10%) and only occur in planarians with short RWTs which had insufficient time to reposition their pharynx [32]. As previously shown [32], if given the relative pharynx location of the parent planarian, one can predict whether division will occur pre- or post-pharynx. This predictability allows for the development of theoretical growth models to explain the observed reproductive behavior [30].

S-planarian offspring size is roughly constant and thus also predictable. The observation that S-planarians generate multiple successive offspring of roughly constant size agrees with the recently proposed compression plane model [15]. The model proposes that S-planarians have mechanically weak compression planes at regularly spaced intervals along the A–P axis that are used for rupture. While this idea cannot be tested directly because visualizing the compression planes kills the animal [15], we have observed that S-planarians often initially form multiple, evenly spaced temporary waists (Figure 2.16(d)) until one is eventually 'chosen' and used for rupture. These temporary waists could be indicative of the mechanically weak compression planes. It remains unclear what determines at which plane division will occur, as it is not always the most posterior waist that is 'chosen'. This stochastic element may contribute to the large variability observed in S-planarian offspring size.

In fact, across multiple parameters (RWT, number and size of offspring, timescales of fracture and recoil), S-planarians have noticeably greater variance than the other two species. We speculate that these differences are a direct consequence of the different division biomechanics: J- and G-planarians form their waist through active muscle contractions at specific locations whereas S-planarians first stretch, forming the waist at a structural weak point, which can only be maintained with the presence of adhesion patches. Thus, S-planarian self-bisection appears to be less controlled, leading to greater sources of variability.

We have demonstrated here that mechanical constraints can explain the observed reproductive behavior and lack of fragmentations in J- and G-planarians. However, worm area and/or mechanical constraints alone are not predictive of offspring number for S-planarians.

Furthermore, the prediction for J-planarian behavior is not absolute; about 6% (n = 52) of imaged J-planarians would have been able to fragment based on the mechanical constraints but did not do so. This implies that other, non-mechanical mechanisms influence whether an individual planarian of sufficient size for fragmentation ultimately undergoes fission or fragmentation.

Biochemical signaling gradients may be the missing link to understand the stochasticity in the control of offspring number per reproductive event. A recent theoretical model has attempted to use biochemical gradients to explain where and when planarians divide based on a controlled, cross-inhibited Turing system [16]. The model qualitatively explains several experimental observations: presence of fission and fragmentation, increase in fission activity upon decapitation and the relative size of the offspring [16]. However, as a deterministic model, it cannot recapitulate the observed stochasticity in planarian division. Moreover, it is based on data and assumptions from multiple planarian species, which, as we have shown here, do not have the same reproductive behavior. These differences have clear effects on division location and thus need to be accounted for.

Several different signaling pathways may play roles in governing planarian asexual reproduction. Consistent with the Turing model, A–P axis polarity in S-planarians is maintained through self-organized Wnt gradients autonomously formed in the tail [47]. A head-based patterning system that mutually inhibits the Wnt patterning system in the tail is also needed [47]. Wnt and TGFβ signaling have been implicated in controlling the frequency of division in S-planarians while Hox signaling has been shown to affect the number of compression planes and the spacing between them [14, 15].

Most of this biochemical understanding has arisen from studies on S-planarians. While Wnt signaling has also been shown to be important for axial patterning in J- and G-planarians [48–50], it is unclear whether there are differences in gradient intensity or slope that may lead to the species-specific mechanisms that we have observed. In addition to morphogen gradients, positional control genes expressed in muscle cells have been shown to provide important

positional cues, allowing the muscles to act as a coordinate system for tissue regeneration [51]. Given the active role of muscle contraction in waist formation in J- and G-planarians, it is possible that muscle cells may set their own positional cues and then act upon them. In addition, the secreted trophic factor TCEN49 has been found to be necessary but not sufficient to induce fission in G-planarians, suggesting a potential role of the nervous system in fission induction [52]. This neuronal control is likely regional as the brain is not required for division.

Together, these observations suggest that morphogen gradients, neuronal signals, and the biomechanical constraints shown here, cooperate to regulate when and where a planarian will divide. While the details of this cooperation will likely differ given the differences in reproductive strategies, key components of the process—such as the mechanical ones identified here (waist formation, substrate adhesion and tensile stress generation)—are expected to be universal. Two key experimental challenges must be overcome to further dissect this coordinated interplay between mechanical and biochemical signaling *in vivo*: (1) the ability to trigger fission on demand to record division with higher spatial and temporal resolution, and (2) *in vivo* labeling of proteins implicated in fission regulation.

2.6   Acknowledgments

2.7 Supplementary Information

The supplemental material below can also be found online at https://doi.org/10.1088/1478-3975/ac2f29.

2.7.1 Supplementary Methods

Resting and gliding lengths and areas

A rectangular transparent plastic lid was split into 6 shallow chambers on a 3x2 square grid using petroleum gel as separating agent. A planarian was placed in each chamber. The setup was lit from below using a blue electroluminescence panel (Adafruit). The lid was first imaged from the top for at least 10 s at 5 frames per second (fps) while the planarians were at rest using a Basler CCD camera. The dish was then imaged for 2 min at 5 fps while the planarians were moving around in the dish. The lengths were measured using the skeletonize and analyze skeleton functions in the Fiji distribution of ImageJ [40]. The areas were measured using the analyze particles function. For the rest lengths and areas, the measurements obtained from Fiji were averaged over the frames where the planarian was not moving. For the gliding lengths and areas, only frames where the planarian was moving in the center of the dish in a straight line were used.

Estimation of stress amplification factor and linear strain

Because the experimental challenges associated with studying fission dynamics prevented us from gathering volumetric data (see Methods section 2.3.2), we estimated the magnitude of the stress amplification factor by making the following assumptions about the cross section of both adhesion patches and the waist:

1. The cross-sectional area of each region scales quadratically with its respective width.

2. We neglect the numerical pre-factor associated with the shape of the cross section since it is of the order unity and would be the same for all 3 species.

We therefore estimated the stress amplification factor from the slope of the linear fit of the squares of the width of the adhesion patch vs the squares of the width of the waist. We can make this estimate using either the anterior (Figure 2.15(a-c)) or posterior adhesion patch (Figure 2.3). Because the posterior adhesion patch remains stationary in all three species while the anterior adhesion patch does not, we used the posterior adhesion patch to compare how stress is amplified in the waist across species.

We estimated the maximum linear strain for S-planarians as

$$\frac{\text{length just before rupture} - \text{rest length}}{\text{rest length}}$$

This assumes that the tissue elongates homogeneously along the length of the planarian. This is the simplest approximation that can be made in the absence of fixed features on the planarian body. To estimate the maximum linear strain for J-planarians, we used values published in Table S1 in Malinowski *et al.* [32]. We estimated the maximum linear strain for G-planarians according to

$$\frac{\text{maximum waist length} - \text{minimum waist length}}{\text{minimum waist length}}$$

Estimating ultimate tensile strength

To estimate the ultimate tensile strength across species, we assumed the Young's modulus of the tissue to be same across the species using a value for S-planarians [42], which is a reasonable assumption given their similar tissue properties. We then calculated the dimensionless ultimate tensile strength as the product of linear strain and the stress amplification factor.

The root mean squared error for the estimate of ultimate tensile strength was calculated

42

using the formula:

$$\frac{\delta f}{f} = \sqrt{\left(\frac{\delta a}{a}\right)^2 + \left(\frac{\delta b}{b}\right)^2}$$

Where f is the mean ultimate tensile strength, δf is the root mean squared error, a is the mean linear strain, b is the mean stress amplification factor and δa and δb are the corresponding standard deviations.

To compare the ultimate tensile strength across the species, we computed the t-statistic as

$$t = \frac{|f_1 - f_2|}{\sqrt{\delta f_1^2 + \delta f_2^2}}$$

Where f is the mean ultimate tensile strength, δf is the root mean squared error and the subscripts 1 and 2 denote species 1 and 2. Statistical significance was then tested using a 2-tailed t-test.

2.7.2 Supplementary Text 1. S-planarian elongation during Phase 1 is sigmoidal

S-planarian elongation during Phase 1 follows a characteristic sigmoidal time course. The change in length can be fit to a hyperbolic tangent curve:

$$\frac{\Delta l}{l_0} = \frac{a}{2}\left(1 + tanh\left(\frac{t - t_0}{\tau}\right)\right)$$

Here, Δl is the change in length of the S-planarian over time (t) and l_0 is the rest length of the worm. The parameters a, t_0 and τ represent the maximum relative length change, time taken to reach half maximum length, and timescale of elongation, respectively. Normalizing time and length change by these parameters, the length change curves for all S-planarians analyzed (n = 16) collapse onto a single curve (Figure 2.2(c)). Further, we obtain a timescale of elongation, $\tau = 180 \pm 25$ s (mean $\pm$ std, n = 16), indicating that S-planarians elongate over a

period of about 3 minutes.

Table 2.1: Comparison of population-level reproductive statistics in the three planarian species. Data shown as median (25th percentile, 75th percentile). Fission and fragmentation data were combined; thus area fractions do not add up to 1.

	J-planarians		S-planarians		G-planarians	
	Head	Tail	Head	Tail	Head	Tail
Area at Birth (fraction of parent area)	0.73 (0.69, 0.77)	0.26 (0.22, 0.30)	0.71 (0.65, 0.78)	0.21 (0.17, 0.27)	0.80 (0.77, 0.83)	0.19 (0.17, 0.22)
RWT (days)	21 (14, 25)	42 (31, 55)	18 (8, 45)	81 (46, 108)	12 (11, 14)	29 (19, 45)
Death Rates (%)	$\sim$0.1	$\sim$1	$\sim$2	$\sim$10	$\sim$2	$\sim$12

2.7.3   Supplementary Figures
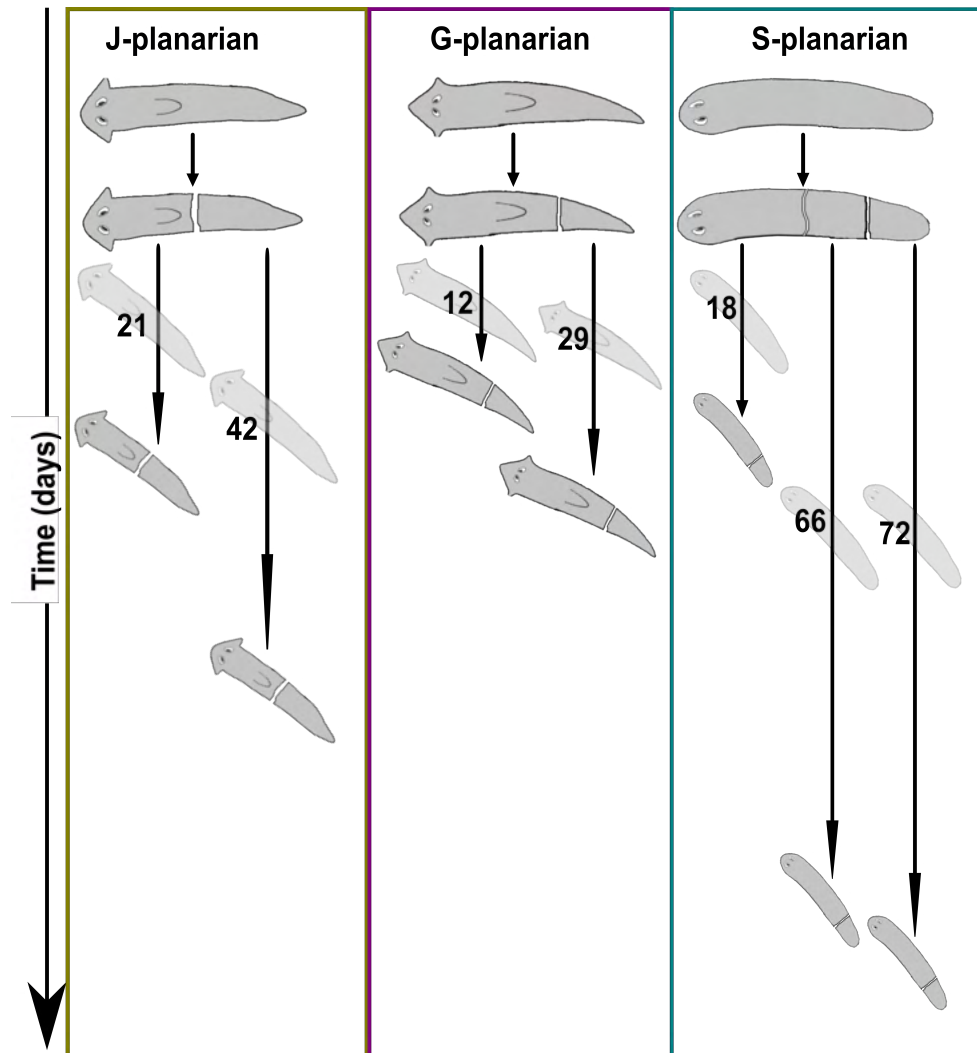
Figure 2.8: Different reproductive strategies. Schematic of the population reproductive strategies of J-, G- and S-planarians. J- and G-planarians primarily fission, producing two offspring, whereas S-planarians primarily fragment, producing a head, a tail, and one or more trunk (middle piece) offspring [13]. J-planarians allocate resources most evenly between head and tail offspring of the 3 species. In contrast, G-planarians produce large heads and small tails, and S-planarians produce multiple offspring per cycle at the cost of the head offspring. RWTs for S-planarian trunk and tail offspring were obtained from [29]. The rest correspond to median values in Table 2.1. Within each species, the heads have shorter RWTs than tail and trunk offspring
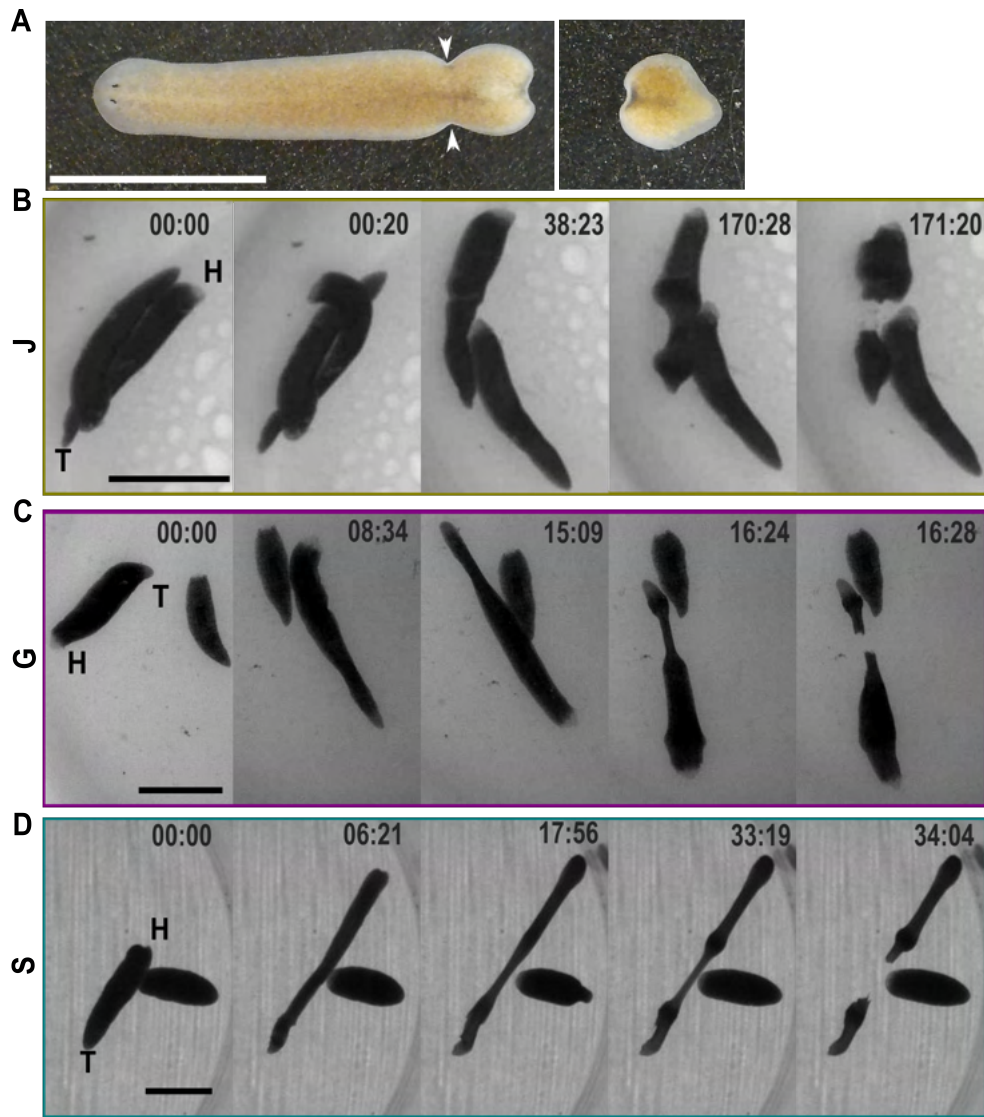
Figure 2.9: Self-bisection stops due to physical disturbances but proximity to conspecifics does not inhibit self-bisection. (a) Left: S-planarian head offspring undergoing fragmentation halts self-bisection due to a disturbance. A plastic deformation of the body remains at the site (indicated by white arrowheads) where division would have occurred. Right: Tail offspring from the first division which completed before the disturbance occurred. Scale bar: 4 mm. (b-d) Representative image sequences of (b) J-planarians, (c) G- planarians and (d) S-planarians. Scale bar: 4 mm. H: head, T: tail. Time stamps are minutes: seconds. Planarians divide despite being in contact with other planarians, refuting previous claims of contact inhibition [35–38].
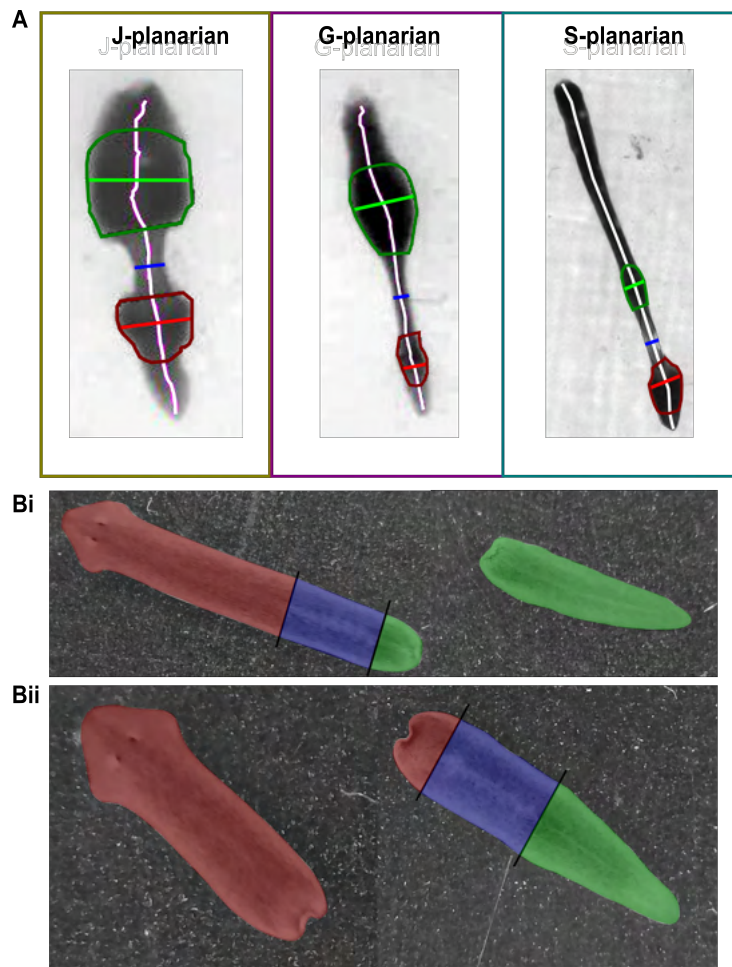
Figure 2.10: Illustration of various measurements of planarian morphological features. Measurements taken during division. The white line denotes the centerline of the planarian. The length of the line is taken as the length of the worm. All widths are measured perpendicular to the centerline. The fluorescent green, blue and red lines denote the widths of the head adhesion patch, the waist and the tail adhesion patch, respectively. The green and red boundaries denote the head and tail adhesion patches, respectively. Adhesion patches were identified as darker regions immediately anterior and posterior to the waist that did not start moving immediately before or after waist rupture was complete (Methods). (b) Measurements taken in offspring post-division. The black lines demarcate the pharynx region (highlighted in blue) within the offspring. Pre-pharyngeal and post-pharyngeal regions are highlighted in red and green, respectively, for (i) post-pharyngeal divisions and (ii) pre-pharyngeal divisions. Total post pharyngeal area was the sum of the green regions in (i), and total pre-pharyngeal area was the sum of the red regions in (ii).
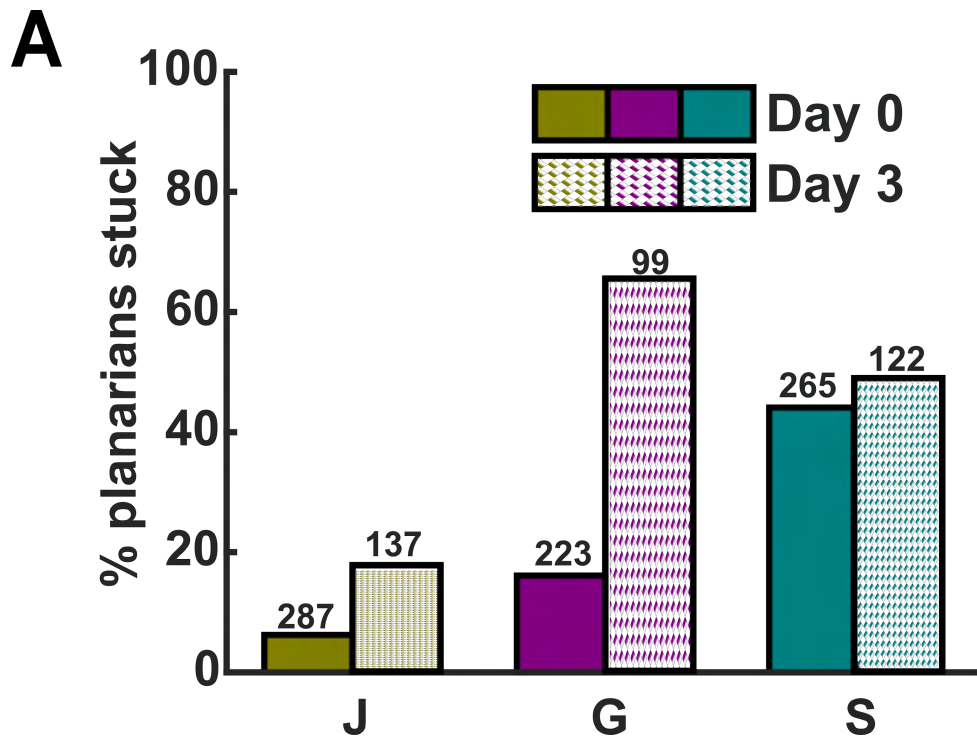
Figure 2.11: Relative stickiness of the three species. (a) Percentage of control planarians that remained stuck to the substrate at the end of the stickiness assay on Day 0 or Day 3 of being cultured in 48 well plates at 0 rpm. Numbers on the bar indicate sample size. G-planarians have unrepresentatively low stickiness on Day 0, potentially due to disruption of the mucus from being pipetted.
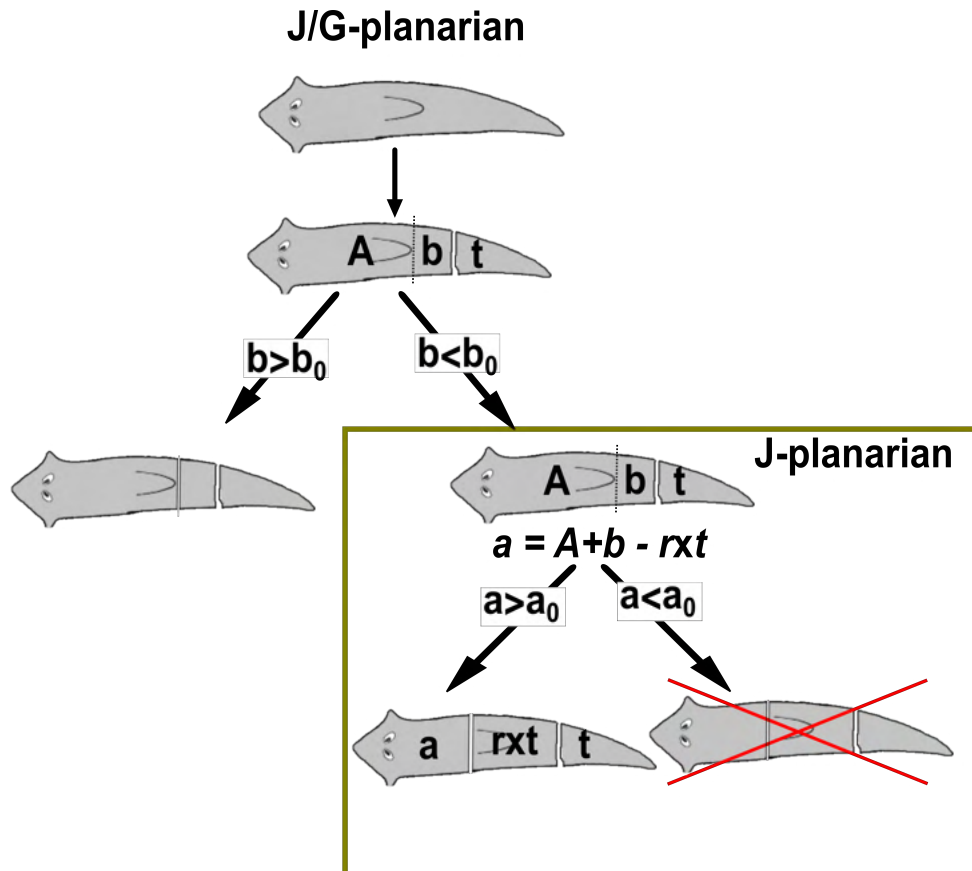
Figure 2.12: Schematic explanation of when J- and G-planarians fragment. J- and G-planarians each require a characteristic minimum tail area b_0. Following a post-pharyngeal division, if the remaining post-pharyngeal area 'b' of the resulting head offspring exceeds b_0 ($b > b_0$), the planarian can undergo a second post-pharyngeal division. Else, if the resulting head offspring does not have sufficient post-pharyngeal area remaining ($b < b_0$) and it is a G-planarian, it cannot divide again. For J-planarians, a second, pre-pharyngeal division is possible if the new head offspring area 'a' exceeds the minimum area a_0 ($a > a_0$). 'r' is the ratio of the areas of the trunk and tail offspring observed in fragmentation events. This ratio was used to calculate the areas of the theoretical trunk ('r' times the area of tail 't') and head offspring (area of fission offspring – area of theoretical trunk).
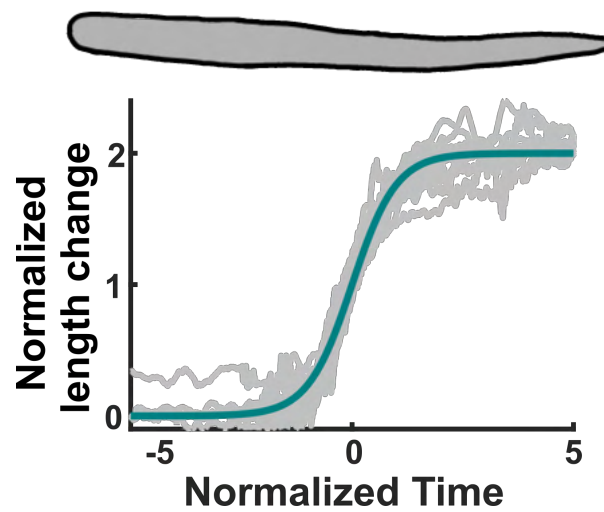
Figure 2.13: S-planarians elongation is sigmoidal. Length change normalized such that maximum length change = 2, as a function of time, normalized to the elongation timescale, for S-planarians. Data for individual planarians (n=16) are shown are as gray lines. Blue line indicates the curve $y = 1 + \tanh(x)$.
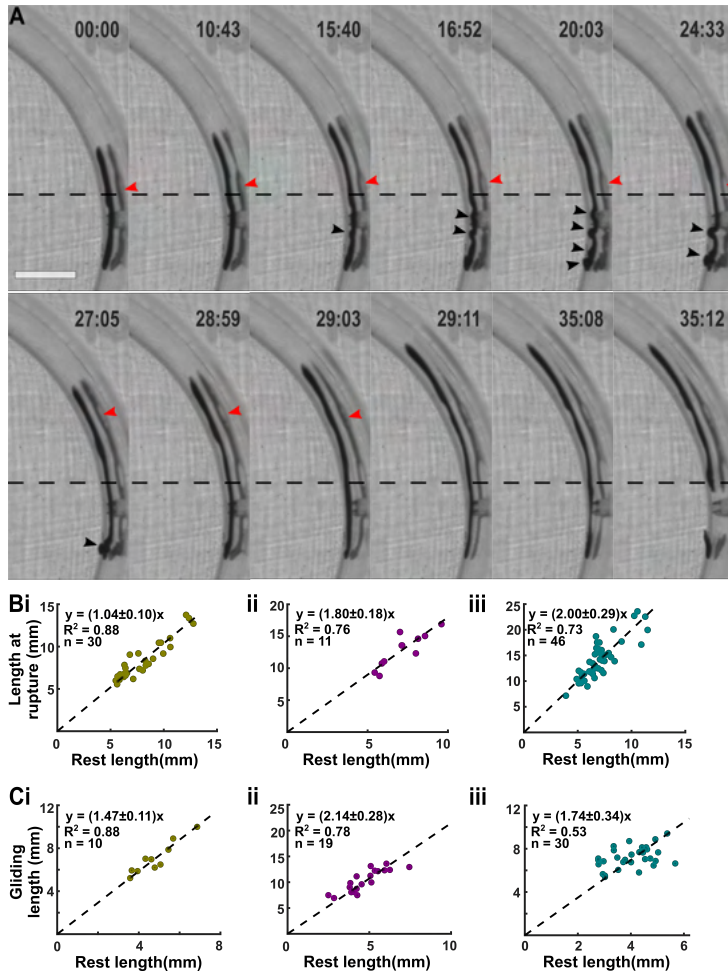
Figure 2.14: S-planarians, but not J- and G-planarians, elongate during division. (a) Example image sequence showing elongation and buckling in S-planarians. Black arrows indicate buckles. The buckling wavelength was found to be 0.83 ± 0.14 mm (n=4). Red arrows indicate a region where the planarian detaches from the substrate (focus on the worm reflection). Dashed line is a visual guide for the movement of the detached region. Scale bar: 4 mm. (b) Length at rupture as a function of rest length for (i) J-, (ii) G- and (iii) S-planarians. (c) Gliding length as a function of rest length for (i) J-, (ii) G- and (iii) S-planarians. Dashed lines represent linear fits with slopes presented as mean ± standard deviation. Note that the slopes for gliding length vs rest length are larger than the slopes for length at rupture vs rest length for G- and J-planarians, showing that these species do not extend as much during division as they do during gliding.

51
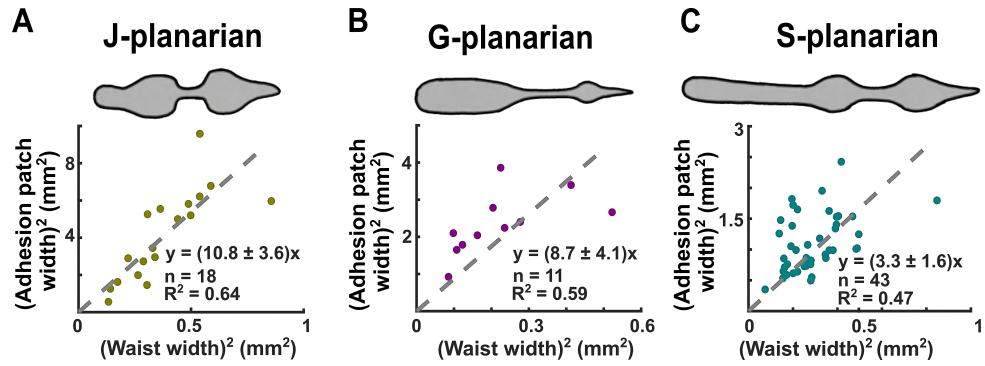
Figure 2.15: Stress amplification. (a-c) The square of the head adhesion patch width plotted against the square of the width of the waist for a) J-planarians, b) G-planarians and c) S-planarians.
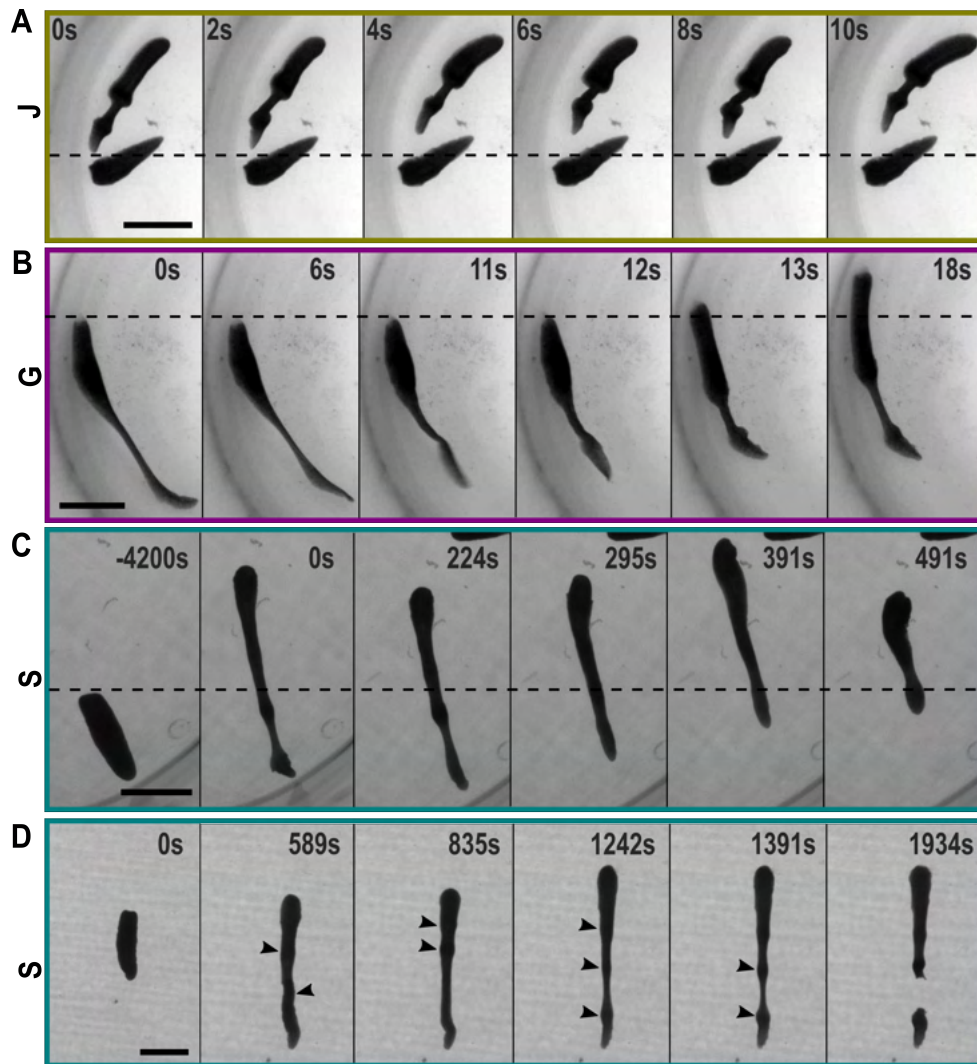
Figure 2.16: Loss of substrate adhesion has different consequences in the three planarians species. (a) Example image sequence showing J-planarian adhesion patch slipping. J-planarians that slip must execute more head pulsations to rupture [32]. (b) Example image sequence showing G-planarian adhesion patch slipping. Notice that the waist remains intact in J- and G-planarians even after slipping, showing that substrate adhesion is not necessary to maintain the waist in these species. (c) Example image of adhesion patch slippage in an S-planarian which led to a failed fission event. Dashed line in a-c added as a reference marker. (d) Example image sequence showing formation of temporary waists during elongation in S-planarians. Black arrows highlight adhesion patches. The distance between the temporary adhesion patches is 4.21 ± 1.15 mm (mean $\pm$ std, n = 56 pairs of patches from n = 31 planarians). Scale bar: 4 mm.
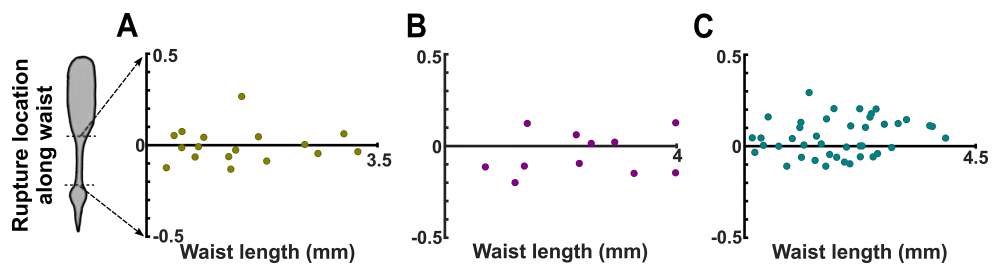
Figure 2.17: Rupture occurs in the center of the waist. Location of the rupture site along the Anterior-posterior (A-P) axis for (a) J-, (b) G- and (c) S-planarians is close to the center of the waist.
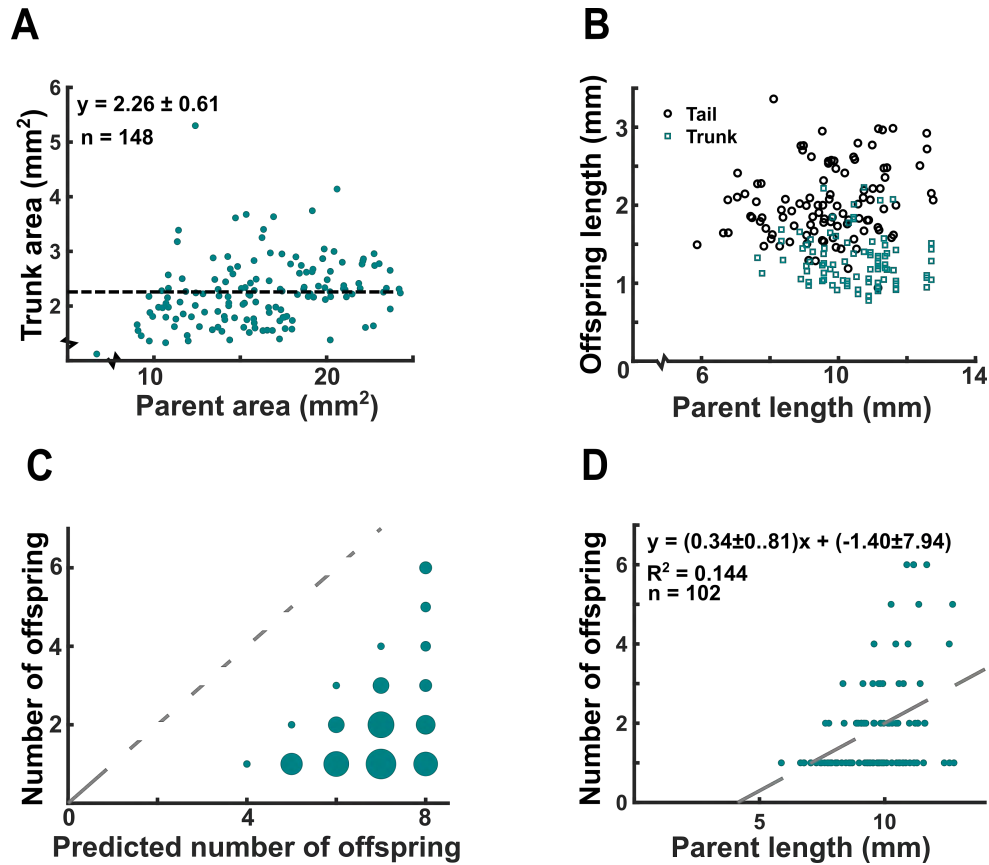
Figure 2.18: S-planarians trunk offspring area vs parent area. (a) Area of trunk offspring plotted against parent area. Trunk offspring area does not depend on parent area, similar to tail offspring (Figure 2.5(c)). The dotted black line indicates the average trunk area: 2.26 ± 0.54 mm^2 (mean ± standard deviation). (b) Lengths of tail and trunk offspring plotted against the length of the parent. Like areas, no dependence on parent length is observed. (c) Experimentally observed number of offspring plotted against predicted number of offspring for n = 102 S-planarians. Offspring number is predicted by taking the difference of the parent length and average tail length and then dividing that by the average length of the trunk. Dashed line represents the 1:1 line for a visual guide. Size of circles corresponds to the frequency of a particular (x, y) pair. (d) Number of offspring as a function of parent length for S-planarians. Dashed line represents a linear fit, with the slope and intercept provided as mean ± standard deviation.
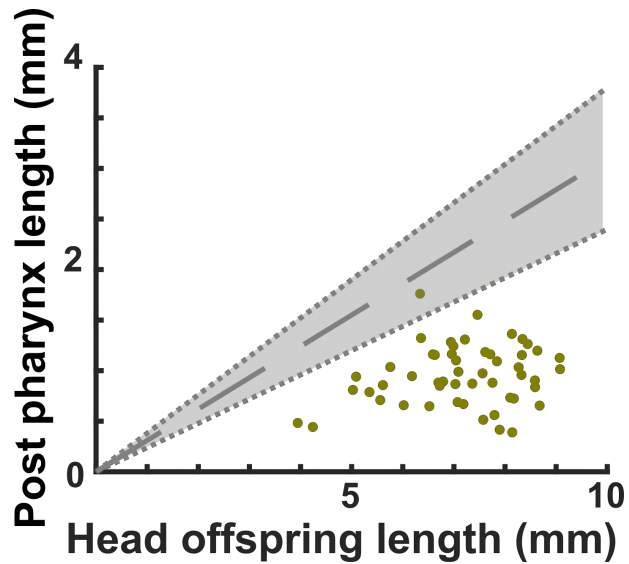
Figure 2.19: J-planarian head offspring cannot divide post-pharyngeally. Length of the post-pharyngeal tissue remaining after the first division plotted against the length of the entire head offspring of a J-planarian that underwent fission. Dashed line represents 31% of the head offspring length. Grey zone depicts $\pm$ 1 standard deviation (7%) of the head offspring length. Head offspring that lie below the grey zone theoretically cannot divide again post-pharyngeally.
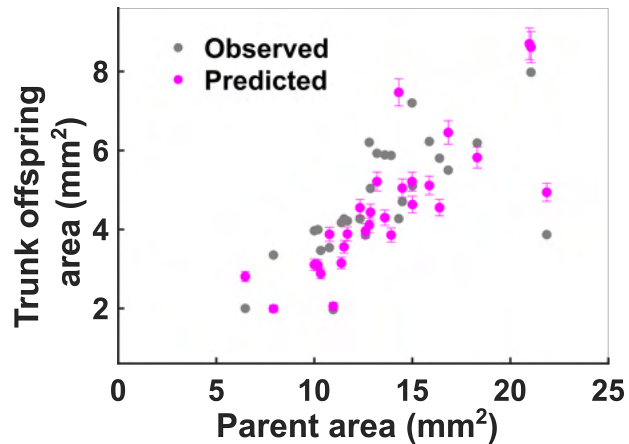
Figure 2.20: The mean trunk offspring area to tail offspring area ratio is a good predictor of trunk offspring size. A second dataset containing the areas of head, trunk and tail offspring of J-planarians was used to verify that the constant 'r' – the mean ratio of the trunk offspring area to tail offspring area obtained from measurements of some J-planarians – is a good predictor of trunk offspring area. The observed trunk areas in this second dataset as a function of parent area are plotted in grey. The predicted trunk areas, obtained by multiplying the constant 'r' with the observed tail offspring area, are plotted in magenta.

2.7.4 Supplemental Movies

Movie file link: https://github.com/tapangoel1994/ThesisMovies.git.

Movie S1: Intact J-planarian division. Representative time-lapse movie of an intact J-planarian dividing. Video playback: 15 fps. Scale bar: 1 mm.

Movie S2: Intact G-planarian division. Representative time-lapse movie of an intact G-planarian dividing. Video playback: 15 fps. Scalebar: 3 mm.

Movie S3: Intact S-planarian division. Representative time-lapse movie of an intact S-planarian dividing. Video playback: 15 fps. Scalebar: 2 mm.

Chapter 3

Mouth function determines the shape oscillation pattern in regenerating *Hydra* tissue spheres

3.1   Abstract

Hydra is a small freshwater polyp capable of regeneration from small tissue pieces and from aggregates of cells. During regeneration, a hollow bilayered sphere is formed that undergoes osmotically driven shape oscillations of inflation and rupture. These oscillations are necessary for successful regeneration. Eventually, the oscillating sphere breaks rotational symmetry along the future head-foot axis of the animal. Notably, the shape oscillations show an abrupt shift from large-amplitude, long-period oscillations to small-amplitude, short-period oscillations. It has been widely accepted that this shift in oscillation pattern is linked to symmetry breaking and axis formation, and current theoretical models of *Hydra* symmetry breaking use this assumption as a model constraint. However, a mechanistic explanation for the shift in oscillation pattern is lacking. Using *in vivo* manipulation and imaging, we quantified the shape

oscillation dynamics and dissected the timing and triggers of the pattern shift. Our experiments demonstrate that the shift in the shape oscillation pattern in regenerating *Hydra* tissue pieces is caused by the formation of a functional mouth and not by shape symmetry breaking as previously assumed. Thus, model assumptions must be revised in light of these new experimental data, which can be used to constrain and validate improved theoretical models of pattern formation in *Hydra*.

3.2 Significance

Hydra spheres originating from tissue pieces or aggregates of body column cells undergo dramatic osmotically driven shape oscillations during regeneration. Previous works proposed a causal link between a characteristic abrupt shift in the frequency of shape oscillations of regenerating spheres and *de novo* axis specification via the establishment of morphogen gradients. Here, we break this link by demonstrating that regeneration without an oscillation pattern shift is possible and that the shift is a direct consequence of mouth function and its use in osmoregulation. Because the link between oscillation dynamics and axis specification was a key assumption in current models of *Hydra* regeneration, our results indicate that we must reexamine the mechanisms driving pattern formation in *Hydra*.

3.3 Introduction

Hydra is a small ($\sim$ 1 cm long), transparent, radially symmetric freshwater cnidarian polyp (Figure 3.1A). It consists of a cylindrical body column with a tentacle ring and a dome-shaped hypostome containing the mouth on one end and a foot that anchors the animal to the substrate on the other. Hydra is composed of only two tissue layers: an outer ectodermal epithelium and an inner endodermal epithelium, separated by a basal lamina called the mesoglea. Body shape is regulated by contractile processes on the epithelial cells called myonemes, which

are oriented longitudinally along the head-foot axis in the ectoderm and circumferentially in the endoderm [53]. This simple anatomy, combined with the ability to regenerate a complete polyp from tissue pieces and from aggregates of body column cells, made *Hydra* an important model system for biologists and physicists alike to study regeneration, axis formation, and patterning [54].
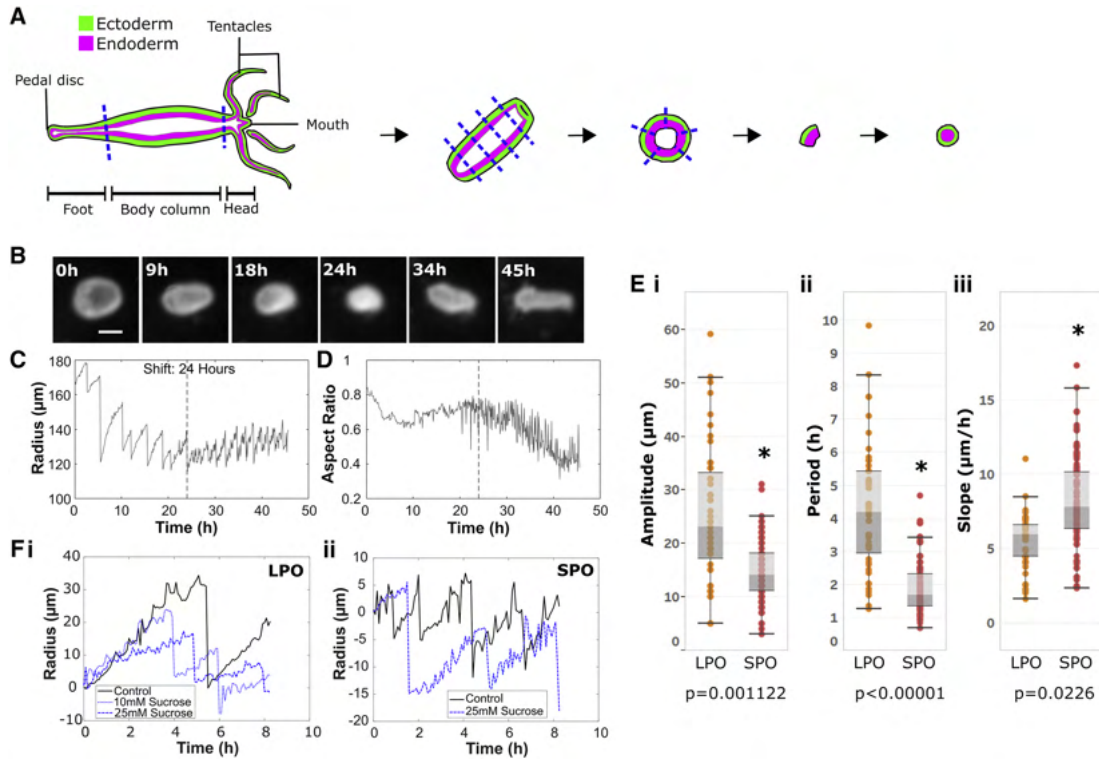
Figure 3.1: Generation of tissue spheres and quantification of oscillation dynamics. (A) Preparation of tissue pieces from a *Hydra* polyp (see Materials and Methods). (B) Representative images of regenerating tissue spheres at various time points during regeneration. In the 45 h image, the regenerated head with tentacles is to the left. Scale bar 150 μm. (C) Plot of effective radius, calculated as the radius of a circle with an area equal to that of the tissue piece, as a function of time for the sphere shown in B. (D) Plot of aspect ratio as a function of time for the same tissue sphere. Dashed line indicates the time of shift from LPO to SPO. (E) Box-whisker plots of i. amplitudes, ii. time periods and iii. slopes for LPOs and SPOs for body column tissue pieces regenerating in HM. (*) indicate a statistically significant difference from LPO (p < 0.05): amplitude p = 0.00112, period $p < 1 \times 10^{-5}$, slope p = 0.0226. (F). Plot of effective radius as a function of time at different sucrose concentrations in the external medium during i. LPOs and ii. SPOs.

One of the earliest attempts at modelling axial patterning in *Hydra* was made by Alfred

Gierer and Hans Meinhardt, who proposed a reaction-diffusion model consisting of a short range head activator, a long range head inhibitor, and a gradient for the activator source [21]. The model qualitatively explains pattern formation from a homogeneous starting state. However, a lack of quantitative experimental data has limited progress on validation and refinement of this and subsequent models [19]. Recently, the availability of a fully sequenced genome [55], various transgenic reporter lines [56, 57] and CRISPR genome editing tools [58] has allowed researchers to reexamine earlier models and studies of *Hydra* regeneration and gain new insights.

Here, we revisit a striking phenomenon that occurs during *Hydra* regeneration from tissue pieces [59] and aggregates of cells [21]. As they regenerate, both tissue pieces and aggregates form a hollow bilayered sphere with ectodermal cells on the outside and endodermal cells on the inside. These *Hydra* spheres undergo osmotically driven cycles of swelling and subsequent rupture, referred to as shape oscillations [60, 61]. The shape oscillations are sawtooth shaped, consisting of cycles of a long inflation phase followed by an abrupt deflation of the sphere due to local tissue rupture [62]. The inflation phase is caused by the uptake of water and the active pumping of sodium ions into the lumen of the sphere [63]. Initially, inflation is isotropic. The *Hydra* sphere's aspect ratio, defined as the ratio of the minor axis to the major axis of an ellipse fit to the sphere, is close to unity. As time progresses, the swelling becomes increasingly anisotropic: the aspect ratio decreases with sharp dips during deflation of the hollow sphere. The regenerating animal breaks spherical symmetry to establish a body axis and develops a mouth and tentacles by ∼48 h [61].

Previous studies have utilized different definitions and criteria for symmetry breaking. First, morphological, or shape symmetry breaking, refers to the tissue sphere becoming ellipsoidal, which has been quantified by shape analysis either through a decrease in the aspect ratio of an ellipsoid fit to the tissue sphere [64] or as changes in the Fourier modes of the two-dimensional contour of the tissue over time [61]. Second, biochemical symmetry breaking involves spatial patterning of morphogens such as Wnt3 [65], to specify a body axis and the

position of the head, foot, and tentacles. Finally, structural symmetry breaking involves the reorganization of supracellular structures such as myonemes [66]. Although these aspects have been studied individually and feedback between morphological and biochemical symmetry breaking has been proposed by some studies [19, 64, 67], the lack of tools to visualize morphogen gradients *in vivo* has prevented researchers from demonstrating a causal connection.

It has long been hypothesized that shape symmetry breaking coincides with or occurs shortly after the morphogen patterning proposed by Gierer and Meinhardt [21], leading models to use the time of oscillation pattern shift as the time of biochemical symmetry breaking. To the best of our knowledge, the mechanism underlying the oscillation pattern shift has not been determined. Sato-Maeda and Tashiro [62] were the first to probe the connection between shape oscillations and axis formation two decades ago. They reported the sawtooth shape of the oscillations and described a method of detecting shape symmetry breaking in cell aggregates by quantifying the divergence of orthogonal radii as the regenerating animal elongated along one axis. This approach represented a measure of body axis formation that could be quantitatively linked to other morphological fluctuations. Fütterer et al. [61] subsequently analyzed the shape of regenerating *Hydra* spheres originating from tissue pieces in greater detail, using Fourier decomposition to reveal three distinct temporal stages: 1) large-amplitude, long-period oscillations (LPOs) of the zeroth mode (size of the tissue piece); 2) small-amplitude, short-period oscillations (SPOs) of the zeroth mode associated with fluctuations of the second mode (elongation); and 3) strong increase in the second mode during contractions. They reported that shape anisotropy always occurred after the completion of LPOs, suggesting a correlation between oscillation dynamics and formation of the body axis as implied by shape symmetry breaking [61].

Hydra spheres derived from cell aggregates and from small tissue pieces exhibit similar oscillation dynamics. It was also reported that regenerating spheres reoriented their body axes in alignment with an applied temperature gradient regardless of their origin, so long as the

gradient was applied before the onset of SPOs [68]. Consequently, it was conjectured that both tissue pieces and cell aggregates begin from a homogenous state and must break symmetry *de novo*. The idea that the pattern shift occurs at the same time as biochemical symmetry breaking was supported by the finding that the time of pattern shift from LPO to SPO coincides with the emergence of critical scaling in the patch size distribution of the Hydra head-specific gene ks1 [68]. Secondly, β-catenin, which acts as a mechanotransducer in other model organisms [69], is involved in *Hydra* head specification via the canonical Wnt pathway [70, 71]. Because the timing of oscillation pattern shift at ~ 24 h [65] was com to the timing of the emergence of expression patches of Wnt3, the earliest known marker expressed during *Hydra* head regeneration [20, 72], in larger cell aggregates, Soriano et al. [64] concluded that the oscillation pattern shift must also coincide with the establishment of biochemical asymmetry. Consequently, it has been proposed that β-catenin may link the mechanical forces caused by tissue stretch or rupture with biochemical patterning in Hydra [64]. This remains to be experimentally verified, but the theory is attractive because of the known role of mechanotransduction pathways in a wide range of morphogenetic and developmental processes [5].

Thus, the pattern shift was regarded as a reliable and easily detectable marker of the morphological and biochemical symmetry breaking event in both aggregates and small tissue pieces [68]. Because of this apparent link, subsequent theoretical models by Soriano et al. [64] and Mercker et al. [19] coupled tissue mechanics with reaction-diffusion of morphogens to explain axis formation in Hydra. Both authors acknowledge that equating the time of oscillation pattern shift to that of biochemical symmetry breaking is a possible overestimation but use this assumption to constrain their models for lack of viable alternatives.

Recently, the assumption that both small tissue pieces and aggregates break symmetry *de novo* has been challenged. It was shown that spheres derived from small tissue pieces inherit the parent animal's myoneme organization and, as such, have structural asymmetry from the beginning [66]. How this structural asymmetry relates to morphological or biochemical

symmetry breaking remains elusive. However, it suggests that regenerating tissue spheres possess a predetermined body axis, which is incompatible with existing models of Hydra regeneration, assuming that small regenerating tissue fragments and regenerating aggregates both begin from an isotropic state and exhibit a true symmetry breaking event. In light of this apparent paradox in the existing literature, there is a need to determine the cause of the LPO-SPO shift and understand its relevance.

Here, we use *in vivo* manipulation and imaging to quantify shape oscillation dynamics and experimentally dissect the timing and triggers of the pattern shift. First, we demonstrate that both LPOs and SPOs are driven by osmotic pressure, suggesting that the observed differences do not arise from different swelling mechanisms but from changes in the local yield strength of the tissue spheres. Consistent with this idea, we find that the site of tissue rupture is random during LPOs but conserved during SPOs, suggesting the existence of a fixed mechanical weak point during SPOs. We demonstrate that this weak spot is the mouth. Furthermore, we show that mouth structure alone is insufficient to cause an oscillation pattern shift because tissue pieces derived from nerve-free animals, which are unable to open their mouths, regenerate fully but exhibit only LPOs. Additionally, tissue pieces derived from the heads of normal animals containing a functional mouth were found to exhibit only SPOs, whereas tissue pieces from the heads of nerve-free animals with a structurally normal but nonfunctional mouth only exhibit LPOs. Together, these experiments demonstrate that the shift in oscillation pattern observed in regenerating *Hydra* tissue pieces is caused by the onset of mouth function. Therefore, the pattern shift is an indicator of active control of mouth opening, providing an easily observable readout for an important regeneration milestone. In addition to providing a mechanistic explanation for shape oscillation dynamics, this study also allowed us to estimate a lower bound for the tissue yield strength, a parameter which may prove useful for future models of *Hydra* regeneration.

3.4   Materials and Methods

3.4.1   *Hydra* strains and culture

Hydra vulgaris strain AEP, *Hydra vulgaris* (formerly *Hydra magnipapillata* strain 105) strain sf-1 (temperature-sensitive interstitial stem cells), *Hydra vulgaris* strain A10 (chimera consisting of *Hydra vulgaris* epithelial cells and sf-1 interstitial cells) [73], and *Hydra vulgaris* "watermelon" (AEP expressing GFP in the ectoderm and DsRed2 in the endoderm) [57] were used for experiments. Polyps were kept in *Hydra* medium (HM) composed of 1 mM $CaCl_2$ (Spectrum Chemical, New Brunswick, NJ), 0.1 mM $MgCl_2$ (Sigma-Aldrich, St. Louis, MO), 0.03 mM KNO3 (Fisher Scientific, Waltham, MA), 0.5 mM $NaHCO_3$ (Fisher Scientific, Hampton, NH), and 0.08 mM $MgSO_4$ (Fisher Scientific) prepared with MilliQ water, with pH between 7 and 7.3, at 18℃ in a Panasonic incubator (Panasonic MIR-554, Kadoma, Japan) in the dark. The *Hydra* were fed three times per week with *Artemia* nauplii (Brine Shrimp Direct, Ogden, UT). Animals were cleaned daily using published procedures [74].

3.4.2   Generation of nerve-free *Hydra*

Nerve-free *Hydra* were generated using either of two methods. Watermelon animals were made nerve free as described by Tran et al. [75]. Briefly, the animals were incubated in 0.4% colchicine (AcrosOrganics, Thermo Fisher Scientific, Waltham, MA) inHM for 8 h in the dark. This 8 h incubation was then repeated 3 weeks after the first treatment. Colchicine-treated *Hydra* are susceptible to bacterial infection, so the animals were kept in HM supplemented with 50 μg mL^{-1} rifampicin (EMD Millipore, Burlington, MA) at 18℃ in the dark in the incubator. Nontransgenic nerve-free animals were generated by heat shock treatment of the sf-1 and A10 strains [73, 76, 77]. Sf-1 and A10 animals were heat shocked in an incubator at 29℃ in the dark for 48 h and then moved back into the 18℃ incubator. All nerve-free animals were force fed and "burped" as per the protocol described in Tran et al. [75].

3.4.3 Preparation of tissue pieces

Tissue pieces were cut with a scalpel (Sklar Instruments, West Chester, PA) from the body columns of adult non-budding *Hydra* starved for 24 h, as shown in Fig 3.1A. The head was amputated immediately below the tentacles. A second cut was made above the foot to isolate the body column. Depending on the size of the resulting body column piece, one to three cross-sectional cuts were made to extract rings. The rings were cut into four or more pieces and allowed to round up in HM for ~2 h (measured from the time of initial excision of the body column piece). Once rounded up, tissue pieces were selected by size (<200 μm radius) by visual examination under a stereo microscope for use in experiments (Figure 3.1 A).

3.4.4 Preparation of head and foot tissue pieces

Head tissue pieces were prepared under a stereo microscope. The animals' heads were removed immediately below the tentacle ring, and then the tentacle bases were excised. The remaining head tissue pieces were given ~1 h to round up and placed individually into custom-made agarose wells for time-lapse imaging. Foot tissue pieces were prepared by cutting the animals immediately above the basal disk and allowing the resulting tissue pieces to round up for 2 h. In both cases, rounded tissue pieces of the same approximate size as body column tissue pieces were selected for imaging.

3.4.5 Imaging of shape oscillations

Regenerating tissue pieces were placed in agarose wells made using a 1% solution of agarose or low melting point agarose (Invitrogen, Carlsbad, CA) in HM. The two types of agarose were used interchangeably. To make the wells, molten agarose solution was poured into 30 mm Falcon petri dishes (Thermo Fisher Scientific), and a comb with 1-mm-wide teeth was placed vertically into the dishes to create wells. Once the agarose had solidified, the comb was removed,

the wells were filled with HM, and the tissue pieces were moved into the wells using a pipette. Imaging was accomplished using an Invitrogen EVOS FL Auto 2 microscope (Thermo Fisher Scientific) and the Invitrogen EVOS FL Auto 2.0 Imaging System software. Images were acquired every 5 min and stored as Tagged Image File Format files. Viability of the tissue pieces was assayed by observing the presence of a body axis at 48 h and the formation of tentacles and mouth opening upon presentation of *Artemia* at 96 h.

3.4.6 Altering osmolarity of *Hydra* medium

To test the effect of changes in osmotic pressure on regenerating tissue pieces, tissue pieces were prepared and imaged as described above. However, the tissue pieces were kept in sucrose-supplemented HM for imaging instead of HM. Sucrose (Sigma-Aldrich) was added to HM to final concentrations of 10 or 25 mM. Rifampicin (EMD Millipore) was added to a final concentration of $50\,\mu\mathrm{g\,mL}^{-1}$ to prevent bacterial growth in the presence of sucrose.

3.4.7 Injections of microbeads and rupture site tracking

Tissue pieces were incubated at room temperature until at least 5 h after cutting to allow them to round up and form an internal cavity. An agarose trough for microinjection was cast as previously described [78]. Hollow tissue spheres were placed in the trough in HM and injected with 1 μm green fluorescent (excitation/emission: 468/508 nm) microbeads (Thermo Fisher Scientific G0100) using a WPI Pneumatic PicoPump (PV 820) (Sarasota, FL) and needles pulled using a Sutter Instrument P-1000 (Novato, CA). Successfully injected spheres were placed in agarose wells and imaged for 24 h as described above. The resulting videos were used to determine the location of rupture events by tracking the locations of ejection of fluorescent beads relative to a fixed feature on the sphere. The smaller of the two angles between the fixed feature and the rupture location was recorded.

3.4.8 Visualization of myoneme arrangement in the head

Nerve-free Hydra prepared by heat shock treatment of strain A10 and untreated controls were fixed and stained with rhodamine-phalloidin (Biotium, Fremont, CA). The polyps were relaxed in 1 mL of 1 mM linalool (Sigma-Aldrich) in HM for 10 min [23] and then fixed in 4% paraformaldehyde (Thermo Fisher Scientific) in HM for 20 min at room temperature. They were washed with HM thrice for 10 min each before being incubated overnight at 4℃ in rhodamine-phalloidin diluted 1:100 in HM. The fixed stained samples were washed 5 times for 10 min each with HM. They were then placed on 22x40 mm glass coverslips (Corning, Corning, NY), which had a piece of double-sided tape (3M, Maplewood, MN) running along the short edges of the coverslips. These coverslips were then sealed by placing 22x22 mm glass coverslips (Fisher Scientific) on top, and the samples were imaged using an Olympus IX81 inverted microscope (Olympus Corporation, Tokyo, Japan) with an ORCA-ER camera (Hamamatsu Photonics, Hamamatsu, Japan). Slidebook version 5 (Intelligent Imaging Innovations, Denver, CO) was used to interface with the microscope and acquire z-stacks. Maximum intensity projections of the z-stacks were used to determine the orientation of the myonemes.

3.4.9 Oscillation analysis

Images collected using the EVOS microscopes were opened in ImageJ (http://imagej.nih.gov/ij/; National Institutes of Health, Bethesda, MD), and full regeneration was verified. Full regeneration was defined as the regenerated tissue piece exhibiting a well-defined body axis, head formation, and tentacle growth. Only tissue pieces that showed full regeneration were included in further analysis. The obtained images were processed to extract the radius of the tissue piece as a function of time as described in the next paragraph. Only those tissue spheres whose minimum radius was ≤150 µm were included in further analysis. This cutoff was chosen based on the literature, in which it has been suggested that spheres with <200 µm

average minimum radius, defined as the average of the minimum radi across oscillation cycles for a single tissue sphere, exhibited a pattern shift [64].

Each image set was analyzed using built-in functions in a custom Python script (Python 3.7.0; Python Software Foundation). The script first applies morphological image opening and closing to distinguish the sphere from the background, followed by watershed segmentation to detect and eliminate ejected cell debris (Figure 3.4). If the script failed to segment the raw image set, debris was removed from the images by manually tracing over the debris in ImageJ before analysis. For each image in a set, the script traces the boundary of the regenerating tissue to determine its area. Effective radius is calculated as the radius of the circle having the same area as the tissue piece. Shape is approximated by fitting an ellipse to the two-dimensional contour of the tissue piece and recording major and minor axes to determine the aspect ratio. Effective volume of the tissue piece was determined as the volume of an ellipsoid obtained by revolution of the fit ellipse about its major axis as described in Soriano et al. [68].We found that the effective radius and the effective volume, normalized so that the minimum radius and volume are unity, qualitatively show the same temporal dynamics (Figure 3.5). Subsequent processing and analysis of the data were carried out in MATLAB 2017b (MathWorks, Natick, MA). The code is available online at https://github.com/Collinslab-swat/Oscillation-Analysis.git. The existence and timing of oscillation pattern shift in a data set was determined by having five researchers independently examine the radius-time plots for the data set and provide an estimate of the presence and timing of the shift. The data set was accepted as having a shift at a particular time if there was consensus of at least four of the researchers, defined as all scores being within a 4 h interval.

After shift presence and timing were determined, the amplitude, time period, and slope of each oscillation were extracted. The amplitude was defined as the difference between maximum and minimum radius during the inflation phase. The time period was defined as the time difference between the beginning of the inflation phase and end of the deflation phase. The

swelling rate (slope) was obtained from a linear fit to the inflation phase of the oscillation.

As individual oscillations within a single biological replicate cannot be considered independent and their parameters are not normally distributed, we calculated the median values for each biological replicate and used these as inputs in our statistical analysis.

A two-sided Mann-Whitney U test was used to determine whether two sets of oscillation parameters originated from the same distribution. A p-value of 0.05 or lower rejects the null hypothesis that the two samples were drawn from the same distribution. For all conditions other than body column tissue pieces taken from wild-type animals regenerating in HM, the oscillations were classified as LPO or SPO based on comparison to wildtype LPO and SPO time periods. We used time periods for classifying an oscillation as LPO or SPO because the time periods are fairly consistent across biological replicates and the LPO time period distribution has very little overlap with the SPO time period distribution.

3.4.10 Calculation of the yield strength of the tissue

The *Hydra* tissue sphere was treated as a linear elastic hollow spherical shell. Then, the elastic pressure experienced by the sphere is given by the following:

$$P = 2Eh\frac{A}{R_0^2(1-\nu)}$$

Here, E is the Young's modulus of the tissue, ν is the Poisson's ratio, h is the thickness of the shell, A is the amplitude of the sphere at the time of rupture and R_0 is the minimum radius of the sphere. The tissue was assumed to be incompressible, so $\nu = 0.5$. However, the results are not strongly dependent on the choice of ν. For example, if $\nu = 0.25$ is used, as in Kücken et al. [60], the pressure is only reduced by a factor of 1.5. For the Young's modulus, a value of 185 $\mathrm{N\,m^{-2}}$ was used, based on experiments by Veschgini et al. [79], who measured the response of tissue spheres to uniaxial compression. The median values of minimum radius and amplitude

were used, with R_0 = 119 μm and A = 28 μm for LPOs and A = 15.5 μm for SPOs, respectively. The shell thickness, h, was obtained from images presented in Buzgariu et al [80] and was found to be approximately 25 μm. The size of the hole caused by rupture was estimated from images that captured debris leaving the tissue sphere during a rupture event. The narrowest portion of the debris immediately adjacent to the sphere was averaged over three events and treated as an upper limit approximation of the size of the exit point, yielding a mean diameter of 26 μm, corresponding to 1-2 cell diameters.

3.4.11   Comparison of the oscillation parameters to previously published values

Published histograms of the slopes during LPOs and SPOs were taken from Soriano et al. ([64]. Using the freely available WebPlotDigitizer (https://automeris.io/WebPlotDigitizer/), we converted the histograms into frequency distribution tables, calculated medians for the slopes for LPO and SPO, and compared those to the medians we calculated for our data. Because histograms were not available for time periods and amplitudes, we used other published plots of radius and volume over time to obtain time periods and amplitudes. The median time periods were obtained after digitizing the volume over time plot in Soriano et al. [68]. Median amplitudes were also obtained in the same manner from the radius over time plot in Kücken et al. [60]. We used medians as the summary statistic for the data because the data distributions were nonnormal.

3.5   Results and discussion

As a freshwater animal, *Hydra* experiences a continuous inflow of water from the medium, through the tissues and into the gastric cavity [81, 82]. The resulting internal pressure is periodically relieved by opening of the mouth [83]. Regenerating *Hydra* spheres initially

lack a mouth and therefore must relieve pressure from water accumulation by passive tissue rupture. This creates an oscillatory pattern of gradual osmotically driven swelling and rapid deflation due to tissue rupture, followed by healing of the rupture site. These cycles of swelling and rupture show an abrupt shift in oscillation pattern from LPOs to SPOs, coincident with a change in the aspect ratio of the regenerating *Hydra* sphere.

3.5.1 LPOs and SPOs have distinct oscillation parameters but a common driving mechanism

To examine the cause of the observed shift in oscillation pattern, we prepared tissue spheres (Figure 3.1 A) and imaged them over the course of regeneration (Video S1). We only analyzed data from tissue spheres that regenerated fully,showing a defined body axis with head and tentacles (Figure 3.1 B). A shift in oscillation pattern was observed to coincide with a gradual decline in aspect ratio (Figure 3.1, C and D), as previously reported [60, 61, 64]. From these radius-versus-time plots (Figure 3.1 C), we extracted amplitude, period, and swelling rate (slope) for LPOs and SPOs (see Materials and Methods) and found all parameters to differ significantly between the two oscillation types (Figure 3.1 E). A comparison of our data to the literature [60, 64] using the medians of the oscillation parameters (see Materials and Methods) shows similar differences in these three parameters between LPO and SPO.

The median amplitudes observed for LPOs and SPOs (Table 3.1) correspond to changes of ∼25% and 15%, respectively, in the radius of the tissue spheres. Because a sphere's radius scales linearly with the linear size of the epithelial cells, we infer that the cells undergo linear deformations of 25% during LPOs and ∼15% during SPOs. Although these are significant cell deformations, similar and more extreme deformations are observed during mouth opening in intact polyps over the course of tens of seconds [83]. These numbers illustrate the remarkable deformability of *Hydra* tissue.

Previous studies and models assumed that both LPOs and SPOs are driven solely by

osmotic pressure [19, 60]. However, this was only experimentally tested for LPOs [60]. To verify that SPOs are also osmotically driven, we incubated tissue pieces in hypertonic medium made by adding 10 or 25 mM sucrose to HM. Because the osmolarity between the inside and the outside of a tissue sphere equilibrates after several rupture events, we began incubation either 2 h post-amputation to probe the effect of altered osmotic pressure on LPOs or 24 h post-amputation to probe its effect on SPOs. Consistent with previous work [60], we observed a concentration-dependent decrease in swelling rates during the LPO cycle in the 2-h post-amputation treatments (Table 3.1). Similarly, we obtained a decrease in slope in the 24-h post-amputation treatment with 25 mM sucrose. Moreover, the increase in slope from LPOs to SPOs was not affected by sucrose concentrations (Table 3.1).

This suggests that SPOs are also primarily osmotically driven and that the increased rate of inflation is due to a secondary mechanism, such as a change in tissue properties associated with regeneration (e.g., an increase in tissue permeability to water or an increase in the number or activity of ion pumps), as previously suggested [61]. As slopes are even further increased in head tissue piece oscillations, the change may be linked to the development of a head, which has been reported to differ in terms of cell composition and matrix thickness [84].

The decrease in maximum amplitude of SPOs compared to LPOs indicates that the pressure required to trigger a rupture event has decreased. This can be explained either by the weakening of the tissue's tearing strength (globally or locally) or the rupture becoming an actively controlled process. Both of these are attributes of the *Hydra* mouth. The mouth is a structural weak spot because it has a thinner mesoglea and an absence of myonemes running across it [84]. The mouth also allows for active pressure release in the intact polyp through the control of the nervous system [83]. Soriano et al. [68] proposed the first possibility, suggesting that the formation of a protomouth created a weak spot, but this idea was not tested experimentally.

Table 3.1: Summary of oscillation parameters

Parameters are reported as the median of biological replicates with the first and third quartiles.

[a] Indicates significant difference from wild-type SPOs at $p < 0.01$.
[b] Indicates significant difference from wild-type SPOs at $p < 0.05$.
[c] Indicates significant difference from wild-type LPOs at $p < 0.01$.
[d] Indicates significant difference from wild-type LPOs at $p < 0.05$.

	Period length (h)	Amplitude (μm)	Slope (μm/h)	Number of biological replicates
Wild-type (HM) LPO	$4.2\ (3.7, 5.8)^{a}$	$28.0\ (21.0, 36.6)^{a}$	$6.3\ (5.6, 7.1)^{b}$	15
Wild-type (HM) SPO	$1.8\ (1.5, 1.9)^{c}$	$15.5\ (13.0, 19.7)^{c}$	$7.5\ (6.7, 9.8)^{d}$	15
Sucrose 10mM 2h	$2.3\ (1.9, 3.0)^{a,c}$	$13.5\ (10.9, 19.1)^{c}$	$4.9\ (4.4, 6.3)^{a}$	14
Sucrose 25mM 2h	$3.0\ (2.8, 4.3)^{a}$	$14.3\ (11.7, 19.8)^{c}$	$3.5\ (3.1, 4.1)^{a,c}$	17
Sucrose 25mM 24h	$4.1\ (2.7, 4.5)^{a}$	$21.2\ (13.5, 29.2)$	$4.0\ (3.6, 5.0)^{a,c}$	15
Wild-type head tissue piece	$1.1\ (0.9, 1.4)^{a,c}$	$8.7\ (6.3, 12.1)^{b,c}$ §	$9.7\ (7.4, 10.9)^{d}$	4
Foot tissue piece	$2.8\ (2.3, 4.0)^{a}$	$21.0\ (14.2, 30.3)$	$7.6\ (5.5, 7.9)$	5

3.5.2 Rupture site becomes constant as regeneration progresses

To determine whether a fixed rupture site consistent with a permanent mechanical defect appears during regeneration, we used fluorescent microbead injections to visualize the rupture site in oscillating tissue spheres (Figure 3.2, A and B). We observed that cell debris was frequently ejected from spheres throughout the regeneration process and thus conclude that the introduction of microbeads does not represent a significant alteration to natural behavior (Figure 3.7). Because rupture events can no longer be visualized after all beads are ejected from a sphere, we injected 5 h post amputation to track rupture events during LPOs or 24 h post amputation to track ruptures during SPOs. We observed that rupture sites are randomly distributed in spheres injected at 5 h (Figure 3.2 Ci) but are significantly more localized in spheres injected at 24 h (Figure 3.2 Cii).We compared rupture site locations for both LPOs and SPOs to data drawn from a uniform distribution using a two-sample Kolmogorov-Smirnov test and uniform distribution (p = 0.9702), whereas the 24 h data are (p = 1.0047×10^{-7}). This suggests that a mechanical weak spot in the tissue sphere forms as regeneration proceeds.

To confirm that this structural weak point corresponded to the *Hydra* mouth, we tracked ruptures in excised head tissue pieces. These were created by excising the intact mouth of the parent animal and a small amount of surrounding tissue, then allowing the piece to round in the same way as a body column tissue piece (Figure 3.2 Di). Head tissue pieces are not viable long term because of being composed mainly of terminally differentiated cells, but they remain healthy for at least 24 h and exhibit trackable oscillations during that time (Figure 3.2 Dii). They also retain the parental mouth structure, which can be visualized via phalloidin staining (Figure 3.8). We found thatthese head piece spheres had an invariant rupture site (Figure 3.2 Ciii), supporting the idea that the emergence of a fixed rupture site is coincident with mouth development during regeneration. Finally, to confirm a link between the mouth and oscillation dynamics, we analyzed the oscillations of head pieces and found that they only exhibit SPOs as seen from the distribution of time periods (Figure 3.2 Dii; Table 3.1). These data demonstrate
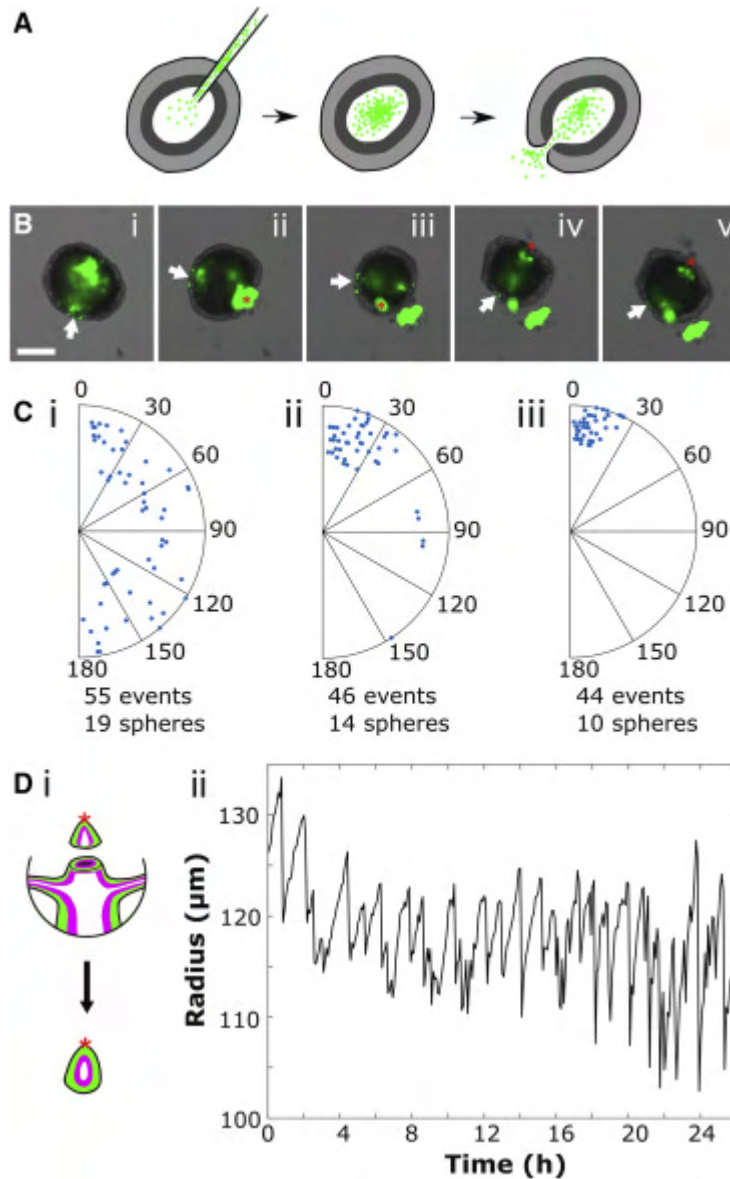
Figure 3.2: Rupture site becomes constant with head development. ((A) Experiment schematic showing injection of fluorescent microbeads into a hollow sphere. Beads are ejected from the sphere during rupture events. (B) Representative image series of sphere ejecting beads during successive ruptures. White arrow indicates the feature used to track rotation, red asterisk represents observed rupture site (see Materials and Methods). Scale bar 100 μm. (C) Location of the rupture site relative to the first rupture, each radius representing a single sphere. i. Beginning 5 h after cutting. ii. Beginning 24 h after cutting. iii. Head tissue pieces, containing the mouth of the parent animal. (D) i. Schematic illustrating the creation of a head tissue piece. Red asterisk indicates location of the mouth. ii. Representative oscillation plot of a head tissue piece.

that the presence of a mouth in a tissue piece is sufficient for SPOs.

Because it had been proposed that the aboral pore acts as a second weak point in the intact animal that may be used for pressure regulation [85], we also imaged foot tissue pieces containing the entire basal disk (Figure 3.1 A). Foot tissue pieces showed oscillation parameters with a greater similarity to LPOs than to SPOs (Table 3.1). The statistically significant difference in period between foot tissue pieces and SPOs indicates that the presence of an aboral pore does not increase rupture frequency in the same way the presence of a mouth does. Thus, the aboral pore does not play a role in regulating osmotic pressure during regeneration. We suspect that the similarity in the swelling rate between the foot piece and body tissue piece SPOs results from a difference in tissue composition in the foot. Both the hypostomal region and the basal disk have significantly higher proportions of epitheliomuscular and nerve cells than the body column [86], which may cause differences in mechanical properties or permeability.

In summary, these results support the hypothesis that ruptures during LPOs are caused by osmotically driven inflation until the yield strength of the tissue is reached, resulting in random rupture locations. In contrast, SPOs are caused by the development of a mouth structure, creating a permanent, localized weak point on the sphere. This is consistent with previous observations that insertion of head tissue into cell aggregates decreases the time required for a shift to SPOs to occur [64]. The presence of a head organizer would allow the aggregate to more rapidly define a head and develop a mouth, resulting in a faster oscillation pattern shift. Whether the forming mouth acts solely as a mechanical defect, as previously suggested [68], or actively regulates osmotic pressure cannot be distinguished based on these data.

3.5.3   Mouth function is required for a shift to SPO

To determine whether the mouth plays an active osmoregulatory role in regenerating tissue spheres, we decouple mouth function from mouth structure by examining nerve-free *Hydra*, which are capable of complete regeneration but are unable to open their mouths to relieve

pressure or respond to chemical stimuli [81, 87, 88]. In contrast to normal animals, nerve-free *Hydra* take on a characteristic bloated appearance [75] (Figure 3.3 A) because of their inability to relieve internal pressure by mouth opening. The mouth appears morphologically normal in nerve-free animals (Figure 3.3 B), suggesting that lack of function is caused by the absence of neurons and thus an inability to sense pressure [89]. Body column tissue spheres derived from nerve-free animals showed only LPOs, with a period slightly longer than LPOs in wild-type spheres (Figure 3.3 C; Table 3.2). The small difference in parameters may be due to differences in tissue strength given that nerve-free animals lack all cell types derived from the interstitial cell lineage: neurons, gland cells, and nematocytes [90]. Although it has been suggested that nerve-free animals may use an alternate, slower regeneration pathway for regeneration than enervated animals (43), we observe that nerve-free animals are able to form a head and tentacles within 72 h without ever exhibiting SPO behavior (Figs. 3 C and S3; Video S2). Thus, nerve-free animals break shape symmetry and have a clearly specified axis without ever experiencing SPOs.

Because it is still possible that the development of mouth structures is delayed in nerve-free *Hydra*, we use excised head pieces from nerve-free *Hydra* containing the mouth to fully decouple mouth structure from mouth function. If the presence of a mouth structure was sufficient to increase rupture frequency, we would expect to observe SPOs in spheres derived from nerve-free head pieces as we do in untreated wild-type head pieces (Figure 3.2 D). Alternatively, if active control of the mouth structure is necessary for SPOs to occur, nerve-free head pieces should not show SPOs. We observe that spheres from nerve-free head pieces show only LPOs (Figure 3.3 D; Table 3.2) and therefore conclude that mouth function is a requirement for the occurrence of SPOs.

Taken together, these data demonstrate that the shift in oscillation pattern observed in regenerating *Hydra* tissue spheres is caused by the formation of a functional mouth and its use in osmoregulation. A tissue sphere derived from a wild-type polyp initially exhibits LPOs

Table 3.2: Oscillation parameters for various experimental conditions

Parameters are reported as median of biological replicates with the first and third quartiles.

[a] Indicates significant difference from wild-type SPOs at $p < 0.01$.

[b] Indicates significant difference from wild-type SPOs at $p < 0.05$.

[c] Indicates significant difference from wild-type LPOs at $p < 0.01$.

[d] Indicates significant difference from wild-type LPOs at $p < 0.05$.

	Period length (h)	Amplitude (μm)	Slope (μm/h)	Number of biological replicates
Wild-type (HM) LPO	4.2 (3.7, 5.8)[a]	28.0 (21.0,36.6)[a]	6.3 (5.6, 7.1)[b]	15
Wild-type (HM) SPO	1.8 (1.5, 1.9)[c]	15.5 (13.0, 19.7)[c]	7.5 (6.7, 9.8)[d]	15
Wild-type head tissue pieces	1.1 (0.9, 1.4)[a,c]	8.7 (6.3,12.1)[b,c]	9.7 (7.4,10.9)[d]	4
Nerve-free body column pieces	6.6 (5.6, 9.3)[a,c]	28.5 (25.8, 37.7)[a]	4.1 (3.3, 4.5)[a]	11
Nerve-free head tissue pieces	3.2 (2.8,4.0)[a]	20.8 (16.0, 29.9)	6.5 (5.5, 7.8)	4
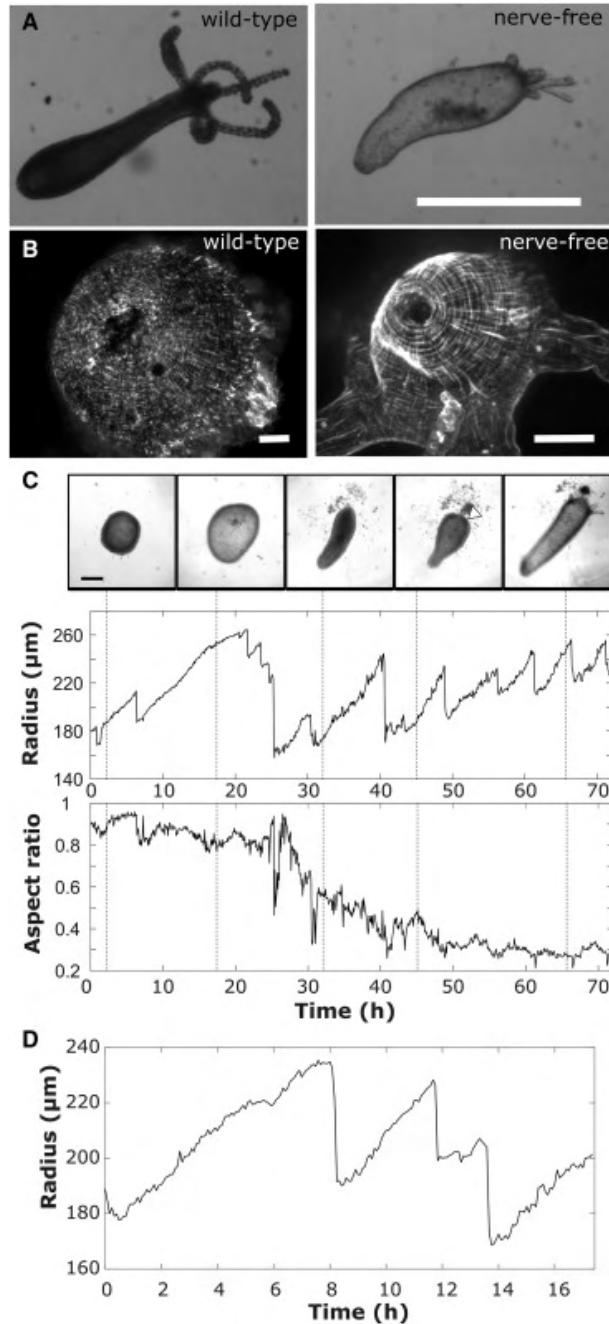
Figure 3.3: Mouth opening impacts oscillation dynamics. (A) Comparison between wild-type and nerve-free polyps, showing characteristic bloated phenotype of nerve-free *Hydra* (scale bar 1 mm). (B) Comparison of myoneme organization in the hypostome of wild-type and nerve-free animals (scale bars 50 μm). (C) Full regeneration of a nerve-free tissue sphere showing only LPOs. Representative images are taken at times indicated on radius and aspect ratio plots. Scale bar 200 μm. (D) Representative oscillation plot of nerve-free head tissue sphere showing only LPOs.

in which rupture is dictated by the yield strength of the tissue. Rupture events in this regime are randomly located because mechanical failure is equally likely to occur at any point on the sphere. Approximately 24 h into the regeneration process, we observed the development of a functional mouth, which allows for active osmoregulation, causing the shift to SPOs.

3.5.4 Implications for theoretical models of *Hydra* regeneration

Various attempts have been made to model axis determination from a homogeneous initial state in *Hydra* spheres. The core of these models lies in some form of feedback between morphogen concentrations and mechanical properties of the tissue such as elasticity. The dynamics of the morphogen concentrations are modeled using the Gierer-Meinhardt model [21], whereas feedback between mechanics and the morphogens is modeled using a relation between tissue stretch and morphogen diffusion. In the model proposed by Soriano et al. [64], this takes the form of a linear relationship between tissue strain and the diffusion coefficient of one of the morphogens. Axis formation is posited to occur when a stable morphogen gradient is established (a consequence of the diffusion coefficient exceeding a certain threshold [64]), which makes the timescale for gradient formation much shorter than the timescale for shape oscillations. In a more recent model by Mercker et al. [19], the local diffusion coefficient is a function of the local area strain of the tissue, and the elastic modulus is a function of morphogen concentration. This allows for a growth instability: high local strain causes accumulation of the morphogen and morphogen accumulation allows for higher local strains in response to the same stress [19].

To date, there are no quantitative experimental data on concentration patterns of morphogens, their diffusion constants, or the feedback between morphogen concentration and mechanical properties in *Hydra*. Therefore, models rely entirely on relations between morphological parameters, such as swelling rate, initial tissue size, and the time of shape symmetry breaking, to constrain model parameters and validate predictions. The results presented here

force us to reconsider the assumption that the time of shape and biochemical symmetry breaking always coincide with the time of the oscillation pattern shift from LPO to SPO. Nerve-free tissue pieces only exhibit LPOs but nevertheless break shape symmetry and specify a body axis (Figure 3.3 C; Figure 3.6). This demonstrates that one of the key observables used to constrain the existing models is not universally applicable. Instead, we show that the shift in the oscillation pattern is caused by a change in local yield strength of the tissue because of mouth formation, a property whose variation is not considered by existing models.

We estimate the local yield strength of the tissue by treating it as an elastic shell (see Materials and Methods). The order of magnitude estimate is made using only quantities that can be measured or calculated from experimental data presented here or elsewhere in the literature, except for Poisson's ratio, which does not affect the order of magnitude (see Materials and Methods). The estimated elastic pressure inside the sphere at the time of rupture is on the order of 20 Pa during LPOs. Because the pressure scales linearly with oscillation amplitude (see Materials and Methods) and the SPO amplitude is approximately half the LPO amplitude, the pressure at the time of rupture during SPOs is $\sim$10 Pa acting on an area of the order of two to three cell diameters across. Therefore, the elastic force must be on the order of a few nano-Newtons at the time of rupture during SPOs.

The magnitude of this force is comparable to that exerted by myonemes to create a mouth opening[83] and to the separation force associated with tight junctions involved in cell-cell adhesion [91]. Although the sources of the elastic forces estimated here for SPOs are different from those involved in mouth opening, they act on the same tissue producing the same effect (breaking cell-cell contacts to create an opening), suggesting that the estimates are reasonable. We thus provide an experimentally determined value that can be used to constrain the maximum stress associated with tissue rupture in models.

We can infer that axis specification must precede mouth function. Previous work shows that Wnt3 expression occurs by 24 h in large aggregates that give rise to multiple body axes

[65] or by 1.5 h after amputation in a decapitated animal [72]. Because a tissue piece retains more structure than an aggregate but less than a decapitated animal, we expect Wnt3 signaling to be established between these times. By combining these constraints with the time of the oscillation pattern shift as an upper bound, we can improve our estimate of the time of axis specification over that used in previous models.

Finally, although this and other recent works [60, 61, 66] have focused on regenerating spheres originating from tissue pieces, the oscillation behavior of spheres originating from cell aggregates should be revisited. A direct comparison of the results from these two starting scenarios is likely to provide further insights into the mechanisms that drive regeneration and patterning. Exploring these possibilities and leveraging them to improve existing models should be the next step in our attempt to understand axis specification in *Hydra*.

3.6   Conclusion

During *Hydra* regeneration from small tissue pieces or aggregated cells, a hollow bilayered sphere forms that undergoes dramatic shape oscillations. A switch in oscillation pattern, from long period, large amplitude to short period, small amplitude oscillations occurs approximately one day into regeneration. As previous explanations for the shift in oscillation pattern have recently been invalidated, we reexamined this fundamental process during *Hydra* regeneration from tissue spheres and demonstrate that the oscillation pattern shift is a direct consequence of the onset of mouth function and its use in osmoregulation. This allows us to infer the development of an important physiological function through a morphological read out. The results from this work also enable the field to re-examine and improve existing models of *Hydra* regeneration that rely on the concurrence of the shift in oscillation pattern and decrease in aspect ratio to constrain model parameters.

3.7 Acknowledgments

3.8 Supplemental Material

The supplemental material below can also be found online at https://doi.org/10.1088/1478-3975/ac2f29.

3.8.1 Supplemental Figures
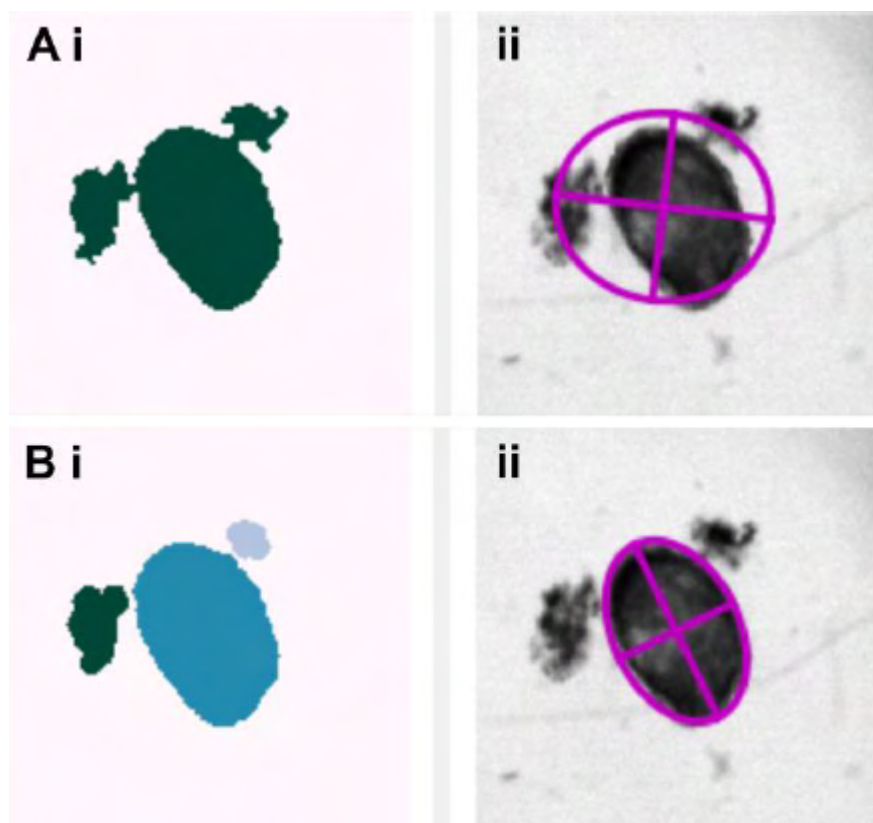
Figure 3.4: Representative images from image analysis of regenerating tissue spheres.
(A) Prior to image segmentation using watershedding. i. Debris and tissue piece identified as single object. ii. Raw image with fitted ellipse. (B) After image segmentation using watershedding i. Debris and tissue piece identified as separate objects. ii. Raw image with fitted ellipse. The ellipse fit in the bottom right panel was used for analysis.
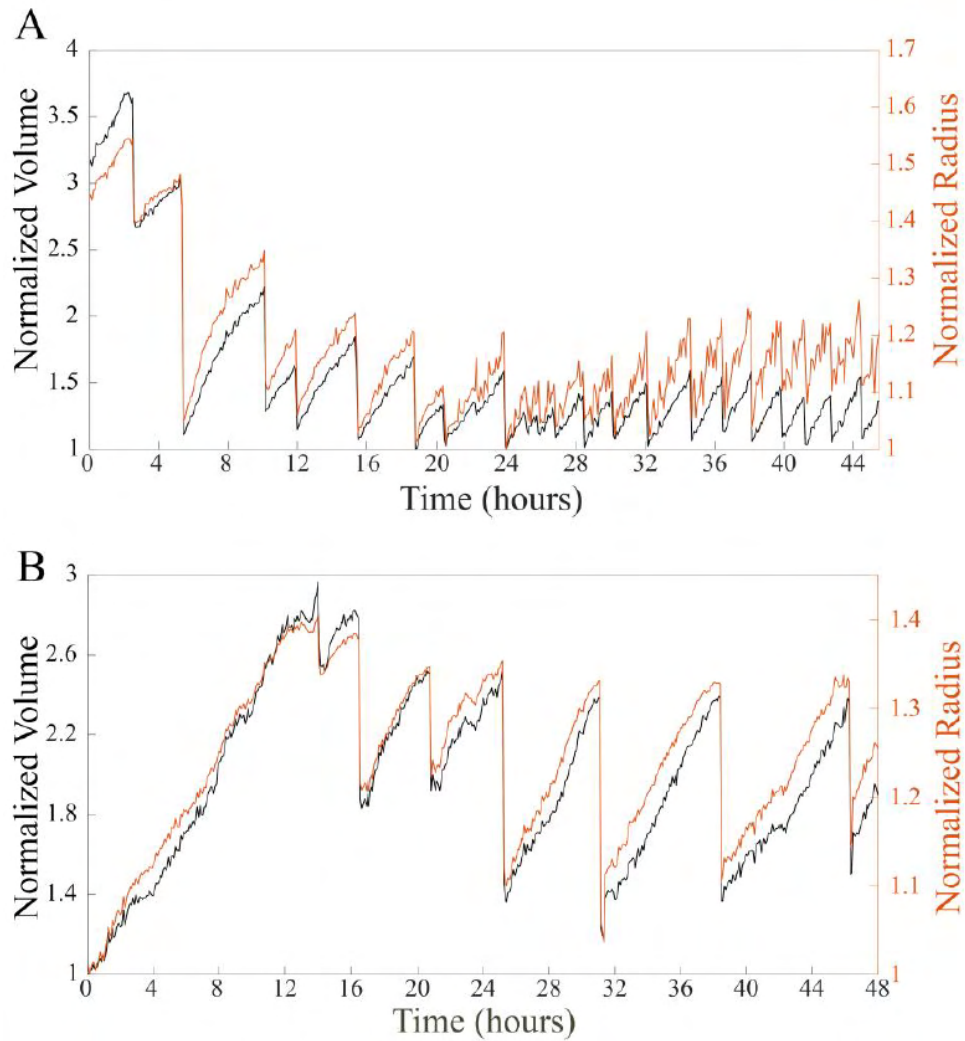
Figure 3.5: Effective radius and volume dynamics are not qualitatively different. (A) Wild type tissue piece displaying an oscillation pattern shift. Radius plotted in red, calculated volume plotted in black. Both were normalized by dividing by the respective minimum values. (B) Tissue piece from a nerve-free animal only displaying LPOs. Normalized radius plotted in red, normalized calculated volume plotted in black.
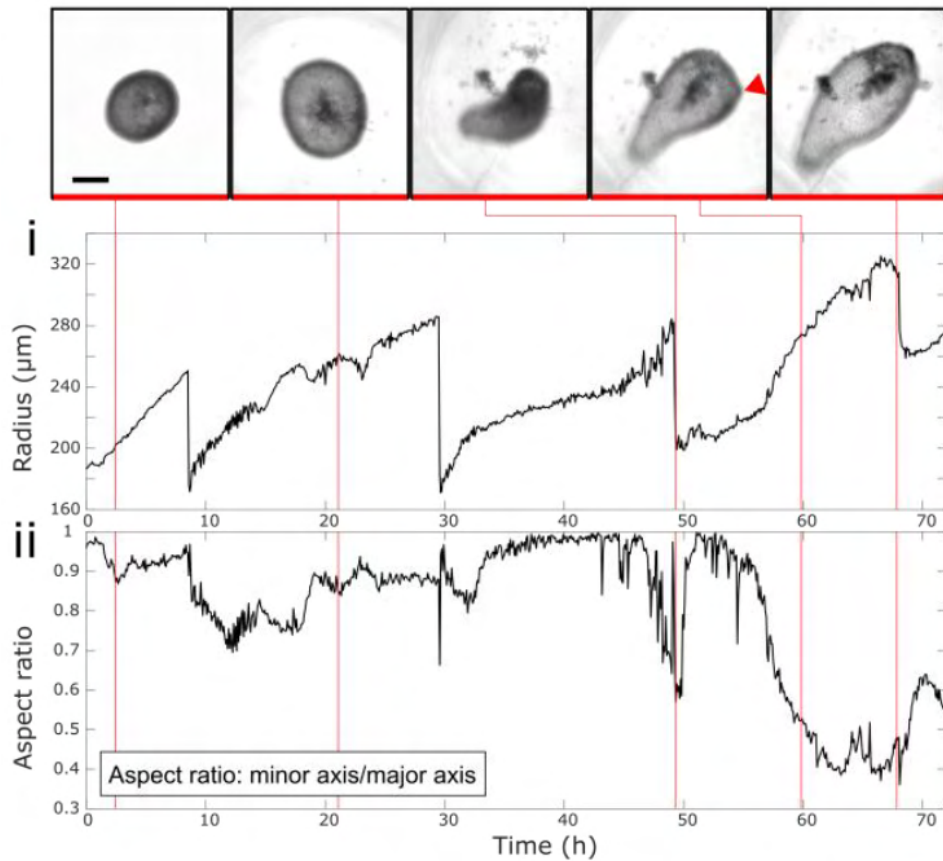
Figure 3.6: Regeneration of head structures in nerve-free tissue piece over the course of 72 h. i. Radius and ii. aspect ratio plots for regeneration of nerve-free tissue piece, with representative images indicated by red lines. Shape symmetry is broken before 48 h and the appearance of tentacle buds is observed around 60 h. Red arrowhead indicates first visible tentacle bud. Scale bar 200 μm.
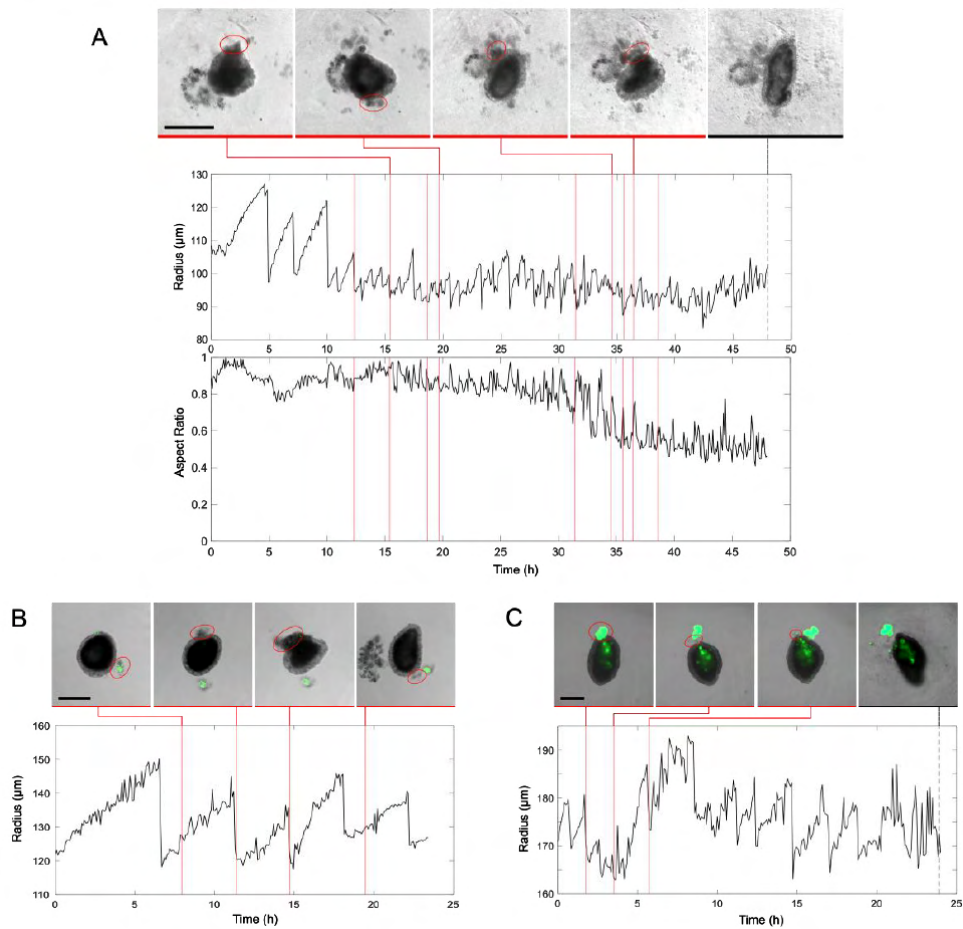
Figure 3.7: Debris is ejected throughout the regeneration process. (A) Cell debris ejected from an un-injected tissue piece. Red lines on radius and aspect ratio plots indicate the earliest frame in which a new piece of ejected debris can be clearly observed. Image series illustrate representative rupture events, with new debris circled in red. Dashed black line and associated image indicate the last frame of the video, showing the presence of a body axis. (B) Tissue piece injected with microbeads 5 h after cutting. 4 trackable rupture events with ejection of both beads and cell debris are observed. Images have been rotated to standardize the orientation of the tissue piece. Oscillations resemble LPOs and rupture site is not conserved. (C) Tissue piece injected with microbeads 24 h after cutting. 3 trackable rupture events with ejection of both beads and cell debris are observed. Images have been rotated to standardize the orientation of the tissue piece. Rupture site is conserved, and oscillations resemble SPOs. The last frame of the video shows the tissue piece is oblong with a conical hypostome structure.
Scale bar: 200 μm.
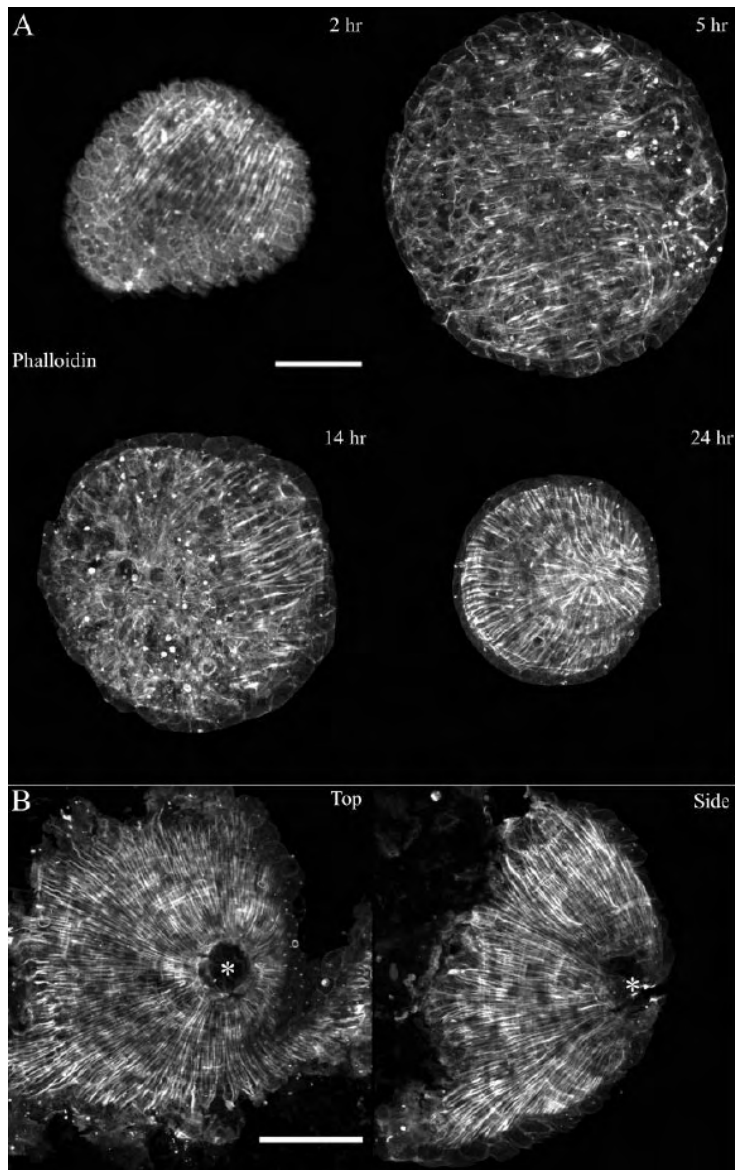
Figure 3.8: Retention of myoneme structure in tissue pieces. ((A) Body column tissue pieces fixed and stained with phalloidin 2, 5, 14 and 24 h after cutting. (B) Phalloidin staining of head pieces 5 h after excision showing retention of normal myoneme organization of the mouth. Damage to the aboral side of the piece (on the left in the side view) occurs during mounting due to the conical shape of head pieces and does not accurately represent the live state. Scale bar: 100 μm.

3.8.2   Supplemental Movies

Movie file link: https://github.com/tapangoel1994/ThesisMovies.git.

Movie 1. Regeneration of wildtype tissue piece. Raw video of the tissue piece represented in Figure 4 A. Scale bar: 200 μm, total time 48 h. Recorded at 1 frame every 5 minutes (0.003 fps), playback at 10 fps.

Movie 2. Regeneration of nerve-free tissue piece. Raw video of the tissue piece represented in Figure 3, showing formation of body axis and head structures. Scale bar: 200 μm, total time 72h. Recorded at 1 frame every 5 minutes (0.003 fps), playback at 10 fps.

Chapter 4

Non-linear elastodynamics of mouth opening in *Hydra*

4.1   Abstract

Epithelial tissues undergo extreme non-linear deformations in a range of developmental and physiological contexts. Often, these deformations have long-range order arising from underlying stochastic, short-range forces in the absence of a master regulator. We have developed *Hydra*'s mouth opening behavior as an experimentally and theoretically tractable *in vivo* model to study non-linear epithelial mechanics in a physiological context. *Hydra* rips open a hole ("mouth") in its head epithelium for ingestion and osmoregulation. The mouth is produced within 1-2 minutes by stochastic contractions generated by actin fibers acting over 2-3 cells. It can get tens of cell diameters wide and has long range order (radial symmetry). We took advantage of the unique regenerative properties of *Hydra*, and chemical and physical manipulations, to show that local mechanical interactions suffice to coordinate mouth opening. We modelled the planar head epithelial tissue as an active viscoelastic anharmonic spring network with nearest neighbor springs coupled to each other via junctions. Using experimental measurements to

constrain our model, we quantitatively reproduced the characteristic time history and spatial symmetry of mouth opening. The model illustrates how strain hardening can lead to bigger and faster tissue deformation if the external forces are concentrated at the boundary of the assembly instead of the bulk. Most importantly, the model shows how symmetry in the deformation is generated simply from mechanical coupling of nearest neighbors despite independent stochastic forces acting on the tissue.

4.2   Introduction

Epithelial tissues maintain important physiological functions by acting as physical barriers, gatekeepers, and signaling centers during development and homeostasis across multicellular organisms [92]. They undergo large deformations - bending, stretching, and compression - on timescales ranging from seconds to days and over length scales many times the size of a single cell [93, 94]. These deformations are often driven by stochastic short range forces that must be coordinated to generate long range patterns.

Since these deformations tend to involve large strains, they are often non-linear. These non-linearities can be due to geometric factors (the large strain amplitude or finite rotation effect means that the quadratic deformation gradient term in the strain tensor cannot be neglected) or biomechanical feedback. These effects play an important role in generating shape and structure during animal development and in various physiological processes. Particularly during embryonic development, non-linear feedback is essential for self-organization and emergence of structure by amplification of instabilities. At the same time, non-linear feedback is also essential to generate stable fixed points in the configuration space of animal structures to ensure robustness of developmental processes against external and internal noise.

Unsurprisingly, the non-linear mechanics of epithelial tissue deformations have long been a subject of great interest and have been studied in both cell culture and in living animals

[95, 96]. However, past efforts suffered from two primary shortcomings: 1) Albeit experimentally and computationally tractable, *in vitro* systems cannot capture the full scope of biomechanical feedback. 2) *In vivo* systems capture the full biological context but are generally too complicated to derive simple conclusions about tissue mechanics beyond the linear mechanical response.

In a previous study, we developed *Hydra* mouth opening as an experimentally and theoretically tractable *in vivo* system to study non-linear epithelial mechanics [83]. *Hydra* is experimentally accessible due to its amazing regenerative capabilities, optical transparency and availability of transgenic lines. This allows for live fluorescence imaging with sub-cellular resolution and various pharmacological and surgical manipulations without adverse effects on the animal. It is also easy to model mathematically due to its simple body plan. These features allow would allow us to study epithelial mechanics in a biologically relevant context. We can ascertain the role of finite strain effects, biomechanical feedback, epithelium-ECM coupling, tissue geometry etc. in generating coordinated tissue scale epithelial deformations.

Hydra can be thought of as a ~1 cm free living intestine, a few hundred microns in diameter. It lives in fresh water and is a cousin of the jellyfish. One end of the tube has and adhesive foot and the other is the head with a ring of tentacles and a dome-shaped hypostome containing the mouth.

The hypostome is primarily composed of three tissue layers: an outer ectoderm, extracellular matrix and an inner endoderm (Figureure 4.1a). The ectoderm and endoderm are monolayers of epithelio-muscular cells interspersed with a few other cell types. These cells have actin processes called myonemes that can generate contractile forces. The myonemes in the ectoderm are arranged into radial spokes while those in the endoderm form concentric circles (Figureure 4.1b). Interspersed within the epithelial layers are two neuronal networks or nerve-nets. Mechanically, the epithelial layers and the extracellular matrix can be thought of as thin, coupled visco-elastic sheets (since they are only 1 cell diameter thick but 20-30 cell diameters in width), the myonemes as active force producing elements and the nerve net as a

regulator of the active forces. The tentacle ring serves as a rigid boundary to the coupled sheets. Therefore understanding the biomechanics of mouth opening would allow us to decipher more general principles about the mechanics of coupled, active epithelial tissues.

In our previous study, we characterized the kinematics of the mouth opening process [83]. *Hydra* opens its mouth in response to food, internal fluid pressure and certain chemicals in its environment. This process involves the rupture of the continuous epithelial layers of the hypostome, contraction of epithelial cells and the formation of an opening, almost as wide as the diameter of the animal (Figureure 4.1c). We showed that this process occurs entirely through radial contraction ($\frac{\Delta l_r}{l_r} \sim 20\%$)and azimuthal elongation ($\frac{\Delta l_\theta}{l_\theta} \sim 200\%$) of cells (Figureure 4.1d-f). However, this process does not involve any cell rearrangements [83]. Further, the mouth area as a function of time follows a characteristic logistic curve, with a timescale $\sim$ 4-5s [83]. Using chemical perturbations, we showed that mouth opening is generated by the contraction of radial myonemes [83].

In this study, we characterize the dynamics of mouth opening. First, we show that the myoneme contractions lead to independent, stochastic, short lived, short-range deformations. However, over the timescale of mouth opening, these stochastic deformations generate a radially symmetric mouth opening. Using loss-of-function experiments, we show that the nerve-net is not necessary to coordinate these short range deformations. Then, using an overdamped anharmonic spring network model, we show that simple mechanical nearest neighbor coupling and anharmonic elasticity can reproduce the experimentally observed kinematics of mouth opening. By scanning through the parameter space of different strength and frequency of active force and, coefficient of non-linear elasticity, we show how anharmonic elasticity leads to a non-trivial response of the passive tissue to active forces on the tissue scale. Finally, we propose further improvements to the model to better mimic the biological reality of the tissue. We also propose new experiments to validate the model and probe the mechanics of the system further.
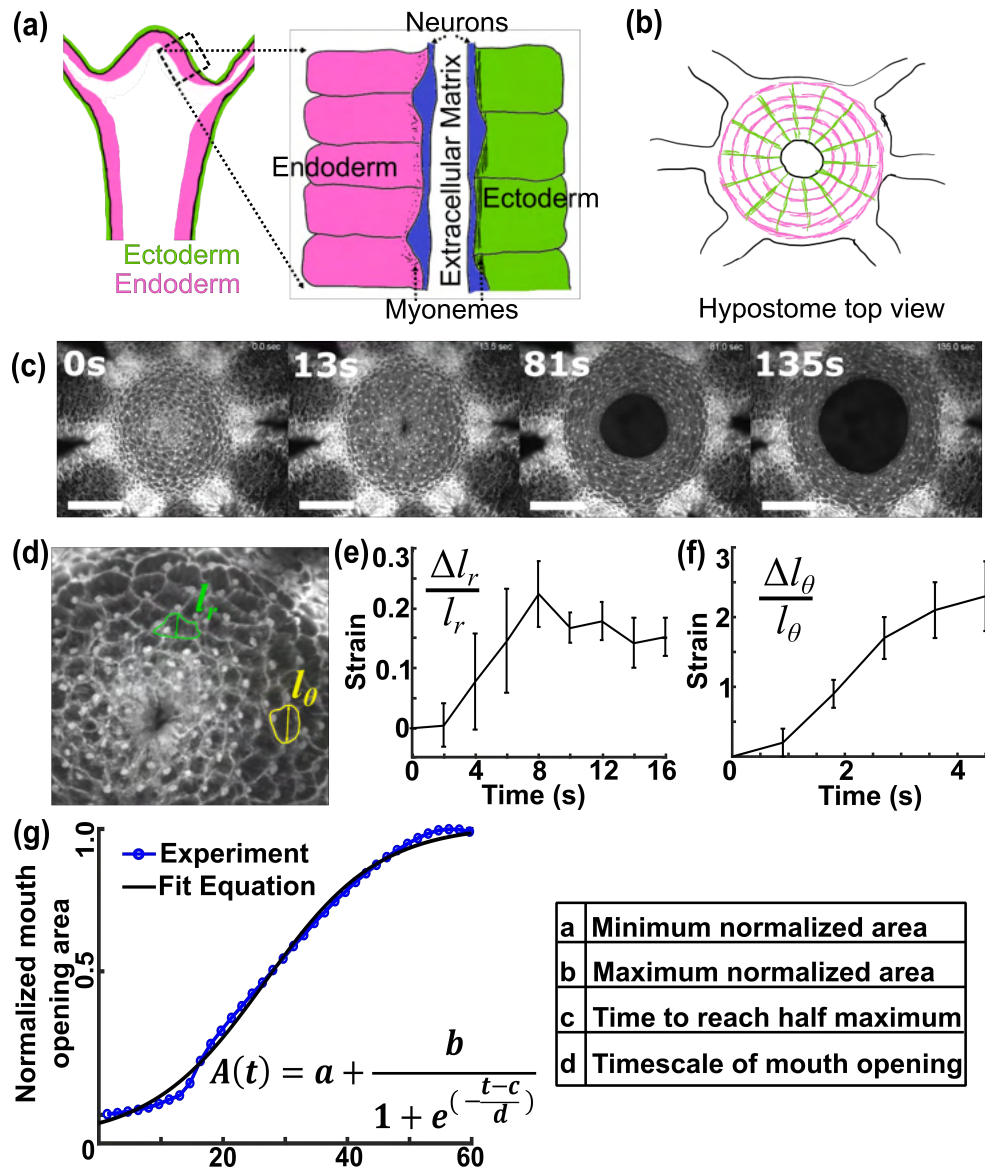
Figure 4.1: Kinematic features of mouth opening (a) Schematic cross section of the hypostome tissue - ectoderm cells in green, endoderm in magenta. Neurons in blue. (b) Schematic of myoneme arrangement in the hypostome when viewed down the axis of the *Hydra*. Ectoderm myonemes form radial spokes (green) and endoderm myonemes form concentric circles (magenta). (c) Example image sequence of mouth opening. Ectoderm cells were imaged using watermelon animals. Scale bar: 200 µm. (d) Representative image of the ectoderm cells imaged using watermelon animals. The yellow and green lines denote the azimuthal and radial lengths of cells respectively. (e-f) Relative change in (e) radial and (f) azimuthal cell length over the course of mouth opening averaged over 5 cells from the same mouth opening event. Error bars represent standard deviation. (g) Representative curve of the normalized mouth opening area as a function of time. The best fit equation was obtained using linear least squares.

95

4.3 Materials and Methods

4.3.1 *Hydra* strains and culture

The *Hydra vulgaris* AEP strain and various transgenic lines derived from this strain: GCaMP6s, expressing the calcium sensor GCaMP6s in interstitial cells [97]; Epithelial GCaMP, expressing GCaMP6s in the ectoderm [98]; Wnt, expressing GFP under control of the Wnt3 promoter [65]; HyBra, expressing GFP under control of the HyBra2 promoter [57]; "Watermelon" (WM) animals [57] expressing GFP in the ectoderm and DsRed2 in the endoderm with both genes under control of an actin gene promoter and, *Hydra vulgaris* strain A10 (chimera consisting of *Hydra vulgaris* (formerly *Hydra magnipapillata* strain 105) epithelial cells and sf-1 interstitial cells, which are temperature sensitive interstitial cells [73] were used for experiments.

Hydra strains were maintained in mass cultures in *Hydra* medium (HM) composed of 1 mM $CaCl_2$ (Spectrum Chemical, New Brunswick, NJ), 0.1 mM $MgCl_2$ (Sigma-Aldrich, St. Louis, MO), 0.03 mM KNO_3 (Fisher Scientific, Waltham, MA), 0.5 mM $NaHCO_3$ (Fisher Scientific), and 0.08 mM $MgSO_4$ (Fisher Scientific) prepared with MilliQ water, with a pH between 7 and 7.3. Cultures were maintained at 18°C in the dark in a Panasonic incubator (Panasonic MIR-554, Tokyo, Japan) The cultures were fed 2-3x/week with *Artemia* nauplii (brine shrimp) from the San Francisco Bay or from the Great Salt Lake (Brine Shrimp Direct, Ogden, UT). Animals were cleaned daily using standard cleaning procedures (Lenhoff and Brown, 1970). Asexual, non-budding polyps starved for at least 24 hours were used for experiments unless stated otherwise.

4.3.2 Generation of nerve-free *Hydra*

To generate nerve-free *Hydra*, A10 polyps were heat-shocked in an incubator (Fisher Scientific 615F) at 28–29°C in the dark for 72 h in an Isotemp oven (Fisher Scientific) and then moved back into the 18°C incubator [73, 76, 77]. All nerve-free animals were subsequently

force-fed and "burped" as described previously [75] for three to four weeks, in which time they lost nematocytes, as well as feeding and mouth opening behaviors. Then animals also adopted a bloated phenotype due to their inability to release built-up fluid inside the body cavity.

4.3.3   Generation of enervated:nerve-free chimera

To generate chimeras with half of the hypostome enervated and the other half nerve-free, nerve-free (nf) A10 and enervated Hybra strains were used. Similarly sized nf A10 and Hybra polyps were selected and put in a dish containing 1.25% methyl cellulose (Acros Organics) and 1 mM linalool (Sigma-Aldrich) in *Hydra* medium to incubate for 10 min. Each polyp was then decapitated one-third of the way down the body column with a scalpel. The resulting head pieces were each prompted to open their mouth with a tap of the forceps, and a lateral cut across the hypostome and tentacles was made with the scalpel to bisect the mouth. The half hypostome pieces were matched with the opposite *Hydra* strain piece and grafted together.

Glass needles were pulled from 5 µL microcapillaries (Corning Inc.) over a Bunsen burner to a thickness of around 0.03 mm. The pieces were then strung onto the needle and a small square of kimwipe (Kimtech) was placed on either side of the grafted pieces to ensure they stay in contact during healing. Chimeras were allowed to heal on the needle for 1.5 h in the methyl cellulose solution and were then removed from the needle with forceps. The chimeras were transferred to a new dish with HM and allowed to heal overnight (between 14 and 24 h) in the 18°C incubator. Chimeras were incubated in a solution of 1:1000 (wt:vol) 1-aminoanthracene (Sigma Aldrich) for 7 min in the dark to provide a temporary green fluorescence, then washed three times with HM. Once stained, chimeras were kept in the dark and imaged as per the method in 4.3.4. The same protocol was followed to prepare control chimeras except for the fact that enervated A10 animals were used in place of the nf A10.

RFamide antibody staining was used to confirm the absence of neurons in the nerve-free tissue of the chimeras after imaging. The chimeras were fixed with 4% paraformaldehyde

made in HM. Chimeras were first relaxed in 1 mM linalool for 5 min, then transferred to the paraformaldehyde solution and fixed for 1 hr at room temperature or overnight at 4℃ in the dark. Samples were then washed once quickly with with PBSTx, followed by two 5 min washes. Chimeras were then washed once in 50% methanol for 10 min, followed by another 10 min wash in 100% methanol, then transferred to fresh methanol for freezing at -20℃. Details of the antibody staining protocol are provided in Supplementary Methods (section 4.8.1)

4.3.4   Image acquisition

Mouth opening was visualized in transgenic animals using epifluorescence microscopy. For imaging studies, 3–7-day starved animals were decapitated immediately below the tentacles with a scalpel, allowed to heal for at least 2 h. The samples were manually positioned in a drop of HM between two glass coverslips separated by a single layer of double-sided tape (Scotch), creating a tunnel slide.

Imaging was performed on an FL Auto 2 microscope (Thermo Fisher Scientific) using the Invitrogen EVOS FL Auto Imaging System software or, on an Olympus IX81 inverted microscope (Olympus Corporation, Tokyo, Japan) with an Zyla 5.5 sCMOS camera (Andor, Oxford Instruments) and Slidebook software version 6.0 (Intelligent Imaging Innovations, Denver, CO). The FL Auto 2 microscope was equipped with a 10×/0.3 Plan Fluor objective and images were recorded at 20-23fps. The Olympus IX81 inverted microscope was equipped with a 20×/0.45 LUCPlanFL N objective and images were recorded at 10fps.

Mouth opening events were either spontaneous (not induced by external stimuli) or chemically induced by flushing in HM containing 0.1 or 0.2mM reduced L-glutathione (Sigma-Aldrich) or 0.5 mM quinine hydrochloride dihydrate (Sigma-Aldrich).

4.3.5 Data analysis

Mouth opening shape and area as functions of time

Custom MATLAB scripts (MATLAB 2021a, Mathworks, Natick, MA) were used to obtain the area of the mouth across several frames, as described in [83]. Briefly, single channel images of the mouth were first binarize. A polygonal region was manually identified as the mouth in the first image of the sequence. Successive images were thresholded based on the pixel intensities in the polygonal region to identify the mouth. For each frame, once the mouth boundary was identified, the area of the mouth, major and minor diameters of the best fit ellipse and, the mean and standard deviation of the mouth radius were calculated.

The areas were then normalized so that they range between 0 and 1. The normalized areas were plotted as a function of time and fit to the logistic equation below using linear least squares fit. $A\left(t\right) = a + \dfrac{b}{1 + e^{-\frac{t-c}{d}}}$

Analyzing mouth openings in enervated:nerve-free chimera

Mouth openings in chimeras were analyzed manually using FIJI [40]. The line tool was used to demarcate the segments of the mouth opening enclosed by the enervated (or nerve-free) half. The polygon tool was then used to enclose each segment of the mouth opening and obtain their areas. The areas of the nerve-free and the enervated segments of the mouth were individually normalized to their respective maximum areas, so the areas lay between 0 and 1. The normalized areas of the enervated and nerve-free halves were plotted against time and individually fit to the logistic equation in section 4.3.5 to obtain the timescales of mouth opening (the 'd' parameter). The ratio of the d parameters for the A10 and Hybra halves was calculated for each chimera.

4.3.6 Toy model of the *Hydra* mouth

To identify the minimal elements necessary to produce a coordinated mouth opening response, a simple mass-spring model was constructed. The underlying assumptions and model details are described below.

Model assumptions

- The epithelial layer and the ECM are coupled such that the mechanics of the three layers can effectively be described by those of a single visco-elastic layer. This simplifying assumption is based on the experimental observation that both epithelial layers show the same logistic kinematics for the opening area with fit parameters that are not too different from each other [83]. Experimental results show that the endoderm start opening only after the ectoderm has opened to a critical area [83]. However, we are only interested in the dynamics of the tissue after initial rupture. Further, since no active forces are being produced in the ECM or in the endoderm, the passive mechanical response of these layers can be effectively captured by modifying the elastic modulus and viscosity of a single layer.

- Tissue deformation occurs in-plane. While we do not have direct experimental evidence to concretely show that mouth opening is a 2-D phenomenon, the tunnel slide imaging setup largely prevents out-of-plane deformations.

- Mouth opening is a low Reynolds number process ($Re = \frac{\rho v l}{\eta} \approx 10^{-10}$). Therefore, we neglect the inertial term in the momentum balance equations.

- We assume that the myonemes co-move with the tissue and that at timescales > 100 ms, the forces generated by the radial myonemes can be treated as uncorrelated. The former assumption relies on the fact that the myonemes are actin projects arising from epithelial

cells. The latter is based on our observation that individual radial tugs observed during mouth opening are uncorrelated over a timescale of 100 ms.

Model description

The epithelial tissue of the hypostome is modelled as a system of $R+1$ concentric regular N-gons, all lying in the same plane. Each vertex (node) is connected to its topological nearest neighbors (so each node is connected to 4 others, except the ones on the innermost N-gon) by an anharmonic spring (Figureure 4.5a). All vertices, except those in the $R+1$-th N-gon are movable. The $R+1$-th N-gon represents a fixed boundary, mimicking the role of the tentacle ring in the hypostome For each node, we can write the momentum balance equation:

$$
\begin{aligned}
\frac{\vec{r}_{i,j}}{\mu} = & -\left\{ \kappa \left(\|\vec{r}_{i,j} - \vec{r}_{i-1,j}\| - a \right) + \frac{\kappa}{l_0^2} \left(\|\vec{r}_{i,j} - \vec{r}_{i-1,j}\| - a \right)^3 \right\} \frac{\vec{r}_{i,j} - \vec{r}_{i-1,j}}{\|\vec{r}_{i,j} - \vec{r}_{i-1,j}\|} \\
& -\left\{ \kappa \left(\|\vec{r}_{i,j} - \vec{r}_{i+1,j}\| - a \right) + \frac{\kappa}{l_0^2} \left(\|\vec{r}_{i,j} - \vec{r}_{i+1,j}\| - a \right)^3 \right\} \frac{\vec{r}_{i,j} - \vec{r}_{i+1,j}}{\|\vec{r}_{i,j} - \vec{r}_{i+1,j}\|} \\
& -\left\{ \kappa \left(\|\vec{r}_{i,j} - \vec{r}_{i,j-1}\| - b_i \right) + \frac{\kappa}{l_0^2} \left(\|\vec{r}_{i,j} - \vec{r}_{i,j-1}\| - b_i \right)^3 \right\} \frac{\vec{r}_{i,j-1} - \vec{r}_{i,j-1}}{\|\vec{r}_{i,j} - \vec{r}_{i,j-1}\|} \\
& -\left\{ \kappa \left(\|\vec{r}_{i,j} - \vec{r}_{i,j+1}\| - b_i \right) + \frac{\kappa}{l_0^2} \left(\|\vec{r}_{i,j} - \vec{r}_{i,j+1}\| - b_i \right)^3 \right\} \frac{\vec{r}_{i,j} - \vec{r}_{i,j+1}}{\|\vec{r}_{i,j} - \vec{r}_{i,j+1}\|} \\
& + \delta_{i,R} \tilde{f}_0 \sum_n \frac{1}{\sqrt{2\pi\sigma^2}} e^{-\frac{(t-t_n)^2}{2\sigma^2}} \frac{\vec{r}_{i+1,j} - \vec{r}_{i,j}}{\|\vec{r}_{i+1,j} - \vec{r}_{i,j}\|}
\end{aligned}
\tag{4.1a}
$$

$$
t_n \sim Poiss(\lambda) \tag{4.1b}
$$

where, $\vec{r}_{i,j}(t)$ is the position of the vertex in the i-th N-gon at the j-th azimuthal position at time t. a is the rest length of the radial springs. b_i is the rest length of the azimuthal springs in the i-th N-gon.

κ is the spring constant, μ is the coefficient of mobility and l_0 is the length at which the harmonic and anharmonic forces are of equal magnitude.

$\delta_{i,R}$ is the Kronecker delta function, $\tilde{f}_0$ is the strength of the active force, σ is the duration over which the force acts and t_n is the time at which the force acts. t_n are drawn randomly from a Poisson distribution with a mean rate λ.

Values of all these parameters are provided in Table 4.1.

Numerical methods

The model equations were solved using custom MATLAB 2021a (MathWorks, Natick, MA, USA) scripts. For each set of free parameters, 5 realizations of the stochastic external force were simulated. The system of coupled ODEs described in equation 4.1a were then solved for each realization using a 4th order Runge-Kutta scheme. For each realization, the final area of the mouth and, azimuthal average and standard deviation of mouth radius were obtained. The timescale of mouth opening were obtained by fitting the mouth area from the simulations to the experimentally obtained logistic curve. These parameters were then averaged over the five realizations for each set of parameters. The relevant code is available at GITHUB

4.4 Results and Discussion

4.4.1 Mouth opening involves radial asymmetry on short timescales

Previous work has shown that the forces necessary to deform the epithelial tissue and cause the mouth to open are generated by the radial myonemes associated with the ectodermal cells [83]. While these myonemes form a long range radial pattern, individual myonemes are short [99]. This short length scale of the myonemes and by extension, that of the forces they generate, manifests itself as short radial 'tugs' at the boundary of the mouth as it opens (Figure 4.2a). We found that these tugs involve the contraction of 3-4 adjacent cells (Figure 4.2b). Further, binning the movies into 100 ms intervals and quantifying the relative angle between successive tugging events, we find that the probability density of the angles is not significantly different

from a uniform distribution (Figure 4.2c). This shows that the tugs are azimuthally uncorrelated over timescales of 100ms. We tracked the ratio of standard deviation of the mouth radius to the mouth radius, averaged over the azimuth. This ratio is essentially a measure of the asymmetry of the mouth shape. We find that it to about 5% over the course of mouth opening (Figure 4.2d).

These observations suggest that the radial forces produced by the myonemes are short ranged, act over short timescales and are azimuthally uncorrelated. However, we see that mouth opening is symmetric over longer timescales and involves a very large deformation of the epithelial tissues. Therefore, we would expect some regulatory element to coordinate these forces.
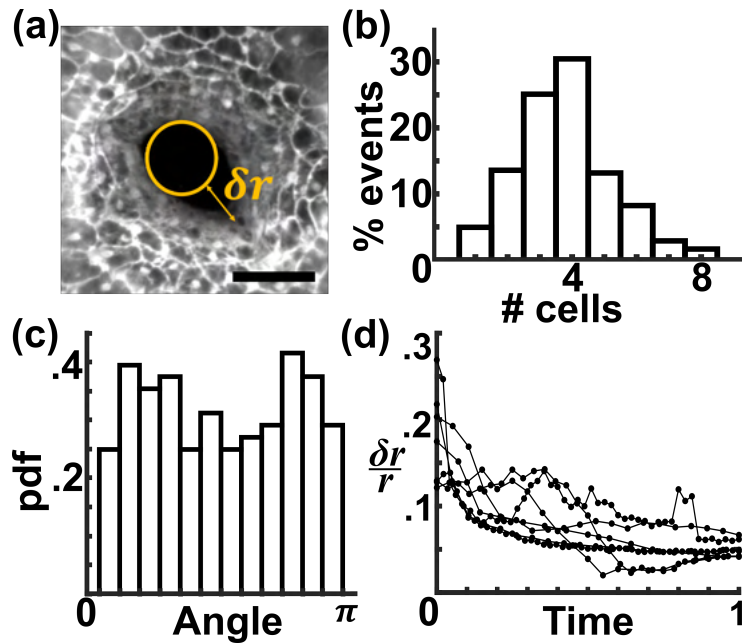
Figure 4.2: Mouth opening involves radial asymmetry on short timescales (a) Representative image of a radial tug during mouth opening. Scale bar: 200 μm. (b) Histogram of number of cells involved in each tugging event (n = 364 tugging events from N = 8 independent mouth opening events) (c) Probability density function for the relative angle between successive tugging events (n = 184 tugging event pairs from N = 5 independent mouth opening events). (d) Time evolution of the ratio of the standard deviation of the mouth radius averaged over the azimuth, to the mean mouth radius (n=6 mouth opening events). Time is normalized from the beginning of mouth opening to when the mouth reaches its maximum area.

4.4.2 The nerve-net is not necessary to coordinate mouth opening

In this search for a regulatory element, the first natural candidate is the nerve net. We used loss-of-function experiments to deduce its role in coordinating mouth opening. We generated nerve-free animals as described in section 4.3.2. It has previously been shown that these animals are unable to open their mouths in response to food or reduced glutathione, suggesting that sensory neurons are necessary to help trigger mouth opening. By stimulating the hypostomes of nerve-free animals with electrodes, we were also able to verify that if an electrical signal is provided, the mouth does start opening, further providing evidence of the role of the nerve net in helping trigger mouth opening. However, these experiments do not explain the role of the nerve net in coordinating mouth opening after it has been triggered.

To understand the role of the nerve net in coordinating mouth opening, post trigger, we created chimeras where half the hypostome tissue had a nerve net while the other half did not (see section 4.3.3, Figure 4.9). We could then induce mouth opening in these chimera by exposing them to reduced glutathione and image the process. We observed that the enervated half of the tissue deformed first but after a delay, the nerve-free part of the tissue started deforming, albiet much slower than the enervated half (Figureure 4.3(a-c)). To verify that this difference in opening rates was a result of the absence of the nerve net and not differences in tissue properties of the A10 and Hybra, we repeated the experiments with chimeras containing enervated A10 and Hybra. We found that the ratio of the timescale of mouth opening $\frac{d_{nerve-free}}{d_{enervated}}$ is significantly lower (p-value = 0.0263, Student's t-test) for the enervated:nerve-free chimeras (ratio = 0.64 $\pm$ 0.29 (mean $\pm$ standard deviation), n = 9 movies, N = 9 chimeras) compared to the enervated:enervated chimeras (ratio = 1.70 $\pm$ 1.26, n = 8 movies, N = 6 chimeras)(Figureure 4.2).

These results show that while the nerve-net is necessary to trigger mouth opening and affects its rate, mouth opening can be coordinated even in the absence of the nerve-net. We suspect that the nerve-free half is able to deform due to the mechanical force on it generated by the deformation of the enervated tissue.

4.4.3 Contractile activity is most prominent in the tentacle ring

Further, to study the activation pattern of the ectodermal cells, we used fluorescent microscopy to visualize calcium activity in the ectoderm with a transgenic strain expressing GCaMP6s in the ectoderm cells. Contrary to a previous report [98], we did not observe a azimuthally symmetric signal travelling from the tip of the hypostome to the tentacle ring. Instead, we observed stochastic flashes in the entire tentacle ring region and weaker, local signals elsewhere in the hypostome (Figure 4.4).

In the absence of a significant role of the nerve-net in coordinating the mouth opening and, ectoderm activation being localized primarily to the tentacle ring region, we now investigate the role of the nearest neighbor coupling of cells to explain the observed kinematic features of mouth opening.

4.4.4 The anharmonic spring network model captures all essential features of size, time history and symmetry of mouth opening

To investigate the role of mechanical nearest neighbor coupling of cells, we use a bottom-up computational approach. We ask - "What are the minimal mechanical ingredients necessary to produce the large symmetric mouth opening that we see experimentally ?". Specifically, (a) how is the characteristic initial slow area increase in the time curve of mouth opening generated, (b) how does non-linear elasticity due to the finite strain ($\frac{\Delta l_r}{l_r}$ 0.1, Fig 4.1e,f) modulate the length scale and timescale of mouth opening in response to the active forces and, (c) how is a symmetric opening generated from stochastic active forces. To answer these questions developed the model described in section 4.3.6 and Fig 4.5a.

From equation 4.1a, we see that the kinematics of mouth opening primarily depend on two ratios: $\frac{\tilde{f_0}}{\kappa l_0}$ and $\frac{\lambda}{\frac{\kappa}{\mu}}$. The first is the ratio of the strength of the active force and the characteristic elastic force of the anharmonic springs. The second is the ratio of the rate of active forcing

to the visco-elastic relaxation rate. Using previously published experimental measurements, we estimate κ and μ. We vary λ, $\tilde{f}_0$ and l_0, which correspond to the active forcing rate, active force strength and the strength of the anharmonic elastic term (through $\frac{\kappa}{l_0^2}$ in equation 4.1a) respectively.

We find that this simple model reproduces the characteristic logistic time curve for the mouth area that we observe in experiments (Figure 4.5b). As the strength of the active force and the forcing rate increase, the model shows an increase in the final area of the mouth (Figure 4.5c - top panel). This result is intuitive since increasing the total amount of work done by the active forces on the tissue (either through increasing the magnitude of the force or its frequency) should result in increased amount of elastic energy being stored in the spring network and therefore, a larger mouth opening. It is also worth noting that the magnitude of the mouth area obtained for larger values of the active force ($> 10^4$ nN) are the same order of magnitude as that obtained in experiments [83].

Interestingly,we find that timescale of mouth opening is not sensitive to the forcing strength and forcing rate (Figure 4.5c - middle panel). The timescale obtained here is also the same order of magnitude observed in experiments [83]. Further we note that response of the opening time to the force and forcing rate changes with the strength of non-linearity (i.e. with l_0).

We also find that the model is able to reproduce the level of symmetry observed in the experiments - $\frac{\delta r}{r}$ is on the order of 5% for most of the parameter space explored. The same value is observed in experiments (Figure 4.5c - bottom panel). We do note a linear region in the phase space characterized by increasing magnitude of active force and decreasing forcing rate, where the mouth is more asymmetric than observed in experiments. This observation is a result of two competing forces: (a) a larger magnitude active force will produce a larger deformation and therefore more asymmetry but (b) if this force is experienced independently at multiple vertices, each vertex will undergo the same large deformation and therefore, the asymmetry

will not increase. The limiting case of this would be if the contractile forces was acting on all the vertices simultaneously, even if the forces had a large magnitude, they would still produce a symmetric mouth opening.

4.4.5 Strain stiffening effect enhances mouth area and affects opening time in a non-trivial fashion

In the model described by equation 4.1a, the finite strain effect is accounted for by the anharmonic elasticity term. For simplicity, we chose the lowest order non-linear term possible - a cubic. Since the sign of this term is the same as the linear elastic term, it represents a strain stiffening effect: as the spring deforms more, it becomes stiffer. By changing l_0, we are able to change the strength of this effect - increasing l_0 makes strain stiffening effect weaker and vice-versa. By changing the strength of the anharmonic elastic term, we investigated the role of strain stiffening in modulating the tissue response to active forces.

Specifically, we found that stronger non-linearity led to wider mouth opening. As l_0 decreases, for a given force strength and forcing rate, we get a larger mouth area (Figure 4.5c - top panel). At first this result was surprising: naively, one would expect that since the non-linearity makes the springs stiffer, if the stiffening effect is stronger, we would get smaller tissue deformations for the same force and therefore, smaller mouth openings. However, in this scenario, since the force must be transmitted from the outer ring inwards, stronger strain stiffening means that for small deformations of the springs in the outer ring, larger forces can be transmitted to the center.

Further, we noted that as the strength of the non-linearity increased, the response of the opening time to the strength and rate of active force changed. In the weakly non-linear case ($l_0 = \infty$), this timescale increased with the strength and the rate of the active forcing. In the strong non-linear regime ($l_0 = 1$), the timescale decreased as the strength and rate of the active force increased. For intermediate values of the non-linear coefficient ($l_0 = 3$) the timescale of

mouth opening became insensitive to the active force. We currently do not have a plausible explanation for why this might be happening.

4.4.6   A cascade provides the slow initial increase in mouth area observed in experiments

We found that the slow initial increase of the mouth area is generated because of a cascade effect (Figure 4.6): The active forces acting on the outermost $(R)^{th}$ ring of springs pull on the outermost vertices first. This in turn causes the springs in the $(R-1)^{th}$ ring to elongate and therefore pull on the $(R-2)^{th}$ ring of springs. This force is transmitted from the outermost ring to the innermost ring with a time delay as the springs contract in a sequence. This is seen in the time shift between the peak deformation of the springs in the outermost ring and those in the innermost ring.

4.4.7   Stiffness of the azimuthal springs controls the symmetry of mouth opening

We also found that the symmetry of the mouth opening can be attributed to the nearest-neighbor coupling of the vertices via springs. Increasing the stiffness of the azimuthal springs, keeping all else constant, caused $\frac{\delta r}{r}$ - the measure of asymmetry of the mouth radius - to reduce (Figure 4.7). This result can be understood by considering the total restoring force acting on a single vertex displaced from its equilibrium position. Consider the network in its equilibrium state. Let an outward radial force act on one of the vertices and displace it radially. Then the total restoring force on the vertex would be the sum of the forces generated by the radial springs it is connected to plus the radial component of the restoring force exerted by the azimuthal springs it is connected to. As the azimuthal springs become stiffer, the total restoring force acting on the vertex would increase causing its total displacement to decrease. Further, as the azimuthal

springs become stiffer, they will also transmit larger forces to the neighboring vertices, causing them to displace more as well. Both these factors combined would lead to a more symmetric mouth opening as azimuthal springs become stiffer.

4.4.8   Model reproduces enervated:nerve-free chimera experiments

To further validate the model, we simulated the enervated:nerve-free chimera experiment. This involved allowing the active forces to act on only one half of the nodes in the outermost polygon, creating a "Semi-circular" sector of the network which was completely passive (Figure 4.8a,b).

We note that the model qualitatively recapitulates experimental observations: the nerve free half of the "tissue" opens slower than the enervated half (Figure 4.8c,d). Comparing the opening times of the two halves, same as what we did in the experiments, we find that ratio of the timescales obtained from the simulations in the strongly non-linear regime is the same order of magnitude as seen in the experiments (Figure 4.8f).

This result lends further support to the validity of our simple model in capturing the essential dynamics of mouth opening in *Hydra*. Further, they also shows transmission of mechanical forces via mechanical nearest-neighbor interactions is sufficient to produce the mouth opening response we observed in the chimeras.
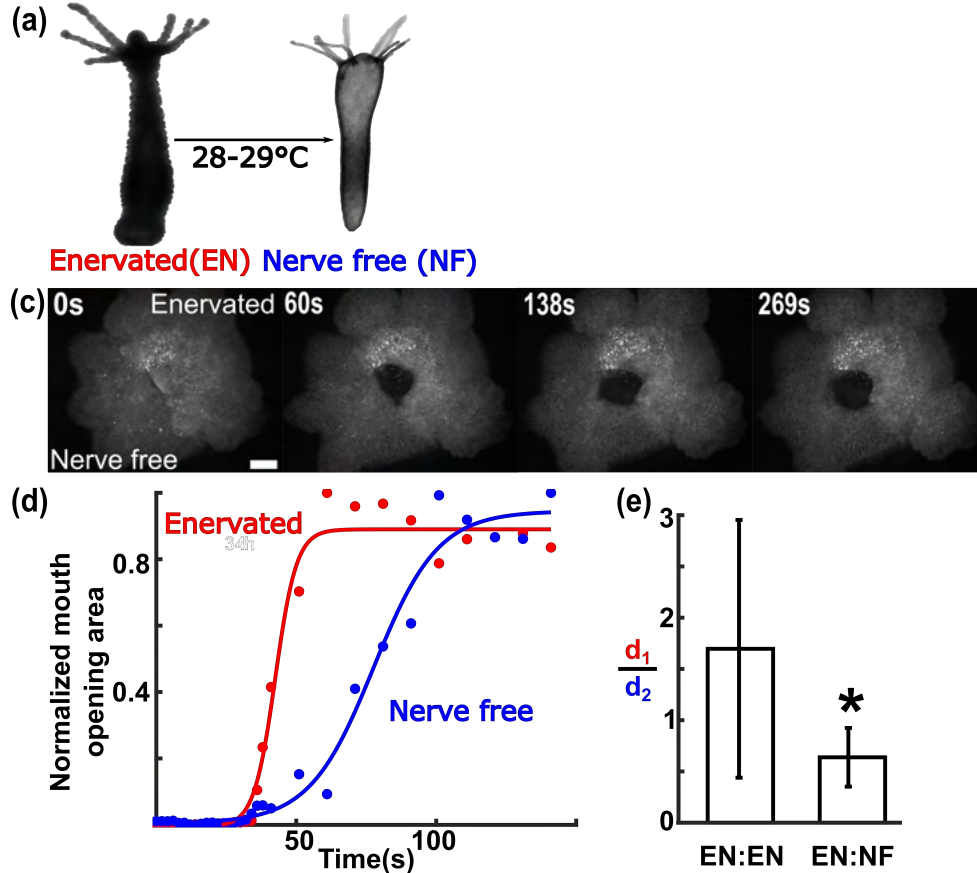
Figure 4.3: Nerve-net is not necessary to coordinate mouth opening (a) Representative images of enervated and nerve free *Hydra*. Nerve free *Hydra* have a bloated appearance due to buildup of fluid in the body cavity due to their inability to open their mouth to vent fluid. (b) Schematic of the chimera making process. (c) Representative image sequence of mouth opening in enervated:nerve-free chimera. Scale bar: 100 μm (d) Representative mouth area vs time curves for the enervated and nerve free segments of the mouth. (e) Ratio of timescale of opening for the two tissue halves for enervated:nerve-free chimeras (ratio = 0.64 ± 0.29 (mean ± standard deviation), n = 9 movies, N = 9 chimeras) and enervated:enervated chimeras (ratio = 1.70 ± 1.26, n = 8 movies, N = 6 chimeras). * denotes p-value < 0.05 (Student's t-test)
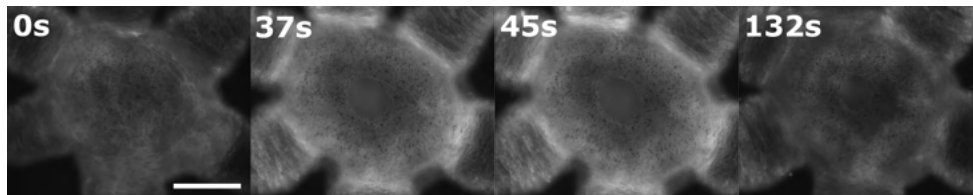
Figure 4.4: Contractile activity is most prominent near the tentacle ring Representative image sequence of contractile activity in the ectoderm from live fluorescence imaging of *Hydra* strain expressing GCaMP6s in the ectodermal cells. Scale bar: 200 μm.
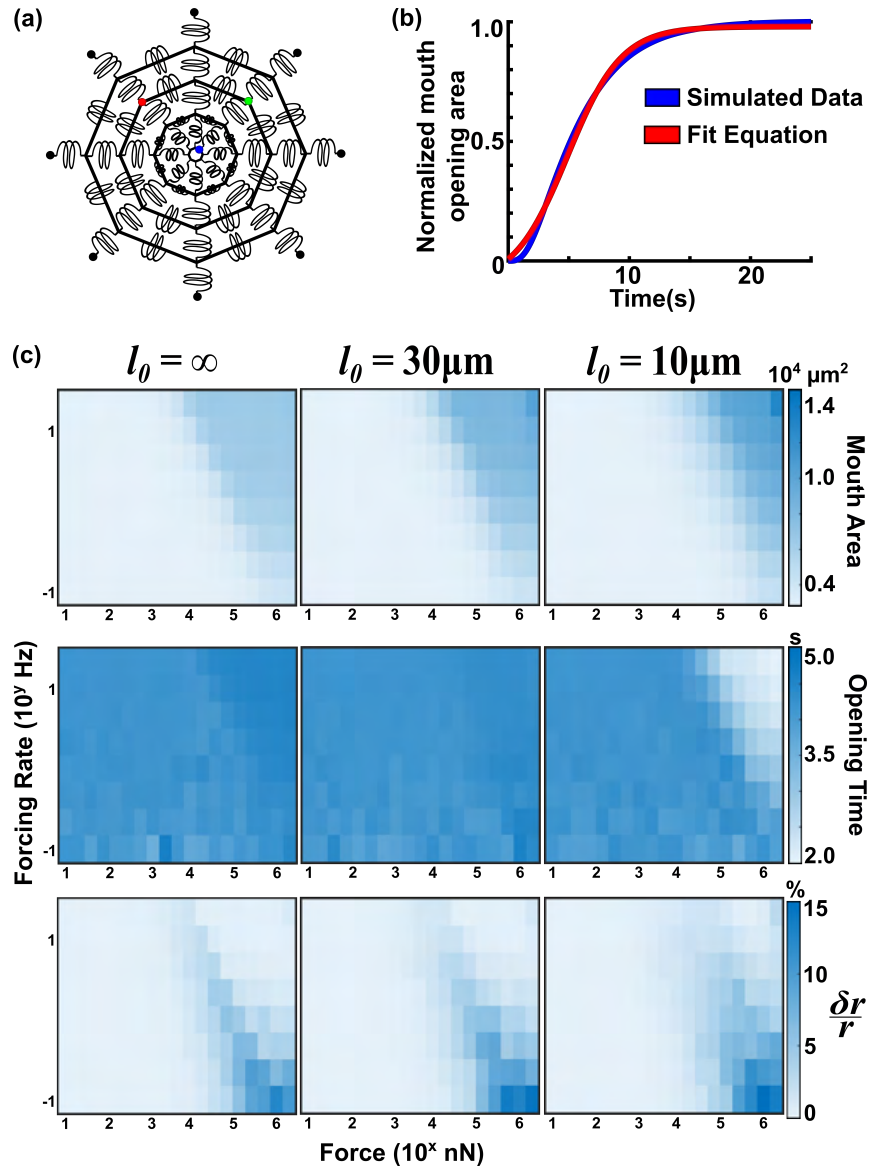
Figure 4.5: Anharmonic spring model of the mouth (a) Schematic of the toy model for the mouth. The innermost octagon represents the mouth. All vertices, except for those represented by solid circles move according to the equation 4.1a. (b) Representative curve of the normalized mouth opening area as a function of time, as obtained from the simulations (blue). Note the slow initial increase and eventual saturation obtained, similar to experimental results. (c) Heatmaps of mouth opening area (Top), opening timescale (Middle) and symmetry (Bottom) as functions of the strength of the active force on the x-axis (log-scale) and the rate of active forcing on the y-axis (log-scale). Decreasing l_0 corresponds to increasing strength of the coefficient of non-linear elasticity.
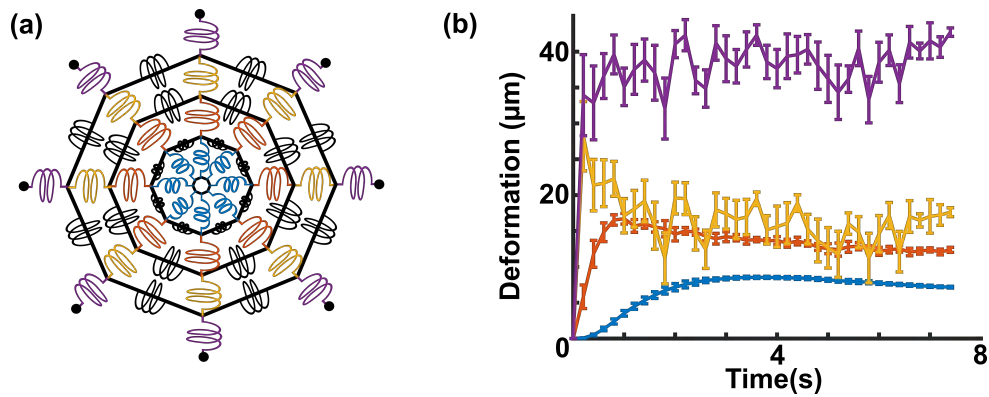
Figure 4.6: Mouth opening proceeds through a cascade of contractions (a) Schematic of the toy model for the mouth. (b) Length change of radial springs, averaged over the azimuth. Error bars represent standard deviation. Colors correspond to the colors of the radial springs in (a).
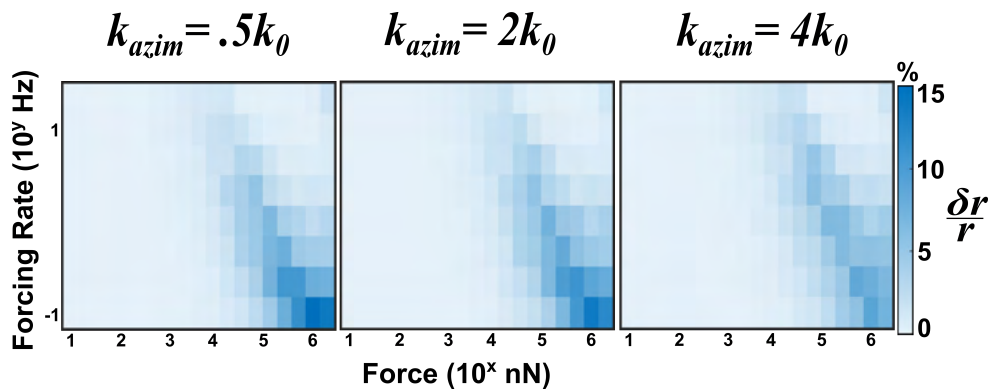
Figure 4.7: Azimuthal springs control symmetry of mouth opening Keeping all else constant, increasing the stiffness of azimuthal springs (κ_{azim})reduces the ratio $\frac{\delta r}{r}$, making mouth opening more symmetric. Heat maps show ensemble average of $\frac{\delta r}{r}$ for (force strength, forcing rate) pairs for $l_0 = 30\mu m$. $\kappa_0 = 100nN\,\mu m^{-1}$ is the stiffness of the radial springs (Table 4.1).
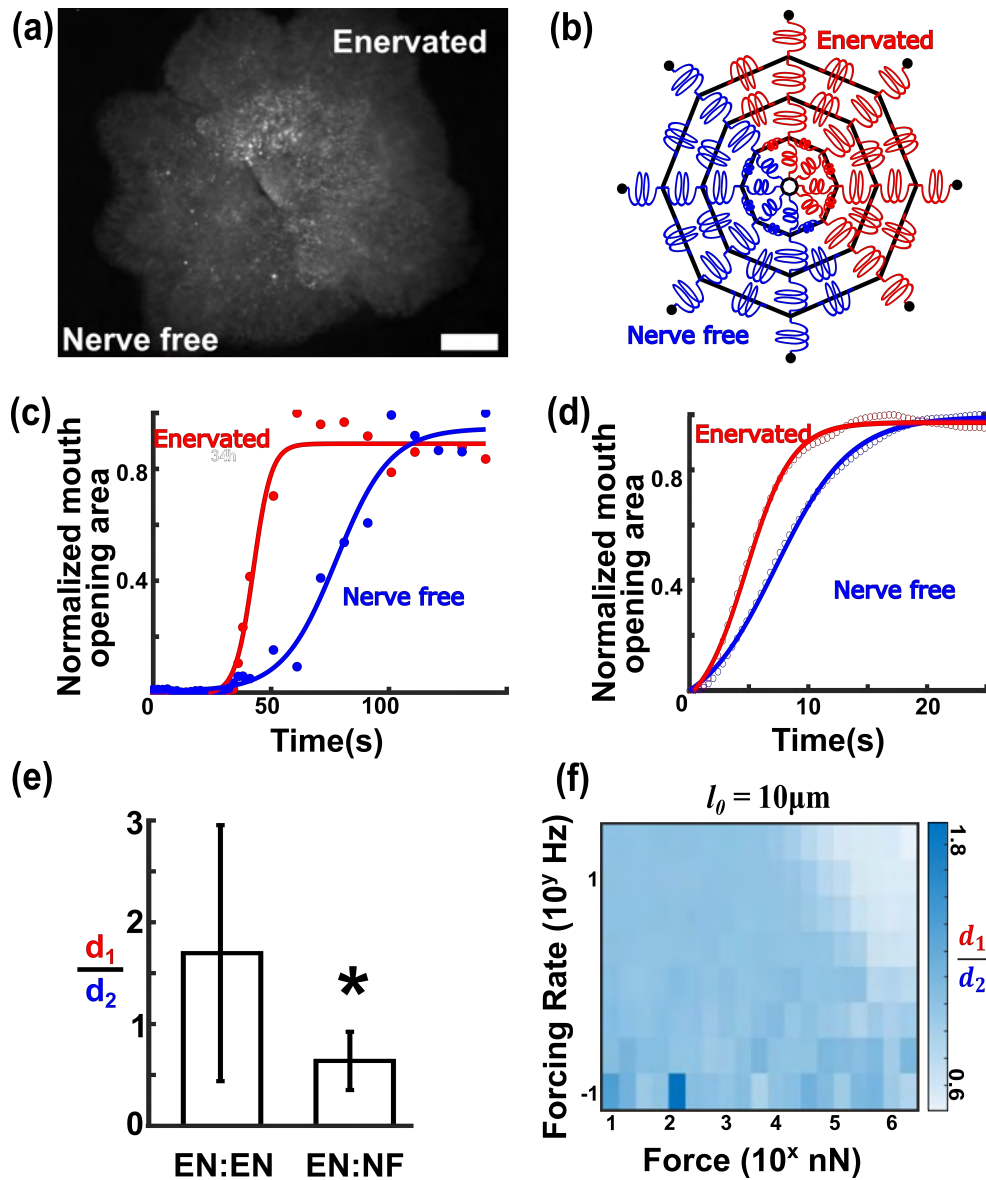
Figure 4.8: Model reproduces enervated:nerve-free chimera experiment Representative image of (a) experimental and (b) simulated chimera at time t = 0s. Representative mouth area vs time plots from (c) experiments and (d) simulations. Note that while the timescales are different, the nerve-free half opens slower than the enervated half. $\frac{d_1}{d_2}$ ratio from (e) experiments and (f) simulations. The ratio obtained from simulations for $l_0 = 10\mu m$ for large values of force and forcing rate are the same order of magnitude as the values obtained from experiments.

4.5 Conclusion

Previous work explored the unusual kinematic features of mouth opening in *Hydra* and established it as an experimentally and computationally tractable model to study extreme deformations of epithelial tissue due to active forces. In this study, we were able to exploit these features to gain insight into the dynamics of the mouth opening process and epithelial mechanics more generally. We were able to obtain the spatial and temporal features of the active myoneme forces that generate mouth opening. We showed that there forces are short range and uncorrelated azimuthally over short timescales. In spite of this, mouth opening is symmetric on longer timescales. Using loss-of-function experiments, we were able to show that while the nervous system is necessary to trigger mouth opening, it is not necessary to coordinate the mouth opening process. Further, using fluorescence imaging, we showed that contractile activity is primarily limited to the region around the tentacle ring. Based on these observations, we hypothesized that mouth opening is coordinated purely by mechanical coupling of nearest neighbor cells. To test this hypothesis, we developed a simple computation model consisting of a 2-D network of anharmonic springs (to mimic the composite of the tissue layers) subject to stochastic, independent, external forces (mimicking the forces generated by the myonemes). We showed that, constrained by experimentally obtained parameter values, this model is able to reproduce experimental observations of the mouth area, opening time and mouth symmetry up to an order of magnitude. The model also gave us insight into the dynamics of mouth opening. It shows how elastic nearest neighbor coupling is sufficient to coordinate mouth opening and produce a symmetric deformation. It also shows the non-intuitive role of strain stiffening in generating larger global deformation and modulating the timescale of mouth opening. Overall, the study shows how simple mechanical interaction between cells can generate large, coordinated deformations from short range stochastic forces in biological systems.

4.6   Future work

Our experimental results and computational predictions for mouth area, opening time and mouth symmetry match up to an order of magnitude. However, since we are trying solve the "inverse" problem of deducing microscopic mechanisms based on macroscopic observations, we must recognize there presence of other possible mechanisms that can generate the results we observe. It is therefore important to constrain the model better using independent experimental measurements of the input parameters and validate it further against experimental results from different types of perturbations.

While we've demonstrated that the nerve net is not necessary to coordinate mouth opening, we do find the enervated tissue deforms faster (Figure 4.3). This is possibly due to activation of myonemes by a neuronal signal. To investigate this further, it would be useful to image mouth opening using animals of the neuronal GCaMP6s strain [97] and use image processing to obtain spatial and temporal patterns of neuronal signal propagation. This would also allow for better modelling of the propagation of active forces in the model.

It would also be useful to probe the role of the tentacle ring as a fixed boundary in generating a symmetric mouth opening. Surgically removing a part of the tentacle ring to create an asymmetric boundary would be one way to study how tissue geometry and boundary conditions affect the shape of the large scale deformation. Preliminary results from experiments where a segment of the tentacle ring is surgically removed show that it makes the mouth asymmetric. Alternatively, one could also apply external forces at the boundary of the tissue to study the same problem. We are currently doing this experiment by aspirating diametrically opposite tentacles into a glass capillary by applying negative hydrostatic pressure. This generates a uniaxial tension on the tissue boundary. We then image mouth opening in these samples and analyze how the external tension affects the shape of the mouth. Both of these perturbations can also be modelled computationally by changing the equations of motion for the outermost fixed vertices in the model.

We also note that the computational model leaves out several details of the actual biological system, the most prominent of which is the presence of two epithelial layers. A simple extension of the model would be to incorporate a second planar spring network to model the endoderm separately from the ectoderm. The coupling between the two networks would depend on the mechanical properties of the extracellular matrix. This would also allow us to test the model against other experimental observations that a) the ectoderm needs to open to a critical area before the endoderm starts opening and b) the endoderm opens with a time delay relative to the ectoderm.

A more subtle modification involves incorporating the fact that as we go away from the center of the network, each spring accounts for more and more tissue area. Therefore, the stiffness of the springs and the coefficient of mobility of the vertices should depend on their radial distance from the center. Preliminary simulations show that this modification does not affect the qualitative relationships presented in the results but does affect the quantitative values of the mouth area, opening time and symmetry.

4.7   Acknowledgments

4.8   Supplemental Material

4.8.1   Supplemental Methods

Immunohistochemistry

The fixed chimera samples were placed on glass slides for a wet mount antibody stain. Humid chambers for staining were constructed by lining covered 100 mm Petri dishes (Spectrum Scientific) with wet paper towels and placing the slides inside the dishes. A well was created in the center of each glass slide by layering two pieces of double-sided tape across both short sides of the slide with one piece of tape running on both long edges of the slide. The samples were placed in a drop of hydra medium on the slide. All steps were performed at room temperature unless otherwise noted. The samples were washed three times with 20 µL 1x PBS, followed by a 15 min permeabilization with 20 µL 0.5% PBSTx (0.5% Triton-X in 1x PBS). They were then incubated for 3.5 h in 20 µL blocking solution (10% FBS, 1% DMSO in 1x PBS) and placed overnight (16 h) at 4℃ in 30 µL anti-rfamide primary antibody (gift from Dr. Kathleen Siwicki) diluted 1:200 in the blocking solution. On the second day, samples were washed quickly 3x with 40 µL 1x PBS, followed by four 25–35 minute washes of 20 µL 0.3% PBSTx. The samples were then incubated in a 1:1000 or 1:500 dilution of Alexa 488 antirabbit IgG secondary antibody (Thermo-Fisher Scientific) for 5 h, followed by three quick and two 10 min washes of 0.3% PBSTx. The samples were then washed three times with 1x PBS. The 1x PBS was replaced with a 1:1 solution of glycerol and HM. Finally, a cover slip was placed over the samples and nail polish was used to seal the slides. Z-stacks of the samples were imaged using a Leica high-resonance scanning SP5 confocal microscope with a 20x C-Apochromat 1.2 W objective.

4.8.2 Supplemental Figures
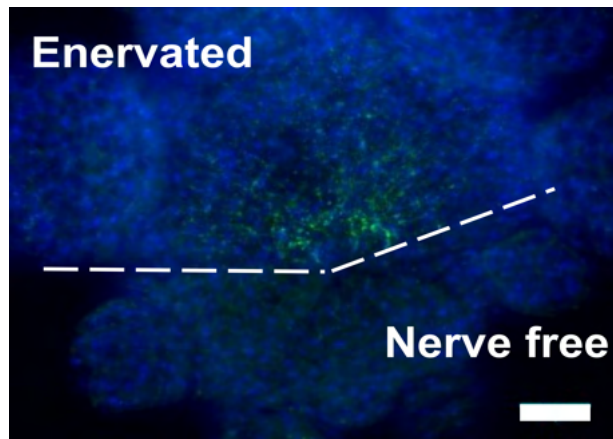
Figure 4.9: Verifying absence of nerve net in the enervated:nerve-free chimera Representative image of fixed chimeric hypostome stained with anti-rfamide (neurons, green) and DAPI (nuclei, blue) after imaging mouth opening. Note that neurons are present only in the enervated half of the hypostome.

4.8.3 Supplemental Tables

Table 4.1: Model Parameters

Parameter	Description	Value	Source
a_0	Initial mouth radius (one cell radius)	10 μm	This study
R_0	Hypostome radius	200 μm	[83]
a	Radial distance between successive polygons	47.5 μm	$\frac{R_0 - a_0}{R}$
E	Ectoderm Youngs modulus	$\sim$5000 Pa	[83]
h	Ectoderm cell diameter	$\sim$20 μm	[100]
τ_{relax}	Ectoderm visco-elastic relaxation time	10 s	[83]
κ	Spring constant	100 nN μm^{-1}	$E \times h$
μ	Coefficient of mobility	0.001 μm nN^{-1} s	$(E \times h \times \tau_{relax})^{-1}$
σ	Duration of individual active forces (half of the average duration of neuronal action potentials used as proxy)	0.05 s	[97]
l_0	Cross-over length scale (length at which harmonic and anharmonic force are equal)	$\{10, 20, 30, 40, \infty\}$ μm	This study
f_0	Active force strength	10×2^n nN, $n = 1, 2...20$	This study
λ	Mean arrival rate of active force	20×2^{-p}, $p = 1, 2...7$	This study
R	Number of polygons with movable vertices	4	N\A
N	Number of vertices in each polygon	8	N\A
dt	Time step size in simulations	0.02s	N\A
T	Total simulation time	25s	N\A

Chapter 5

Conclusions and Future Directions

In this dissertation, we used two different animal models and three different biological processes to investigate the kinematics, dynamics and biological consequences of chemo-mechanical coupling. In chapter 2, we provided the first quantitative, comparative study of the kinematics of planarian fission across species. We found fundamental physical limits to how planarians self-bisect and allocate biomass to their offspring based on mechanical and anatomical constraints. This allowed us to develop a predictive model for biomass allocation between planarian offspring. We also showed how heterospecific differences in the kinematics of self-bisection explain the differences in reproductive strategies of different planarian species. Our results add to the growing body of work that has largely been looking at biological factors that influence planarian reproductive behavior. In chapter 3, we showed how the development of physiological function affects the mechanical behavior of tissues. Within the context of regeneration and development in *Hydra*, we showed that a core assumption of existing models of axis formation is inaccurate. Our work showed that apart from passive tissue mechanics and morphogen patterning, models of embryonic development also need to consider how development of physiological functions affects the mechanics of morphogenesis. In chapter 4, we elucidated the dynamics of *Hydra*'s mouth opening behavior. This work builds on a previous

study of the kinematics of mouth opening [83]. We showed how mechanical nearest neighbor interactions can coordinate tissue deformations generated by local stochastic forces even in the absence of a master regulator. We also developed a new experimental tool - linalool - that makes *Hydra* surgeries and imaging easier. This is a valuable addition to the toolkit of the *Hydra* research community. Our simple model of the mouth provides an intuitive framework to understand tissue mechanics in *Hydra* and should be contrasted to complicated continuum models proposed before [22]. Our model also serves as a great starting point to investigate several interesting aspects of extreme epithelial deformation. While these studies answered some questions related to biomechanics in *Hydra* and planarians, they also open the doors to new ones.

Our study of the kinematics of planarian self-bisection serves as a launchpad to investigate the spatio-temporal changes in mechanical forces involved in this process. For instance, determining how adhesion forces are distributed along the body of the planarian at different time points during the division process would allow us to better understand the inter-specific kinematic differences in planarian self bisection. Knowing the strength of the adhesive forces would also help obtain better bounds for the location of the self-bisection plane. Such data has previously been obtained for one of the planarian species using traction force microscopy [32]. A similar experiment could be done using the other planarian species used in our study. Another aspect of the division process worth investigating in greater detail is the role of muscle contractions and mass transport in creating the zone of waist constriction around the site of self-bisection. Two experiments might shed light on this question: (1) 3D imaging to see how planarian change their local height to accommodate the waist constriction and, (2) using functionalized fluorescent beads that adhere to the planarian surface to see how mass is displaced locally to form the waist. At the population level, a model that predicts the time of self bisection

would be a great addition to our work on predicting the location of the division plane. Previous work [13] has linked planarian size and likelihood of self-bisection. Combining this information with our model for biomass allocation, it should be possible to create a model that accurately predicts when an individual planarian would divide.

Our study of the shape oscillation pattern in regenerating *Hydra* tissue pieces shows the need to develop new measurements to test theoretical models of symmetry breaking. *In vivo* live imaging of chemical patterning could provide one such measurement. Doing so would require the development of new transgenic strains where endogenous Wnt3 expression can be visualized.

In chapter 4, we showed enervated tissue deforms faster than nerve free tissue. To explore the role of the nerve net further, our model can be modified to include waves of neuronal signal that can trigger the active forces, as opposed to just having independent stochastic forces. To estimate the speed of these waves, we need to ascertain the production rate and speed of the Ca^{2+} signal traveling through the ectoderm tissue. This would require imaging mouth opening in animals that express GCaMP6s in the ectoderm and have fluorescent markers embedded in the tissue. Together, these two sets of data - the changing intensity of the GCaMP6s signal and the displacement field of the markers - would allow us to obtain the speed and production rate of the Ca^{2+} signal. This information would shed light on the role of mechano-chemical coupling in coordinating mouth opening.

Understanding the role of tissue geometry in generating the mouth opening response would also be an important area of exploration. Experimentally, this can be done by excising parts of tissue from the tentacle ring or by applying negative pressure along parts of the tissue boundary, using microaspiration. Computationally, this can be implemented by removing some of the fixed springs at the boundary or by subjecting some of the fixed boundary springs to a constant force. These perturbations would allow us to understand how tissue geometry affects tissue deformation.

Another interesting project would be to look at the implications of the coupling between the epithelial layers in generating mouth opening. It has been observed that the endoderm starts opening later than the ectoderm, and only after the ectoderm has opened to a critical area [83]. This coupling is hard to dissect experimentally, since neither tissue layer can be isolated while maintaining the geometric structure of the mouth. A computational approach is more likely to make headway. Our model can easily be extended from a 1 layer spring network to 2 layers of spring networks, connected to each other via springs and dashpots to mimic the mechanics of the extracellular matrix between the two epithelial layers. Such a two layer model would allow us to understand how coupling between tissue layers affects their response to active forces.

To summarize, we used non-traditional model organisms - planarians and *Hydra* - to study how mechano-chemically coupled systems behave at the tissue and organismal level. The remarkable regenerative capabilities, simple body plan and aquatic habitat of these animals allowed us to use a range of experimental, observational and computational techniques in our work. Through our studies, we were able to generate valuable insights, system specific and more general.

Appendix A

Linalool acts as a fast and reversible anesthetic in *Hydra*

A.1 Abstract

The ability to make transgenic *Hydra* lines has allowed for quantitative *in vivo studies* of *Hydra* regeneration and physiology. These studies commonly include excision, grafting and transplantation experiments along with high-resolution imaging of live animals, which can be challenging due to the animal's response to touch and light stimuli. While various anesthetics have been used in *Hydra* studies, they tend to be toxic over the course of a few hours or their long-term effects on animal health are unknown. Here, we show that the monoterpenoid alcohol linalool is a useful anesthetic for *Hydra*. Linalool is easy to use, non-toxic, fast acting, and reversible. It has no detectable long-term effects on cell viability or cell proliferation. We demonstrate that the same animal can be immobilized in linalool multiple times at intervals of several hours for repeated imaging over 2–3 days. This uniquely allows for *in vivo* imaging of dynamic processes such as head regeneration. We directly compare linalool to currently used anesthetics and show its superior performance. Linalool will be a useful tool for tissue

manipulation and imaging in *Hydra* research in both research and teaching contexts.

A.2   Introduction

Abraham Trembley's careful and systematic studies on *Hydra* regeneration, published in his Memoires in 1744, brought this freshwater cnidarian into the spotlight of biological research [101]. Hydra is an optically transparent polyp a few millimeters in length. It consists of a hollow cylindrical body column with a head on one end, consisting of a ring of tentacles and a dome-shaped hypostome, and an adhesive basal disk on the other end. *Hydra* is composed of only a small number of cell types originating from three (ectodermal, endodermal and interstitial) stem cell lineages [90]. This anatomical simplicity, continuous cell turnover in the adult [102], and the ability to regenerate from small fragments of the body column or even from aggregates of cells [59, 103] render *Hydra* a powerful system for studies of development [104], stem cell biology [105, 106], and regeneration [107–110]. Furthermore, *Hydra* has a relatively simple nervous system [86, 111], consisting of a few thousand cells [112] that are organized in three neuronal networks [97], making it an attractive system to study neuron development [113, 114] and neuronal control of behavior [97, 115]

Exploiting *Hydra's* patterning processes and regenerative abilities via sophisticated excision and grafting studies has been a mainstay of *Hydra* research since Trembley's original experiments. This "cut-and-paste" approach has provided fundamental insights into *Hydra* biology. For example, the excision and subsequent threading of body column rings onto fishing line allowed researchers to probe questions about oral-aboral polarization [116]. Grafting of hypostomes into body columns showed that the tip of the hypostome acts as a head organizer [117, 118] long before the head organizer was biochemically analyzed [119]. Transplantation experiments were used to characterize the properties and dynamics of head inhibition [120] and estimate the length scales of head activation and inhibition [121], which helped validate

the Gierer-Meinhardt model of axial patterning [21] decades before *in vivo* visualization of cells or proteins was possible in *Hydra*.

However, despite its many advantages, *Hydra* has not become a mainstream model organism due to the lack of genetic tools. This has changed in the last decade with access to a fully assembled *Hydra* genome [55], single cell RNAseq data [122], and the development of molecular tools that allow for the generation of transgenic lines [56, 57, 123]. Because of these tools, numerous recent studies have been able to address longstanding open questions that could not previously be answered. For example, the recent creation of a transgenic line expressing GCaMP6s in the interstitial lineage allowed visualization of neural activity in real time in freely behaving animals and led to the discovery of multiple discrete networks of neurons linked to specific behaviors [97]. Transgenic animals have also enabled biomechanics studies to settle key biological questions regarding the mechanism driving cell sorting during regeneration from cell aggregates [109] and the functioning of the *Hydra* mouth [83].

As *Hydra* research continues to dig deeper into such questions in the living animal, future studies will require ever more precise and repeatable manipulations, high resolution live imaging, or a combination thereof to fully exploit transgenic strains and other new technologies. Because *Hydra* is in a continuous dynamic state of extension-contraction and responds rapidly to stimuli such as touch and light [124], a reversible way of slowing or preventing the animal's movements would greatly facilitate these kinds of experiments. The search for a reliable and reversible relaxant in *Hydra* has driven the field to explore an array of compounds, with the most prominent being urethane [63, 125–128], heptanol [129, 130], and chloretone [58, 131–133]. Urethane and heptanol have broad effects on *Hydra*. Urethane reverses the transepithelial potential, causing adverse effects upon several hours of exposure [125]. Heptanol blocks epithelial gap junction communication in the body column [134]. Chloretone is reportedly nervous-system specific, but *Hydra* was observed to develop tolerance to the anesthetic within hours of exposure [133]. Thus, existing anesthetics have limitations and there is an urgent need for an alternative that

reliably immobilizes *Hydra* without causing tolerance or adverse health effects.

Here, we report on linalool as a novel, safe and fully reversible anesthetic for Hydra. Linalool is a monoterpenoid alcohol found in flowers and frequently used in cosmetic products [135]. It has been shown to have anesthetic or sedative activity in mice [136], catfish [137] and flatworms [138]. Linalool exists in two enantiomeric forms with different pharmacological effects. In humans, the (S)-enantiomer causes an increase in heart rate while the (R)-enantiomer works as a stress relieving agent [139]. In contrast, in catfish the (S)- enantiomer acts as a sedative [137]. Here, we demonstrate that a racemic mixture of linalool enables live imaging of *Hydra*, including the acquisition of fluorescence time-lapse movies and multichannel z-stacks at high magnification. Linalool is fast acting – a 1 mM solution of linalool anesthetizes an animal within 10 min of exposure, with recovery occurring in approximately the same time after removal from the solution. Because anesthesia using linalool is reversible, the same animal can be imaged consecutively over the course of days, enabling dynamic studies of long-term processes such as head regeneration and budding. Furthermore, linalool facilitates the rapid execution of precise tissue manipulations such as tissue excisions and grafting. Linalool has been reported to be a cytostatic agent in cancer cells in vitro [140]; therefore, we also investigated this possibility in *Hydra*. We found no significant effects of prolonged (3-day) continuous linalool exposure on budding rates, mitotic activity, or cell viability. In contrast, 3-day continuous exposure to linalool partially suppressed regeneration in amputated animals, but regeneration could be rescued by removal of the anesthetic. Thus, linalool may also be a useful tool for manipulating regeneration dynamics. In conclusion, we find that linalool outperforms other currently used anesthetics and enables *in vivo* manipulations and live imaging of *Hydra* with precision and ease of use.

A.3   Materials and Methods

A.3.1   *Hydra* strains and culture

We used the *Hydra vulgaris* AEP strain [141, 142] and various transgenic lines derived from this strain: GCaMP6s, expressing the calcium sensor GCaMP6s in interstitial cells [97]; Epithelial GCaMP, expressing GCaMP6s in the endoderm cells [98], Wnt, expressing GFP under control of the Wnt3 promoter [65]; HyBra, expressing GFP under control of the HyBra2 promoter [57]; "Watermelon" (WM) animals [57] expressing GFP in the ectoderm and DsRed2 in the endoderm with both genes under control of an actin gene promoter; *Hydra vulgaris* strain A10 (chimera consisting of *Hydra vulgaris* (formerly *Hydra magnipapillata* strain 105) epithelial cells and sf-1 interstitial cells, which are temperature sensitive interstitial cells [73]; and a line originating from a single animal that was obtained by recombining AEP ectoderm and watermelon endoderm following tissue separation [109] and named "Frank" by the undergraduate student who created it. The Frank line has unlabeled ectoderm and DsRed2-expressing endoderm. *Hydra viridissima* and *Hydra oligactis* were generously provided by Dr. Rob Steele.

Hydra strains were maintained in mass cultures in *Hydra medium* (HM) composed of 1 mM $CaCl_2$ (Spectrum Chemical, New Brunswick, NJ), 0.1 mM $MgCl_2$ (Sigma-Aldrich, St. Louis, MO), 0.03 mM KNO_3 (Fisher Scientific, Waltham, MA), 0.5 mM $NaHCO_3$ (Fisher Scientific), and 0.08 mM $MgSO_4$ (Fisher Scientific) prepared with MilliQ water, with a pH between 7 and 7.3. Cultures were maintained at 18℃ in the dark in a Panasonic incubator (Panasonic MIR-554, Tokyo, Japan) save the *H. oligactis* and *H. viridissima* which were kept on a windowsill at room temperature. The cultures were fed 2-3x/week with *Artemia* nauplii (brine shrimp) from the San Francisco Bay or from the Great Salt Lake (Brine Shrimp Direct, Ogden, UT). Animals were cleaned daily using standard cleaning procedures [74]. Asexual, non-budding polyps starved for at least 24 h were used for experiments unless stated otherwise.

A.3.2 Generation of nerve-free *Hydra*

To generate nerve-free *Hydra*, A10 polyps were heat-shocked in an incubator (Fisher Scientific 615F) at 28–29°C in the dark for 72 h and then moved back into the 18°C incubator [73, 76, 77]. All nerve-free animals were subsequently force-fed and "burped" as described previously [75] for three to four weeks, in which time they lost nematocytes, as well as feeding and mouth opening behaviors.

A.3.3 Preparation of anesthetic solutions

Stock solutions were made in HM at concentrations of 1 mM linalool (Sigma-Aldrich), 0.04% heptanol (Acros Organics, Fisher Scientific), 2% urethane (Sigma-Aldrich), or 0.1% chloretone hemihydrate (Sigma-Aldrich). Linalool and heptanol were prepared fresh daily by adding to HM and shaking vigorously for 1 min to dissolve and, stored at room temperature. Urethane and chloretone solutions were stored at 4°C for a few days and pre-warmed to room temperature before usage. Anesthetic solutions were prepared at room temperature, except for chloretone, which was prepared with slight heating.

A.3.4 Linalool viability assay

24 h starved polyps were incubated in 6-well plates (Genesee Scientific, El Cajon, CA), 8 or 10 animals per well in 2 mL of different concentrations of linalool (0–10 mM) at room temperature for 3 h. Below concentrations of 3 mM and above 3.6 mM, 4 technical replicates were performed for each concentration. Between 3 mM and 3.6 mM, 6 technical replicates were performed at each concentration. The fraction of live animals was scored at the end of the assay. To obtain the LC50 value, the fraction of dead animals (1- fraction of live animals) was plotted

against the linalool concentration. The data were fitted to the Hill equation as in [143]:

$$y = \frac{1}{1 + \frac{LC_{50}}{x}^{Hill-coefficient}}$$

Here, y is the fraction of dead animals and x is the concentration of linalool in millimolar. The fit was generated using the curve fitting application in MATLAB (MathWorks, Natick, MA, USA) to obtain the mean LC50 value and the 95% confidence intervals.

A.3.5 Characterizing short term efficacy of anesthetics

1–5 intact *Hydra* polyps were incubated per well in a flat bottom 6-well plate (Eppendorf, Hamburg, Germany) filled with 8 mL of HM or respective anesthesia. If more than 2 polyps were used, 40 µm or 100 µm Falcon cell strainers (Fisher Scientific) were used in the well to allow for quicker transfer of the animals from HM to anesthesia and vice versa. In some experiments, all wells were imaged simultaneously, and polyps were stained with neutral red (1:400,000 w/v; Fisher Scientific) in HM for 90 s at room temperature prior to the experiment to enhance contrast during imaging. The 6-well plate was imaged from the top using a Basler A601f-2 camera (Basler Inc., Exton, PA) attached to a 25 mm TV lens C22525KP with adjustable focal length (Pentax, Tokyo, Japan) for 65 min at 1 fps using Basler pylon camera software. Lighting was provided by a model A4S light box (ME456, Amazon, Seattle, WA). After 65 min, the cell strainers were moved to a new well and 8 mL of HM were added to each well. Following this, the plate was imaged for 2 h. In other experiments, individual wells were imaged on a stereo microscope using a Flea-3 camera (FLIR Integrated Imaging Solutions Inc, Wilsonville, OR) controlled by a custom MATLAB script. To obtain representative images at higher magnification, anesthetized *Hydra* were imaged in a 35 mm tissue culture dish with a Leica MZ16FA microscope (Leica Microsystems Inc., Buffalo Grove, IL) equipped with a SPOT RT3 camera (SPOT Imaging, Sterling Heights, Michigan), using the SPOT 5.1 software (SPOT Imaging) at 15 min and at 60

min exposure.

A range of sublethal linalool concentrations (0 mM, 0.1 mM, 0.25 mM, 0.5 mM, 0.75 mM,1 mM) were tested. Working concentrations for other anesthetics were 2% urethane, 0.04% heptanol, or 0.1% chloretone, with induction imaged for at least 20 min and recovery for at least 30 min. At least 10 animals were assayed for each condition, in at least 3 technical replicates. Time of induction of anesthesia was considered to be the time at which the animal stopped extending further after its last spontaneous contraction, and time of recovery was considered to be the timing of complete contraction in the first contraction burst observed after returning the polyps to HM. Due to the complex behavior of *Hydra* and the subjectivity of these measures, calculated times for induction and recovery should be considered estimates rather than conclusive values.

A.3.6 Body column length of *Hydra* in anesthetics

24 h starved polyps were imaged for 10 min in HM to observe both extended and contracted states of the moving polyp to calculate an average body length ((max+min)/2). The polyps were then transferred to 1 mM linalool, 2% urethane, 0.04% heptanol, or 0.1% chloretone and imaged for an additional 20 min. We averaged the minimum and maximum body lengths of *Hydra* in the last 10 min of recording in each anesthetic. Average body length in the anesthetic was divided by the average in HM to find the % body length for each anesthetic to determine whether the polyps were hyperextended (¿100%) or contracted (¡100%) compared to their "normal" length. Because *Hydra* doesn't have a fixed body shape or length due to constant extension and contraction, this normal length is somewhat arbitrary; it nevertheless allows us to compare the effects of the various anesthetics.

A.3.7 Feeding and pinch responses in linalool

24 h starved polyps were incubated in 1 mM linalool for 10 min in a 60 mm tissue culture dish (VWR International, Radnor, PA). Each animal was pinched using a pair of Dumont No. 5

forceps (Fine Surgical Tools, Foster City, CA) to determine presence or absence of a contractile response while in the linalool solution.

To evaluate how quickly the pinch response would be restored after removal from 1mM linalool, six 1-day starved *Hydra* were incubated in 1mM linalool for either 10 min or 30 min in a 30 mm diameter dish. After incubation they were moved over to the lid of a 30 mm dish containing 3 mL *Hydra* medium with a glass pipet and their behavior was recorded on a Leica Wild M3C dissection microscope, equipped with a Flea-3 camera. Three independent replicates were performed for each 10 min and 30 min exposure, with 6 biological replicates per technical replicate.

To assay whether animals exhibited a feeding response in linalool, 4-day starved polyps were first incubated for 10 min in HM or 1 mM linalool. Meanwhile, 30 *Artemia* were counted and added to a well of a 96-well plate (Eppendorf) either in HM or 1mM linalool. A picture of the well was taken using a Flea-3 camera attached to a stereo microscope to record the number of *Artemia* in the well. A single polyp was then added to the well and left undisturbed for 30 min. At the end of 30 min, the number of *Artemia* ingested were counted, either by pulling the ingested *Artemia* out of the animal's body cavity using forceps in the case of the *H. viridissima* or by counting the number of freely floating *Artemia* in the dish.

To assay how long anesthetized animals took to regain a feeding response once removed from linalool, 5 animals were incubated in 1mM linalool for 10-15 min. A single individual was added to a small drop (60–80 µL) of HM containing approx. 70–80 *Artemia*. All 5 animals were imaged using a Leica dissection microscope and Flea-3 camera at regular intervals to determine whether the *Hydra* started eating *Artemia*. The number of animals eating at 5, 10, and 15 min were recorded. Eating was determined as having an enlarged body column due to ingestion of *Artemia*. Three technical replicates with 5 animals each were performed.

A.3.8 Cross sections and "zebra grafts"

48–72 h starved Wnt and Frank polyps were used to assay sectioning. Polyps were placed in the lids of 35 mm dishes in either HM or 1 mM linalool for at least 10 min. Rings of tissue were excised from the body column using a scalpel 10 blade. The rings were strung onto glass needles pulled from microcapillaries (World Precision Instruments, Sarasota, FL) using a P-1000 micropipette puller (Sutter Instrument, Novato, CA) and imaged with a Leica MZ16FA microscope equipped with a SPOT RT3 camera, using the SPOT 5.1 software. The time taken to cut the sections was measured for each polyp. The thickness of each section was measured using Fiji [40] by measuring the length of the thickest part of the cross section.

"Zebra grafts" (n = 10 per condition) were created using WM and Frank animals. One animal of each kind was used to make one graft. The animals were placed in a 100 mm petri dish (Spectrum Scientifics, Philadelphia, PA) filled with either HM or 1 mM linalool in HM. A small piece of filter paper (2x2 mm) was cut and threaded onto a size 00 enameled insect pin (Austerlitz, Carolina Biological) and the pin placed into the dish. One animal was decapitated, and the head threaded onto the pin mouth first using forceps such that the cut edge of the tissue faced towards the point of the pin. The second animal was then decapitated, and the head discarded. A ring of tissue was cut as thinly as possible from the body column of the second animal and threaded onto the pin, followed by a ring from the first animal. Alternating rings of tissue were cut and placed on the pin until the body columns of both animals were used up, at which point one of the feet was threaded onto the pin to complete the chimera. A second piece of filter paper was threaded onto the pin, and forceps used to gently move the two pieces of paper together in order to force all the rings into contact with each other. These chimeras were allowed to heal on the pins for 2 h, then gently pushed off the pins with forceps, transferred to clean 35 mm dishes full of HM, and allowed to further heal overnight before imaging. Two grafts were then imaged using an Invitrogen EVOS FL Auto microscope (Thermo Fisher Scientific) and the Invitrogen EVOS FL Auto Imaging System software. Since the entire

graft did not fit in a single field of view, multiple images were taken and stitched together in Inkscape 0.92.3 which is an opensource vector graphics editor. The other grafts were imaged using an Olympus IX81 inverted microscope (Olympus Corporation, Tokyo, Japan) with an ORCA-ER camera (Hamamatsu Photonics, Hamamatsu, Japan) and slidebook software version 5.0 (Intelligent Imaging Innovations, Denver, CO). The number of segments in each graft and the time taken to cut sections of the parent animals and assemble the graft on the pin was recorded.

Grafting of heads into the body column was accomplished using WM and unlabeled animals using an approach similar to the insect pin method described above. The WM animal was decapitated, and a slit cut in the side of the unlabeled animal. The pin was passed through the WM head hypostome first, then through the wound in the unlabeled polyp and out through the body wall on the other side. Care was taken when positioning the filter paper pieces to avoid pushing the donor head into the recipient body cavity. Animals were allowed to heal for 2 h, then removed from the pins and placed in dishes of clean HM to heal overnight before imaging. Grafting of head organizers into the body column was accomplished without pins. Head organizers were obtained by anesthetizing a WM animal in linalool, removing the head, then excising the tentacle bases to leave only a small fragment of tissue containing the tip of the hypostome. A small slit was cut in the body column of an unlabeled animal, and forceps used to place the hypostome piece into the slit. Animals were allowed to heal for 2 h before transfer to dishes of clean HM. Successful grafts were imaged every 24 h to determine whether an ectopic body axis was induced.

A.3.9   Fluorescence imaging in 1 mM linalool and in other anesthetics

All fluorescence imaging was done using the Olympus IX81 inverted microscope with the ORCA-ER camera. Slidebook software was used to interface with the microscope and acquire z-stacks and time-lapse images. Anesthesia incubations were performed as described earlier.

Hydra expressing GCaMP6s in nerve cells and WM *Hydra* were used for fluorescence

imaging. For low magnification single channel imaging, a GCaMP6s animal was allowed to move freely in a drop of either HM or 1 mM linalool on a 40 mm x 24 mm glass coverslip (Fisher Scientific) and was imaged in the GFP channel with a 50 ms exposure using a 4x objective (Olympus). Images were recorded every 100 ms for 10 s to obtain a time lapse movie. Rigid body correction of z-stacks was accomplished using a previously described algorithm [144]. For high-magnification single channel imaging, GCaMP6s animals were mounted in tunnel slides prepared as described in [83]. Neurons in the body column of GCaMP6s animals were imaged by taking z-stacks of the tissue in the GFP channel (500 ms exposure; z-step size of 0.25 μm), using a 60x oil immersion objective (Olympus).

For imaging calcium activity during mouth opening, 4–5 day starved epithelial GCaMP animals were incubated in 1 mM linalool for 10 min. The animals were then decapitated and the hypostomes mounted in tunnel slides. Mouth opening was induced by flushing in 2 mM reduced glutathione (Sigma-Aldrich) diluted in 1 mM linalool into the tunnel slide [83]. Images were taken every 400 ms with an 80 ms exposure using a 10x objective (Olympus) in the GFP channel.

For calcium imaging using a pinch response, 5 epithelial GCaMP animals were used. A single polyp was moved into a 60 mm petri dish with HM. Response to pinch was recorded on the Leica MZ16FA microscope equipped with the SPOT RT3 camera at 5 fps. The same polyp was then moved into a second 60 mm petri dish containing 1 mM linalool and incubated at room temperature for 10 min. Pinch response was then recorded in the same way it was done for HM.

For low-magnification multi-channel imaging, WM animals were incubated in Hoechst 33342 (Thermo-Fisher Scientific) diluted 1:500 in 1 mM linalool for 15 min in the dark. The animals were then decapitated and the hypostome mounted in a tunnel slide. Z-stacks were taken in DAPI, GFP and RFP channels with a step size of 2.99 μm using a 10x objective.

For high-magnification multi-channel imaging, RWM animals were first incubated in SYTO 60 red fluorescent nucleic acid stain (Invitrogen) diluted to 10 μM in HM for 1 h at

room temperature in the dark. 2 quick washes in 1 mL HM followed, as well as a 15 min incubation in the dark at room temperature in 1:250 Hoechst 33342 diluted in 1 mM linalool. Body columns of the animals were imaged in the DAPI, RFP and DRAQ5 channels with a 60x oil immersion objective. For high magnification two-channel imaging, Hoechst 33342 (Thermo-Fisher Scientific) was diluted 1:500 in 1 mL of the respective anesthetic solution and WM animals were incubated for 15 min at room temperature in the dark. Individuals were mounted on tunnel slides and imaged.

For long term imaging, whole polyps were placed in 35 mm plastic dishes in 2 mL 1 mM linalool solution. They were imaged unconstrained with no stage movement once every 5 min for 24 h using an Invitrogen EVOS FL Auto microscope.

A.3.10   Quantification of movement of samples during imaging

To quantify the amount of movement of the samples during imaging, the z-stacks obtained by imaging GCaMP6s animals at 60x and t-stacks obtained by imaging them at 4x were projected using a SD projection in Fiji. The mean gray value of the projection was obtained and divided by the mean grey value of the first image of the z-stack or t-stack to calculate the coefficient of variation.

A.3.11   Regeneration and budding assays

Polyps were decapitated with a scalpel just below the tentacle ring for head regeneration and above the budding zone for foot regeneration assays. In one experiment, the decapitated animals were placed in 600 μL of 0 mM (control), 0.1 mM, 0.25 mM, 0.5 mM, 0.75 mM, or 1 mM linalool in HM. Head regeneration was scored by the appearance of the first tentacle on a decapitated animal. 8 animals were kept at each concentration in a 48-well plate (Eppendorf) and imaged in brightfield at 4x with the Invitrogen EVOS Fl Auto 2. Head regeneration was scored every 12 h for 72 h. The lid of the plate was removed for imaging and the solutions were

changed every 24 h. In another experiment, decapitated polyps were placed individually into the wells of a 24-well plate (Eppendorf), filled either with 500 µL HM or 1 mM linalool. Polyps were imaged approximately every 12 h and the appearance of tentacles and hypostomes were scored. After approximately 3 days, polyps were transferred into a new 24-well plate containing 500 µL fresh HM and imaged a day after transfer. Foot regeneration experiments were conducted the same way, with animals scored for the appearance of a peduncle and for the ability to adhere to the substrate. For repeated imaging of head regeneration at high magnification, animals were anesthetized in 1 mM linalool for 10 min prior to imaging and returned to HM to recover afterwards. To facilitate removal from the slides, a layer of Scotch tape was placed over the double-sided tape during construction of tunnel slides. The increased space between coverslip and slide and ability to easily lift off the coverslip after imaging allowed recovery of the animal with minimal chance of injury.

Budding was assessed by selecting healthy animals with early buds at stages 3–4 on the previously described scale [145], and incubating them in well plates as described for regeneration assays. Animals were scored for development of tentacles on the bud and formation of further buds at the end of 3 days. Long-term imaging of budding was carried out in 35 mm glass bottomed dishes (MatTek, Ashland, MA). One animal was placed onto the glass surface at the bottom of the dish in 1 mM linalool, a coverslip was laid over the top to constrain the animal, and the dish was flooded with 1 mM linalool. Animals were imaged once per hour for 48 h using an Invitrogen EVOS FL Auto microscope.

A.3.12 Cell viability assay

Polyps were incubated for 30 min in 1 µg mL^{-1} propidium iodide in HM, washed twice in HM, then mounted on glass slides as described for live imaging of neurons. Slides were imaged on an Invitrogen EVOS FL Auto microscope in the red fluorescence channel using the Invitrogen EVOS FL Auto Imaging System software. Labeled cells were counted in the body

column only and reported as number of labeled cells per animal. As a positive control, polyps were incubated in 0.04% colchicine (Acros Organics) in HM to induce cell death [146]. Animals were incubated in colchicine for a full 24 h rather than 8 h incubation followed by 16 h recovery as described.

A.3.13   Mitotic index assay

Polyps were incubated in HM or 1 mM linalool for 72 h in 60 mm cell culture dishes at a density of 1 polyp/mL. Polyps were not fed during the experiment, but the medium was changed daily. At the end of the 72 h, one or two cross sectional segments were cut from the body column of each polyp near the head. The samples were placed on glass slides for a wet mount antibody stain. Humid chambers for staining were constructed by lining covered 100 mm Petri dishes (Spectrum Scientific) with wet paper towels and placing the slides inside the dishes. A well was created in the center of each glass slide by layering two pieces of double-sided tape across both short sides of the slide with one piece of tape running on both long edges of the slide. The samples were placed in a drop of medium on the slide. All steps were performed at room temperature unless otherwise noted. The samples were fixed in 20 μL 4% paraformaldehyde (Sigma-Aldrich) in HM for 15 min. The samples were washed three times with 20 μL 1x PBS, followed by a 15 min permeabilization with 20 μL 0.5% PBSTx (0.5% Triton-X in 1x PBS). They were then incubated for 3.5 h in 20 μL blocking solution (1% FBS, 0.1% DMSO in 1x PBS) and placed overnight (16 h) at 4°C in 30 μL anti-phospho-histone H3 (Ser10) primary antibody (Millipore Sigma, Burlington, MA) diluted 1:100 in blocking solution. On the second day, samples were washed quickly 3x with 40 μL 1x PBS, followed by four 25–35 min washes of 20 μL 0.3% PBSTx. The samples were then incubated in a 1:1000 or 1:500 dilution of Alexa 546 rabbit IgG secondary antibody (Thermo-Fisher Scientific) for 5 h, followed by three quick and two 10 min washes of 0.3% PBSTx. To stain nuclei, the samples were incubated in DRAQ5 (Thermo-Fisher Scientific) diluted to 5 μM in 1x PBS for 15 min and then washed three times

with 1x PBS. The 1x PBS was replaced with a 1:1 solution of glycerol and HM. Finally, a cover slip was placed over the samples and nail polish was used to seal the slides. Z-stacks of the cross-sections were imaged using a Leica high-resonance scanning SP5 confocal microscope with a 20x C-Apochromat 1.2 W objective.

To calculate mitotic indices, the number of Alexa 546 stained nuclei was counted for each cross section, divided by the number of nuclei stained by DRAQ5 and multiplied by 100 to obtain a percentage. Counting of Alexa 546 and DRAQ5 stained nuclei was done using Fiji. For the z-stack corresponding to each color channel, a maximum intensity z-projection was taken and binarized. The projection was then segmented using the water-shedding tool. The number of particles was counted using the Analyze Particles tool, with a size range of 10- infinity μm^2. For Alexa 546 color channel stacks, an additional thresholding step was used before binarizing the image.

A.3.14 Comparison of different anesthetics

The different anesthetics were ranked 1–4, based on our direct comparison of their performance and the criteria described in Table A.1. 1 was considered excellent, 2 good, 3 fair and 4 poor. The anesthetics were ranked the same if the difference in relevant values for comparison were not statistically significant.

Table A.1: Criteria of ranking anesthetics.

Readout	Criterion
Induction time	Ranked in increasing order of median induction times (Figure A.8B).
Recovery time	Ranked in increasing order of median recovery times (Figure A.8C).
Lethality	Ranked in decreasing order of fraction of surviving animals at the end of 3d incubation (Figure A.17B).
Ease of use	Ranked based on availability as solid or liquid, with liquids ranking higher, and on toxicity (requiring handling in a fume hood or not).
Morphology	Ranked on basis of closeness to appearance of animal in HM. Effects such as bloating, lumps or stubby tentacles were ranked lower (Figure A.7A).
Immobilization	Quality of z-projections of z-stacks of neuronal GCaMP6s animals were taken at 60x (Figure A.7B).

A.4 Results

A.4.1 Linalool is a fast acting and reversible anesthetic

Intact polyps in *Hydra* Medium (HM) continuously exhibit body shape changes such as contractions, extensions, bending, as well as tentacle movements [115, 147], which complicates *in vivo* manipulations and imaging. In contrast, animals incubated in 1 mM linalool (LL) for 10 min appear relaxed, with tentacles splayed out and the mouth assuming a conical shape (Figure A.1A).

We investigated the effect of various linalool concentrations on animal health within 3 h of incubation (Figure A.1B) and found that concentrations ≥ 2 mM caused negative health effects on the animals, such as an abnormal body shape, contracted tentacles, and partial disintegration (Figure A.9). Death was observed at concentrations of 3 mM and beyond, following the 3 h exposure. We determined the LC_{50} to be 3.31 mM (95% confidence interval 3.27 mM to 3.36 mM) using the same approach as in [143]. We then empirically determined the optimal working concentration for linalool by measuring and comparing induction and recovery times for different sublethal concentrations.

No negative health effects were observed at or below 1mM linalool. Induction time of

anesthesia decreased with increasing concentration of linalool to about 10 min at 1mM (Figure A.1C), while recovery time remained between 10–20 min for all concentrations tested (Figure A.1D). After a 1 h incubation in 1 mM linalool, polyps regained their spontaneous contractions in about 13.0 (8.8, 17.2) min (mean (95% confidence interval), n = 12 across 3 technical replicates) (Figure A.1D). Therefore, we determined that the highest tolerated dose, 1 mM, was the best concentration to use in experiments.

Polyps incubated in 1 mM linalool for 10 min no longer exhibit the "pinch response", a global longitudinal contraction that is observed upon gently squeezing the body column of a polyp in HM with forceps (Figure A.1Ei and Figure A.1Eii, S1 Movie). Polyps in 1 mM linalool swelled at the site of pinching but did not contract globally (Figure A.1Eiii and Figure A.1Eiv). However, upon being returned to HM, the polyps regained their response to pinching within 5 min (n = 18, across 3 replicates, Figure A.10A). Taken together, these results demonstrate that linalool prevents both spontaneous and mechanically induced contractions in *Hydra*.

Mechanically induced body column contractions are known to be mediated by the ectodermal epithelial layer, and epithelial (nerve-free) animals in HM retain their pinch response despite lacking spontaneous contraction behaviors [134]. Therefore, to determine whether linalool affected epithelial cells directly, we tested whether nerve-free Hydra exhibited a pinch response in linalool. As was the case for enervated polyps, nerve-free animals lost their pinch response in linalool (S2 Movie). The loss of both spontaneous and mechanically induced contractions, in both enervated (Figure A.1Eiii and Figure A.1Eiv) and nerve free animals (S2 Movie) upon treatment with linalool suggests that linalool affects both the neuronal and epithelial cells.

However, 1 mM linalool does not completely paralyze the animal—we observed that some anesthetized individuals were able to capture and ingest *Artemia* (brine shrimp), although very inefficiently compared to controls (Figure A.1F). We quantified the feeding response by adapting the protocol by [148]. While we found *Artemia* readily stuck to the tentacles of most

animals, only 2 out of 9 animals in 1 mM linalool ingested 1 *Artemia* each in 30 min, whereas the median number of *Artemia* ingested by each animal incubated in HM was significantly higher (p = 0.00028, Mann-Whitney U test) with 13 (11, 16; 25th percentile, 75th percentile) for n = 9 polyps across 2 technical replicates. (Figure A.10D).

The effect of linalool treatment on mechanically induced contraction and the ability to feed was rapidly reversed by moving the polyps back into HM. Following a 10 min incubation in 1 mM linalool, polyps regained the mechanically induced pinch response within 5 min of return to HM (n = 18 across 3 technical replicates; Figure A.10A). The ability to capture and ingest *Artemia* was restored within 15 min of HM incubation following a 10–15 min incubation in 1 mM linalool, as quantified by the fraction of polyps that were able to capture and ingest *Artemia* at different time points after the linalool incubation (Figure A.10C).

A.4.2 1 mM linalool enables precise tissue manipulations

Recent studies have shown that the regeneration outcome in *Hydra* could be influenced by the geometry of tissue pieces excised from the body column [66]. Making precise cuts is also useful for manual sections of the body column for use in immunohistochemistry and histology. To test whether linalool allowed for improved precision of cuts and thus would be a useful tool for such studies, we compared the excision of tissue rings from animals incubated in HM with those incubated in 1 mM linalool. When sectioning animals to obtain pieces of body column tissue, the application of linalool did not drastically improve the average thickness of the sections (Figure A.2Av), but significantly reduced the time required to section the animals from 99 ± 45 s (mean ± standard deviation (SD), n = 13 across 3 technical replicates) per animal in HM to 40 ± 9 s (mean ± SD, n = 16 across 5 technical replicates) per animal in 1 mM linalool (p = 0.00002, 2-tailed t-test) (Figure A.2Aiv). The reductions in variability and in average time are due to the suppression of the animal's natural contractile response to touch, removing the need to wait for the polyp to extend following each cut.

The improvements possible using linalool become more readily apparent in grafting experiments. A "zebra graft" to create a chimeric animal consisting of bands of differently labeled tissue produced a significantly better result when linalool was employed (Figure A.2B). While the time to assemble the grafts was comparable with or without linalool treatment (Figure A.2Biv), the average number of segments per graft was significantly higher (p = 0.03, 2-tailed t-test) for grafts in linalool (8 $\pm$ 1 segments per graft, n = 8 grafts) than those made in HM (5 $\pm$ 2 segments per graft, n = 8 grafts; Figure A.2Bv). This difference is due to a combination of two effects. First, the animals do not move in linalool and second, they are extended. Thus, they are more quickly and easily cut into smaller segments, which are in turn easier to thread onto a needle. Morphology of grafts made in HM was also more frequently abnormal compared to those made in linalool (Figure A.11). The observed morphological abnormalities are likely due to tissue movement during healing, causing the cut edges of the pieces to become misaligned while on the needle, thus preventing the segments from healing smoothly together as described previously [149]. A similar effect was observed when grafting heads onto body columns (n = 3 per condition), following the procedure described in [150]. Linalool allowed more precise decapitation of the donor animal, reducing the amount of extraneous body column tissue, and guaranteed better positioning of the graft on the recipient animal. Grafts carried out in HM tend to have the donor head protruding at an angle, again due to misalignment of the cut surfaces during healing (Figure A.2C).

Finally, linalool is beneficial in hypostome grafts, carried out as previously described [98]. We conducted 25 hypostome grafts each in HM and in 1 mM linalool and scored at 4 days after grafting for retention of donor tissue and for formation of an ectopic body axis from recipient tissue with donor tissue limited to a small part of the new head (Figure A.2Diii), as in [98, 117]. Grafts that retained donor tissue but failed to induce an axis fell into several broad categories: donor tissue that either failed to form any structure or induced only a tentacle before being reabsorbed (Figure A.2Dii), or donor tissue that formed the entirety of an ectopic head

143

with no host tissue involvement (Figure A.12). We found a slight but statistically non-significant improvement in the number of grafts that induce an ectopic axis when linalool is used (6/25 in HM vs. 11/25 in linalool). For two technical replicates containing n = 16 grafts per condition, we individually recorded the time taken to excise the donor hypostome and to conduct the graft. Linalool did not significantly improve the time required to cut hypostomes (p = 0.1221, Mann-Whitney U test), but grafting times were significantly shorter (p = 0.0226, Mann-Whitney U test) in linalool, with 134 s (104, 209; median, (25th quartile, 75th quartile)), compared to in HM with 196 s (147, 258).

A.4.3   Incubation in 1 mM linalool enables high quality short-term fluorescence imaging

To test whether the immobilization in 1 mM linalool was sufficient to allow for in vivo fluorescence imaging, we imaged animals incubated in 1mM linalool under various conditions and compared the results to those obtained from imaging animals in HM.

First, we used single channel fluorescence imaging using polyps expressing GCaMP6s in the interstitial cell lineage [97], because this transgenic line allows for the visualization of individual neurons and subcellular processes such as dendrites. We imaged unconstrained animals at low magnification (Figure A.3A-B, S3 Movie). Unconstrained animals in HM moved significantly during the 10 s acquisition, as shown by a maximum intensity projection of the time series (Figure A.3A-Bii). In contrast, polyps incubated in 1 mM linalool for at least 10 min only exhibited drift (Figure A.3Bi-ii), which can be corrected for with standard post-processing methods (Figure A.3Biii), whereas these methods do not correct for the motion observed in the control, because the animal exhibits non-linear body shape changes (Figure A.3Aiii).

We also acquired 7.5 µm thick z-stacks of the body columns of intact polyps mounted in tunnel slides [83] at high magnification (Figure A.3A,Biv-v). The image quality of individual slices was better when imaging anesthetized animals (Figure A.3B), but the difference in stability

and thus image quality becomes most evident when comparing maximum intensity projections of the entire z-stack (Figure A.3Av and A.3Bv). The animals in linalool were sufficiently still to allow the resolution of subcellular features such as neuronal processes, whereas the animals in HM moved too much, making z-stacks impractical (Figure A.3A-Bv and S4 Movie). As the tissue stretched and compressed anisotropically during those movements, it was not possible to correct this motion through post-processing. We quantified the motion under these two imaging conditions (HM, 1 mM linalool) using the coefficient of variation (see Methods). As expected from the images (Figure A.3), the coefficient of variation was significantly higher for image sequences acquired in HM than for those acquired in 1 mM linalool (Table A.3, Figure A.3C).

Next, we tested the performance of 10 min incubation in 1mM linalool for the acquisition of multi-channel z-stacks at low (10x) and high magnification (60x). Control videos in HM were not attempted due to the unsatisfactory results obtained in single channel imaging as described in the preceding paragraphs (Figure A.3). By exposing animals to 1mM linalool in the presence of 2mM reduced glutathione, we were able to induce mouth opening (Figure A.4A). The animal is sufficiently still to allow for simultaneous visualization of nuclei positions and cell boundaries using different excitation wavelengths at 10x magnification. We also took 3-channel time-lapse movies of heads exposed to reduced glutathione below the activation threshold for opening to illustrate the overall stability that can be achieved using linalool, allowing for co-localization studies of dynamic processes (S5 Movie).

Furthermore, we used mouth opening to test if calcium imaging was possible in linalool-treated animals. Epithelial GCaMP animals [98] incubated in 1mM linalool for 10 min opened their mouth in response to 2mM reduced glutathione and calcium waves could be observed (S6 Movie). We also observed local calcium signaling in the body column in response to pinching with tweezers (S8 Movie). Together, these data demonstrate that linalool does not interfere with epithelial calcium signaling and that behaviors that are not suppressed by linalool can be

studied using GCaMP animals.

Finally, we tested whether animals were sufficiently immobile to obtain high quality z-stacks at high magnification (60x) in multiple channels (UV, blue, and green excitation; Figure A.4B). Notably, when testing live dyes for this purpose, we found that the SYTO 60 red fluorescent nucleic acid stain is specific to nematocysts of all types in *Hydra* (Figure A.4Biii), determined by comparing morphology of stained structures to previous descriptions of nematocyst types [151]. Thus, SYTO 60 is a useful tool for studying nematocysts in vivo.

While motion was not completely suppressed in 1 mM linalool and extended exposure to short wavelength light caused the animal to escape the field of view, it was nevertheless possible to achieve high quality multichannel imaging (Figure A.4B). Thus, linalool is a useful tool for *in vivo* co-localization studies at high magnification, which are impossible to perform in HM.

A.4.4   Linalool allows for repeated short-term fluorescence imaging

A major strength of linalool as a reversible anesthetic is the ability to repeatedly anesthetize and image the same animal over the course of days, thus allowing the acquisition of dynamic data of cellular processes in a single animal. To illustrate this capability, we decapitated transgenic HyBra2 promoter::GFP animals and allowed them to regenerate in HM. We imaged head regeneration over the course of 2 days, using repeated short-term 15 min incubations in 1 mM linalool to acquire a total of 11 high resolution images of the same animal (Figure A.5A). When not being imaged, the regenerating animals were returned to HM. In this way we were able to observe the development of the hypostome and tentacles and also observe a gradual increase in GFP signal beginning at 24 h. The same technique of repeated linalool exposure was used to image the tissue grafts in Figure A.2.

We also confirmed that the timing and outcome of head regeneration in animals repeatedly anesthetized for imaging did not significantly differ from that observed in untreated

controls (Figure A.5B). Thus, linalool is a valuable tool for repeated live imaging applications, which will be useful to study long term processes, such as regeneration and budding.

A.4.5   Long-term effects of linalool

Due to the reported cytostatic effect of linalool on cancer cells in culture [140], we investigated whether linalool has similar effects in *Hydra*. The cell cycle lengths in interstitial and epithelial cells are approximately 1 [102] and 3 days [152], respectively. Therefore, we continuously incubated intact polyps for 3 days in 1 mM linalool, exchanging the solution every 24 h to account for volatility. We did not observe significant changes in the mitotic index (Figure A.6A) nor in the rate of cell death (Figure A.6B) in the body column of intact polyps. Furthermore, budding seemed to occur normally, as verified using 3-day continuous time-lapse imaging (Figure A.6C, A.13).

Based on these results, we attempted to image head regeneration using continuous incubation in 1 mM linalool. Continuous incubation would be advantageous compared to consecutive mounting and imaging sessions as it would minimize interaction with the sample and could be fully automated. We found that decapitated *Hydra* experienced a significant delay in head regeneration when continuously exposed to 1 mM linalool over the course of 3 days. Anesthetized body columns were observed to shed cells and assume a lollipop shape (Figure A.6Ei and 6Eii), and a few animals disintegrated completely. A third of the animals (14/42 across 4 technical replicates) were less affected and showed 1–2 small tentacle buds at the end of 3 days (Figure A.14). If removed from linalool after 3 days, however, the remaining two thirds of the animals, which showed no visible signs of regeneration, recovered. Tentacle buds were observed as early as 1 day into recovery and all polyps had fully regenerated their heads after 3 days of recovery (Figure A.6E). Foot regeneration was similarly suppressed in 3-day continuous 1 mM linalool exposure and was also rescued after the animals were moved into HM (Figure A.15). This suggests that the effects of linalool on regeneration are not specific to the head.

The observed head regeneration delay in continuous linalool exposure was observed for concentrations as low as 0.5 mM for up to 48 h (Figure A.6D), and at 0.75 mM, 50% of the animals did not regenerate heads within 3 days. However, since even 1 mM linalool was ineffective in sufficiently immobilizing animals to allow for long-term imaging with cellular resolution (S7 Movie), these lower concentrations are not viable alternatives.

Finally, we tested whether the inhibition of regeneration is caused by an effect on the nervous system, as it had previously been suggested that the nervous system plays a role in head regeneration [153]. To this end, we generated nerve-free animals as described in Methods and assayed head regeneration in 1 mM linalool. Surprisingly, nerve-free animals in 1 mM linalool regenerated similarly to nerve-free animals maintained in HM. After 4 days of regeneration, 7/10 animals in HM and 4/10 in linalool showed tentacle buds across two technical replicates. By 5 days this had increased to 9/10 in HM and 6/10 in linalool (Figure A.16). There were no statistically significant differences in the fraction of head regenerates for both days (p = 0.36 for day 4 and p = 0.30 for day 5, Fisher's Exact test). Furthermore, nerve-free animals in linalool did not assume the lollipop shape (Figure A.6Eii) that we observed in enervated polyps. Together, these data suggest that linalool disrupts regeneration by perturbing the function of either neurons or other cells in the interstitial lineage.

A.4.6 Comparison of linalool to other commonly used anesthetics in Hydra research

Whenever one introduces a new tool, it is important to compare performance with existing methods and demonstrate that the advantages of the new tool are sufficient to make its adoption worthwhile. While anesthetics were and continue to be most frequently used to relax *Hydra* prior to fixation for histological and immunohistochemistry studies [63, 126, 128, 154], the advent of modern molecular tools have brought with it an increased use for *in vivo* applications [58, 127, 131]. Table A.2 provides an overview of the various anesthetics that have

been reported in the literature for use in *Hydra* and examples of their respective applications.

Based on our literature search, the most prominent *in vivo* application of the anesthetics was fluorescence imaging using urethane, heptanol, or chloretone. We therefore compared linalool to these anesthetics. To this end we studied whether there were any differences in morphology when *Hydra* polyps are exposed to the different substances. Although we observed variability among individual polyps exposed to the same anesthetic at a fixed concentration, both in terms of morphology and in terms of immobilization speed and strength, polyps assumed characteristic shapes upon exposure to the different chemicals (Figure A.7A). Following a 15 min exposure, *Hydra* polyps incubated in 1 mM linalool appear relaxed with tentacles splayed outwards and had cone-shaped hypostomes (Figure A.7Ai). This morphology does not change significantly by 60 min. Animals incubated in 0.04% heptanol appear less extended at 15 min, with contracted conical tentacles. At 60 min the body columns are contracted, and the stubby tentacles persist (Figure A.7Aii). Exposure to 2% urethane causes animals to extend and become very thin at 15 min, though they become swollen while remaining extended by 60 min (Figure A.7Aiii). 0.1% chloretone causes initial extension without the thinness seen in urethane, followed by the formation of swellings along the body column by 15 min and contraction of both body and tentacles by 60 min (Figure A.7Aiv). To quantify these differences, we calculated average body length of individual animals after 10 min incubation in anesthetic as a percentage of their average length prior to anesthesia (see Methods and Figure A.8).

We found that linalool, heptanol and urethane produced similar anesthetized lengths at 10 min, while chloretone showed a statistically significant increase in length at the 5% level and some hyperextended animals (Figure A.8A and 8D). Because this length measure does not account for the other morphological characteristics described above (e.g. the contracted tentacles in heptanol or the formation of bumps in the body column of chloretone-treated animals) nor for the changes in morphology that were observed for heptanol and chloretone over time, we also qualitatively compared the body shapes of the anesthetized animals (Figure

Table A.2: Summary of various anesthetics used to relax *Hydra*. Note that this table is not a comprehensive summary of all *Hydra* studies that have employed anesthetics but provides an overview of examples spanning different chemicals and applications. To the best of our knowledge such a direct comparison has not previously been attempted and is thus a useful resource for the field.

Chemical	Working concentration	Application	Treatment duration	Health effects	References
Urethane	2% w/v	Determination of mechanism of urethane's action		Hyperextension; potential reversal; structural damage	[125]
	1-3% w/v	Relaxation prior to fixation	2-20 min	None reported	[63, 126, 128, 154, 155]
	2% w/v	Fluorescence microscopy	Not reported	None reported	[127]
	0.05 M	Inhibition of feeding reaction	Not reported	None reported	[132]
Chlorobutanol (chloretone)	0.1-0.33% w/v in bath	Reactions to chloretone exposure on 3 Hydra species	several hours	No apparent damage at low concentrations; habituation	[133]
	0.003 M	Inhibition of feeding reaction	Not reported	None reported	[132]
	0.1% w/v	Fluorescence imaging	Not reported	None reported	[58, 131]
1-Heptanol	3 mM	RNA interference	10 min in 4°C	None reported	[129]
	1% v/v	Fluorescence microscopy	Not reported	None reported	[130]
Magnesium chloride	2.5% w/v	Inhibition of feeding reaction	5 min	Extensive damage with exposure >1 hr	[83]
Menthol	Not reported	Relaxation prior to fixation	Not reported	None reported	[156, 157]
	Not reported	Inhibition of feeding reaction	Not reported	Disintegration	[83]
MS-222	0.1%	Inhibition of feeding reaction	Not reported	None reported	[132]

A.7A) to those of untreated animals. Because the morphologies in linalool and urethane were the most similar to the untreated body morphology and did not change much over the course of 60 min incubation, we ranked morphology in linalool and urethane as the best, followed by heptanol (contracted body and tentacles, changing shape), and chloretone (hyperextended, contracted tentacles, bumps, changing shape).

Because most published studies specified only the concentration of anesthetic used and not the incubation time, we used concentrations that have been reported in the literature to be effective for the different anesthetics and measured induction and recovery times for direct comparison to linalool. Anesthesia in linalool is induced slower than in other anesthetics (Figure A.8B and 8E). Recovery times were statistically similar between all anesthetics, with most polyps resuming normal activity within 10–20 min post-exposure (Figure A.8C and 8F).

Finally, we compared the effects of long-term exposure to the different anesthetics. First, we tested a 3-day exposure to the anesthetics without changing the medium, as would be necessary for long term immobilization for continuous imaging, as in the example shown in Figure A.6C for 1 mM linalool. While 1 mM linalool does not negatively affect intact polyps (Figure A.6), all polyps disintegrated within 24 h upon continuous exposure to 2% urethane (Figure A.17). Under the same conditions, chloretone caused disintegration in 50% of the animals after 24 h, with most polyps disintegrating by 72 h (Figure A.17). The animals that survived the 3-day chloretone treatment without solution exchange had a fairly normal morphology and pinch response, potentially due to a developed tolerance, as previously suggested [133]. Heptanol was not lethal to *Hydra* over 3 days (Figure A.17), but as with chloretone the animals regained normal morphology and pinch response by the third day.

Subsequently we tested a 3-day incubation with media changes every 24 h, to determine whether performance could be improved by constant refreshing of the anesthetic. As seen with the previous experiment, polyps in urethane died within the first 24 h and polyps in linalool were still alive at the end of 72 h. Survival in chloretone was reduced as all polyps had died by

48 h. Similarly, only about 60% of the polyps survived in heptanol by 72 h (Figure A.17).

We also compared the performance of these various anesthetics for single and dual channel high magnification fluorescent live imaging of GCaMP6s (Figure A.7B) and WM animals labeled with Hoechst (Figure A.7C), respectively and did not observe a notable difference in image quality between the anesthetics.

Using these comparative data, we ranked the performance of the anesthetics in the six categories we tested (Figure A.8G and Methods): ease of use, animal morphology upon exposure to anesthetic, induction and recovery times, immobilization/imaging quality, and negative health effects. As liquids, heptanol and linalool solutions are easier and quicker to prepare than urethane or chloretone, which are supplied as solids (see Methods). Morphology is closest to normal and remains stable over the course of at least 1 hour incubation in urethane and linalool (Figure A.7A and Figure A.8A and 8D). Induction was slightly slower in linalool compared to the other three anesthetics (Figure A.8B and 8E), but recovery times after short-term exposure were similar (Figure A.8C and 8F). All anesthetics tied regarding immobilization/imaging quality (Figure A.7B and 7C). Linalool stands out with the least negative health effects–in contrast to the situation in the other anesthetics, not a single animal died in linalool at the end of 3-day exposures (Figure A.17), making linalool the compound of choice for multi-day applications. In summary, linalool ties for best on 3/6 criteria and scores best for 2/6. Thus, based on these six criteria, linalool's overall performance is superior to currently used anesthetics.
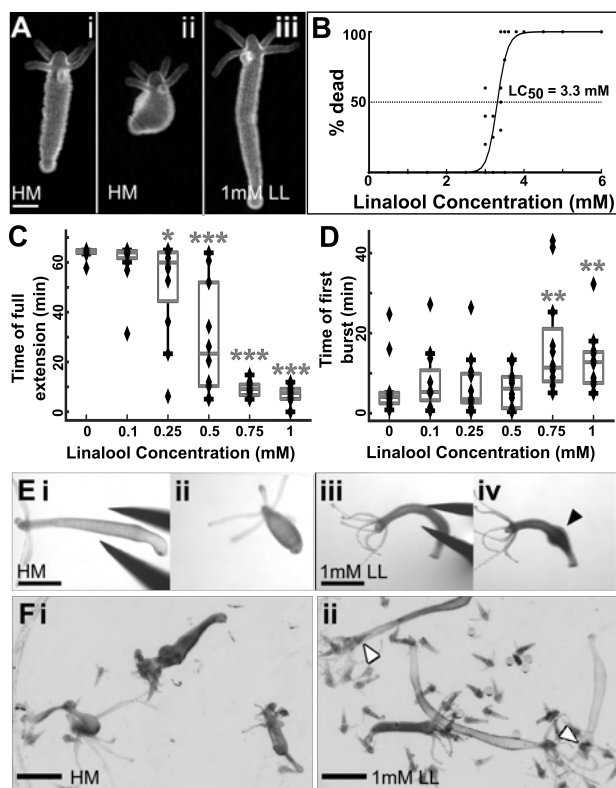
Figure A.1: Linalool as an anesthetic. A. Representative images of *Hydra* polyps before (i. extended, ii. contracted) and after (iii) incubation in 1 mM linalool (abbreviated to LL). Scale bar: 200 µm. B. 3 h incubation in linalool concentrations exceeding 3 mM causes lethality. Each point represents a single technical replicate containing 8–10 animals. C. Box plot showing time of full extension after last observed contraction burst during 65 min incubation in linalool concentrations up to 1 mM. 1mM linalool takes 7.53 min (5.44, 9.03) (median (25th percentile, 75th percentile)) to anesthetize the animals. (*), (**) and (***) indicate statistically significant difference from 0 mM linalool at $p < 0.05$, $p < 0.01$ and $p < 0.001$ respectively (Mann-Whitney U test). Data from 3 technical replicates containing 3–4 animals each for every concentration. Each data point corresponds to one animal. D. Box plot showing time of first observed contraction burst during 120 min recovery in HM following 65 min of anesthesia in linalool. Animals recover in 12.77 min (7.72, 15.13) (median (25th percentile, 75th percentile)) after incubation in 1mM linalool. (*), (**) and (***) indicate statistically significant difference from 0 mM linalool at $p < 0.05$, $p < 0.01$ and $p < 0.001$ respectively (Mann-Whitney U test). Data from 3 technical replicates containing 4 animals each for every concentration. Each data point corresponds to one animal. E. Pinch response. i. Hydra polyp in HM. ii. Polyp in HM shows a global body column contraction in response to pinching. iii. *Hydra* polyp incubated in 1 mM linalool for 10 min. iv. Anesthetized polyp shows only local swelling after pinch, indicated by black arrowhead. Images representative of n = 5 animals per replicate in 2 technical replicates. F. 30 min feeding response in 4-day starved polyp. i. *Hydra* polyps in HM readily capture and ingest *Artemia* (brine shrimp), with multiple *Artemia* clearly visible within the body column of each animal. ii. *Hydra* polyps incubated in linalool for 10 min prior to introduction of *Artemia* have a strongly reduced reaction, and only rarely ingest *Artemia*. White arrowheads indicate *Artemia* inside polyps. Several animals have not ingested prey at all, and those that have contain a maximum of one *Artemia* each. Scale bars for E, F: 1 mm.
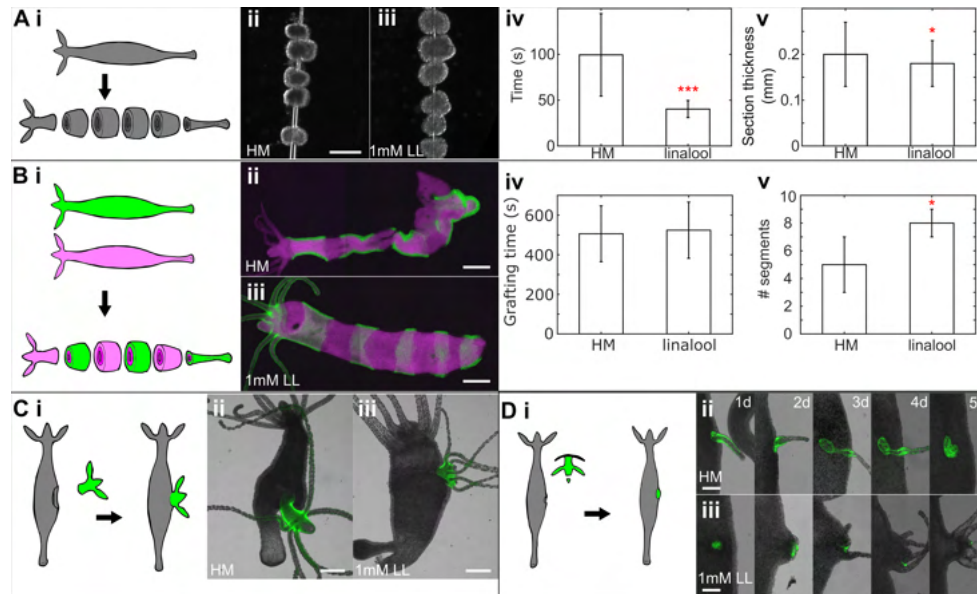
153

Figure A.2: Linalool improves outcomes of surgical manipulations in *Hydra*. A. Sectioning of body column. i. Experimental schematic. ii. Sections cut in HM. iii. Sections cut in linalool. Scale bar: 400 μm iv. Time required to section a polyp in *Hydra* medium (HM) (90 ± 45 s (mean ± SD), n = 13, across 3 technical replicates) and in 1mM linalool (40 ± 9 s, n = 16, across 5 technical replicates). v. Thickness of body column sections cut in HM (0.20 ±0.07 mm (mean± SD), n = 66 sections, 15 polyps across 4 technical replicates) and in 1mM linalool (0.18 ± 0.05 mm, n = 99 sections, 19 polyps across 6 technical replicates). Error bars represent SDs. (*), (**) and (***) indicate statistical significance at $p < 0.05$, $p < 0.01$ and $p < 0.001$ respectively, calculated using a 2 tailed t-test. B. "Zebra grafting". i. Experimental schematic. ii. Representative animal grafted and healed in HM. iii. Representative animal grafted and healed in linalool. Scale bars: 400 μm. All grafts are shown in (Figure A.11) iv. Time taken to assemble grafts in HM (506 ± 141 s (mean ± SD)) and in 1 mM linalool (524 ± 142) (n = 8, across 2 technical replicates each for HM and 1 mM linalool). v. Number of segments in completed graft in HM (5 ± 2 (mean ± SD)) and in 1 mM linalool (8 ± 1) (n = 8, across 2 technical replicates each for HM and 1 mM linalool). Error bars represent SDs. (*) indicates statistically significant difference from grafts in HM at $p < 0.05$ (2-tailed t-test). C. Head transplantation into gastric region. i. Experimental schematic. ii. Representative animal grafted and healed in HM. iii. Representative animal grafted and healed in 1mM linalool. Scale bars: 400 μm. D. Head organizer transplantation into gastric region. i. Experimental schematic. ii. Animal grafted in HM imaged daily over 5 days. iii. Animal grafted in 1 mM linalool imaged daily over 5 days. Scale bars: 200 μm. Linalool did not improve hypostome cutting times, which were 60 s (50, 69) (median, (25th quartile, 75th quartile), measured for n = 17 grafts) in HM and 50 s, (38, 66) (n = 17) in linalool, but slightly improved success of the induction of ectopic axes (6/25 in HM versus 11/25 in linalool) and significantly shortened grafting time to 134 s (104, 209) (n = 17) compared to 196 s (147, 258) (n = 17) in HM.
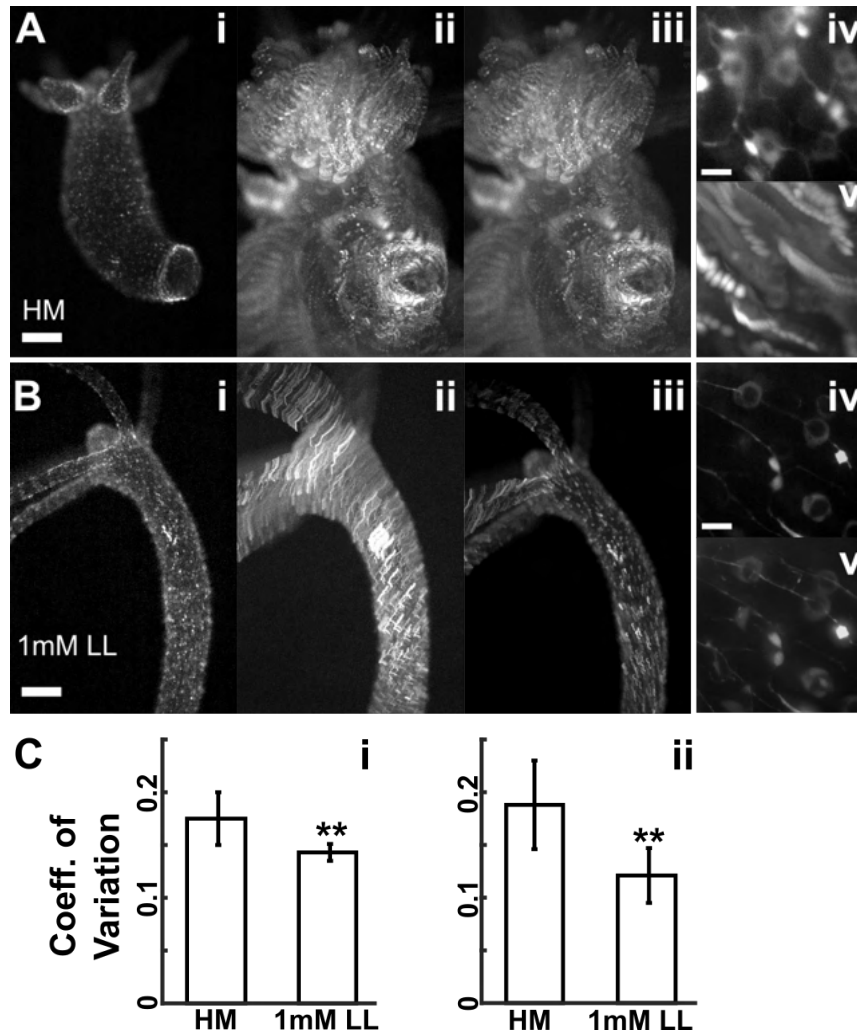
Figure A.3: Single channel live imaging in linalool. Single channel live imaging in A. HM and B. 1mM Linalool. For each condition, the images are i. Single image at 4x magnification, ii. Maximum intensity t-projection of a 10 s video at 4x magnification, iii. Rigid body correction of the video projection (Scale bar: 200 μm), iv. Single slice from a 7.5 μm thick z-stack of a GCaMP6s animal imaged at 60x magnification with a resolution of 0.25 μm along the z-axis at a 500 ms exposure per slice using blue excitation and, v. Maximum intensity projection of high magnification z-stacks (Scale bar: 10 μm) C. Coefficient of variation for i. low magnification imaging in HM (0.175 ± 0.025 (mean $\pm$ SD)) and linalool (0.143 ± 0.008) calculated from n = 10 polyps across 2 technical replicates ii. high magnification imaging in HM (0.188 ± 0.042 (mean $\pm$ SD)) and linalool (0.121 ± 0.026) calculated from n = 6 polyps across 2 technical replicates. Error bars represent SDs. (**) indicates statistically significant difference at $p < 0.01$ as determined by a 2 tailed t-test.
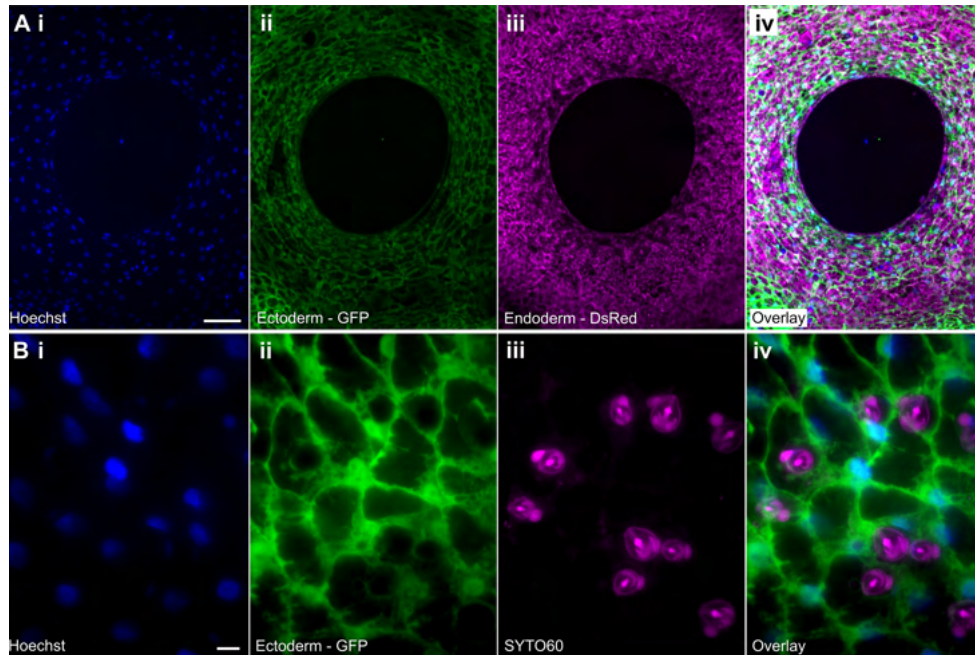
Figure A.4: Linalool enables high resolution imaging in multiple channels. A. Low magnification maximum intensity projection of a z-stack acquired of an open *Hydra* mouth in 1mM linalool using i. Hoechst 33342, ii. Ectoderm—GFP, iii. Endoderm–DsRed2, iv. overlay. 5 µm slice thickness, 6 slices total. Scale bar: 100 µm. B. High magnification maximum intensity projection of a z-stack of the body column tissue acquired in 1mM linalool using i. Hoechst 33342, ii. Ectoderm–GFP, iii. Nematocysts–SYTO 60, iv. overlay. 0.25 µm z-step, 17 slices total. Scale bar: 10 µm. The reduced animal motion allows for acquisition of multiple z-slices in 3 channels.
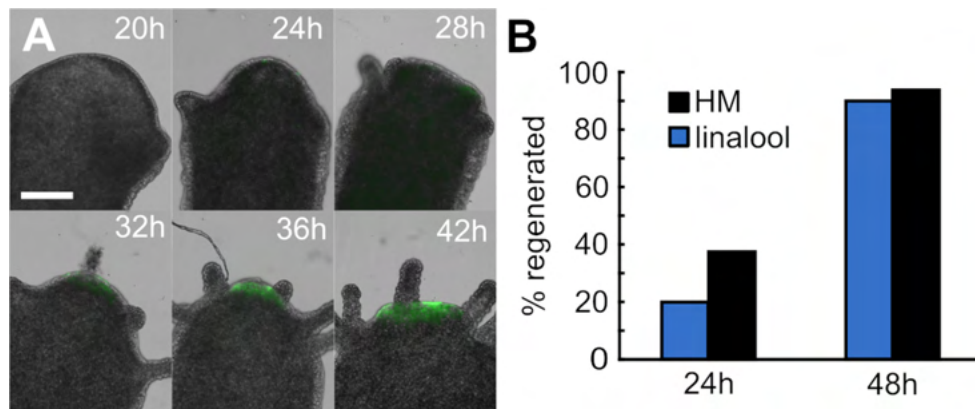
Figure A.5: Linalool enables repeated high-resolution imaging. A. Head regeneration in a transgenic HyBra2 promoter::GFP polyp imaged at high resolution every 4 h from 12 h to 48 h. Subset of images shown. Scale bar: 0.5 mm B. Repeated anesthesia and recovery do not impact regeneration speed or outcome (n = 10 animals HM, n = 16 animals linalool, 3 technical replicates). Differences between conditions not statistically significant at p = 0.05 level (Fisher's Exact test).
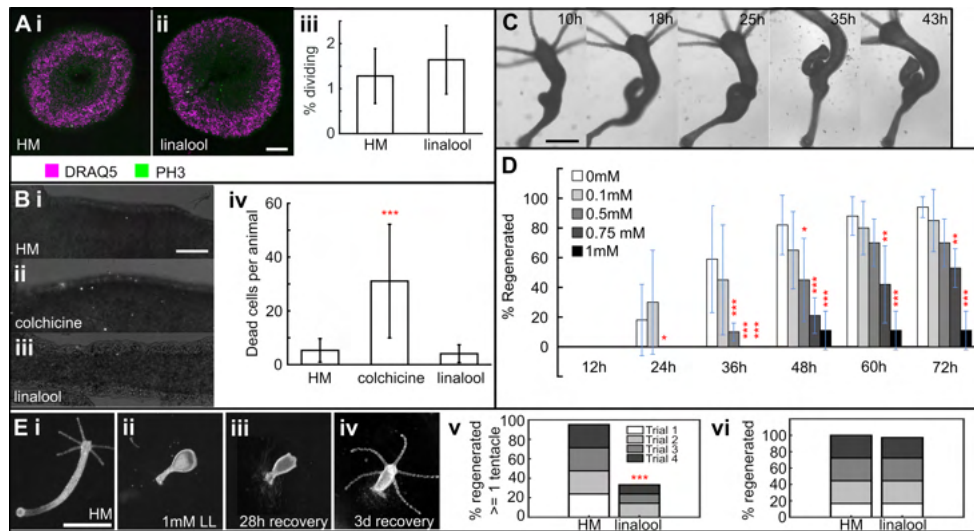
Figure A.6: Effect of long-term continuous linalool exposure. A. 3-day incubation in 1 mM linalool does not impact rate of cell division. Slices stained with DRAQ5 (nuclei) and anti-PH3 (phospho-histone H3, dividing cells). i. Representative image of body column sections from polyps incubated 3 days in HM. ii. Representative slice from polyps incubated 3 days in 1 mM linalool. iii. Percentage of dividing cells in animals incubated 3 days in HM or 1mM linalool. Mean $\pm$ SD: HM = 1.3 $\pm$ 0.6, linalool = 1.6 $\pm$ 0.8. n = 18 across 5 technical replicates. Difference not statistically significant at p< 0.05 (2-tailed t-test). Error bars represent SD. Scale bar: 100 μm. B. 3-day incubation in 1 mM linalool does not damage or kill cells. Representative images of polyps stained with propidium iodide after incubating for i. 3 days in HM, ii. 24 h in 0.04% colchicine, and iii. 3 days in 1 mM linalool. iv. Mean number of dead cells per animal after incubation in HM (5 $\pm$ 4, n = 38), in colchicine (31 $\pm$ 21, n = 28) and linalool (4 $\pm$ 3, n = 39). Error bars represent SD. (***) indicates statistically significant difference from linalool at p < 0.001 (2-tailed t-test). Scale bar: 100 μm. C. Long term incubation in linalool does not impact budding. Representative images of a budding polyp continuously incubated and imaged in 1 mM linalool. Scale bar: 500 μm. D. Long term incubation in linalool prevents head regeneration. Error bars represent SD (0 mM n = 17, 0.1 mM n = 20, 0.5 mM n = 40, 0.75 mM n = 19, 1 mM n = 19; 3 technical replicates). (*), (**) and (***) indicate statistically significant difference from 0 mM at p<0.05, p<0.01 and p<0.001 respectively (Fisher's Exact Test). E. Recovery in HM rescues the head regeneration defect. i. Polyp incubated in HM for 68 h after decapitation. ii. Polyp incubated in 1 mM linalool for 68 h after decapitation. iii. Decapitated polyp recovered for 28 h after 3 days in 1mM linalool, iv. Polyps recovered for 3 days after 3 days in 1mM linalool. Scale bar: 1 mm. v. Head regeneration is suppressed by incubation for 3 days in 1 mM linalool. Only 14/42 polyps incubated in 1 mM linalool regenerated at least one tentacle at the end of 3-day incubation compared to 40/42 polyps in HM (across 4 technical replicates). (***) denotes that the difference is statistically significant at p<0.001 (Fisher's Exact test) when comparing overall numbers. vi. Head regeneration is rescued in linalool- incubated animals after 3-day recovery in HM. 35/36 polyps incubated in 1 mM linalool regenerated heads at the end of 3-day recovery compared to 36/36 polyps in HM, across 4 technical replicates. The difference is not statistically significant at p<0.05 (Fisher's Exact test) when comparing overall numbers.
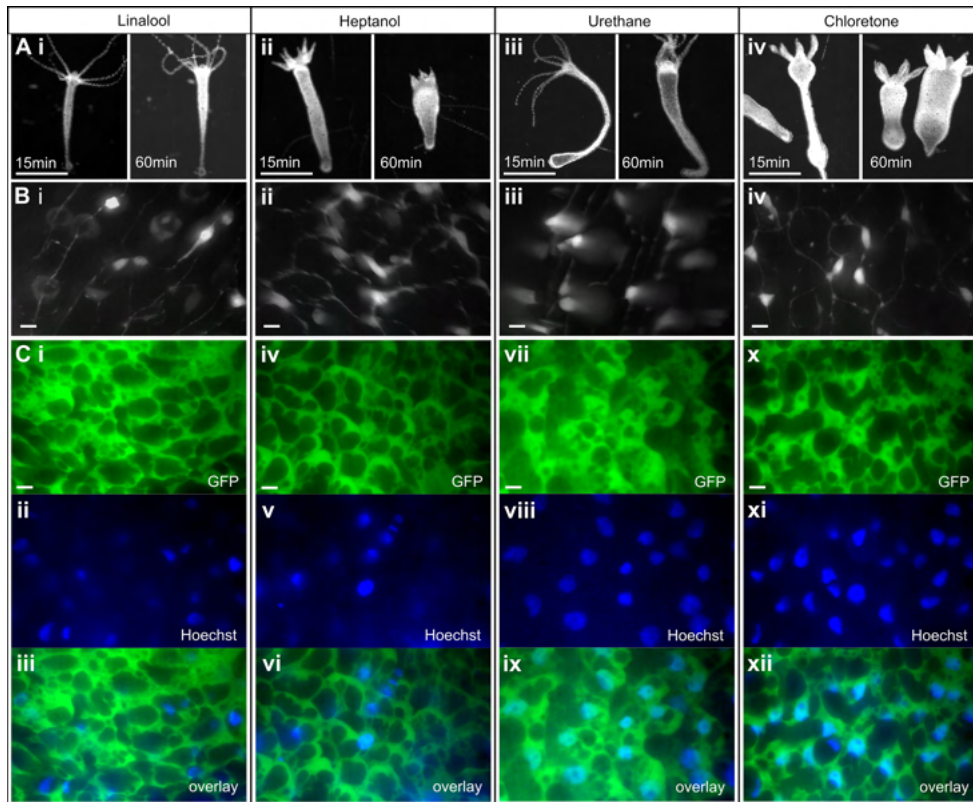
Figure A.7: Comparison of various *Hydra* anesthetics. A. Comparisons of the same animal after 15 min and 60 min of anesthetic exposure. i. 1 mM linalool, ii. 0.04% heptanol, iii. 2% urethane, iv. 0.1% chloretone. Scale bars: 1 mm. B. Maximum intensity projections of GCaMP6s animals at 60x magnification in each anesthetic. Scale bars: 10 μm. C. Maximum intensity projections of two-channel images of watermelon animals stained with Hoechst nuclear dye at 60x magnification. GFP channel, DAPI channel, and merge (overlay) shown for each anesthetic. Scale bars: 10 μm.
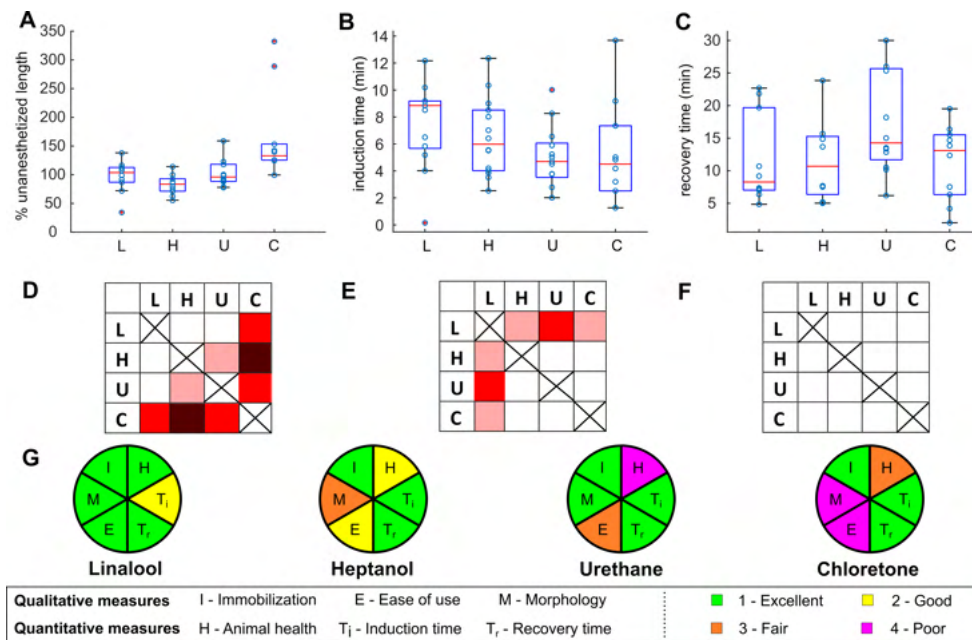
Figure A.8: Comparison of various *Hydra* anesthetics. A. Comparisons of the same animal after 15 min and 60 min of anesthetic exposure. i. 1 mM linalool, ii. 0.04% heptanol, iii. 2% urethane, iv. 0.1% chloretone. Scale bars: 1 mm. B. Maximum intensity projections of GCaMP6s animals at 60x magnification in each anesthetic. Scale bars: 10 μm. C. Maximum intensity projections of two-channel images of watermelon animals stained with Hoechst nuclear dye at 60x magnification. GFP channel, DAPI channel, and merge (overlay) shown for each anesthetic. Scale bars: 10 μm.

A.5 Discussion

Our results show that linalool is a fast-acting, reversible anesthetic for *Hydra*. It is non-toxic and simple to use, and its pleasant smell makes working with it an enjoyable experience. Incubation in 1 mM linalool does not completely immobilize the animal, as mouth opening and feeding are still observed (Figs 1F and 4A); although, feeding is extremely impaired (Figure A.1F, A.10). While *Artemia* frequently get stuck to the tentacles of animals incubated in linalool, few are ingested. This suggests that while nematocyte and mouth function may be normal in linalool-treated animals (Figure A.4A), the movement of food into the body cavity is impaired. As digestive movements have previously been shown to require nervous system function [73], this impairment may be a direct consequence of linalool's effect on the *Hydra* nervous system, as suggested by our data. Our experiments in wildtype and nerve-free animals show the absence of both spontaneous and mechanically induced body column contractions, implying that linalool affects both nervous system and epithelial cells.

In terms of applications, a 10 min incubation in 1 mM linalool significantly decreased polyp movement, allowing for fine surgical manipulations with superior precision, efficiency, and long-term success compared to their execution in HM (Figure A.2). Thus, linalool is a useful tool for grafting and tissue manipulations, especially for novice researchers. We achieved significantly improved fluorescent imaging when compared to HM and were able to acquire high quality single- and multi-channel fluorescent z-stacks and time lapse movies (Figure A.4 and S3–S6 Movies). Comparable high-quality fluorescence in vivo imaging has previously only been possible using chloretone [58], which, as we show here, is not without negative side effects (Figure A.8 and A.17), or using custom microfluidics [131] and Polydimethylsiloxane (PDMS) chips [158].

Additionally, we showed that linalool enables repeated short-term imaging of the same specimen over the course of days, allowing us to visualize the dynamics of graft development and head regeneration in individuals (Figure A.2Diii and Figure A.5A). We were able to achieve

fluorescent imaging with sub-cellular resolution (Figure A.3), which suggests that one could study cellular migration processes over the course of days. Furthermore, induced mouth opening and induced local body column contraction in linalool treated epithelial GCaMP animals demonstrated that linalool does not interfere with epithelial calcium signaling and that GCaMP animals can be used to study behaviors that are not suppressed by linalool. Therefore, given linalool's lack of toxicity and ease of use, linalool is likely to become a popular tool by making in vivo fluorescence imaging over broad contexts accessible to *Hydra* researchers.

When compared to other currently used anesthetics, 1 mM linalool is superior in terms of ease of preparation, handling, and disposal. Linalool and heptanol are alcohols and supplied as liquids; thus, working solutions are made up within minutes. Because heptanol has a strong smell, however, preparation in the fume hood may be preferred. Urethane and chloretone are powders and therefore the preparation of stock solutions requires more time and safety precautions, such as working in a fume hood. Chloretone also needs to be heated to dissolve. Regarding overall toxicity, linalool is considered non-toxic at the concentrations employed here [159]. Chloretone is also comparably non-toxic at the concentrations used here [160], whereas urethane is a known carcinogen [161–163]. Heptanol is a teratogen [164] and considered to have aquatic toxicity [165], and long-term low-dose exposure causes abnormal patterning phenotypes, such as two-headed animals in freshwater planarians [166]. Thus, linalool provides a clear advantage in terms of ease of use and lack of toxicity.

Linalool also has an advantage in anesthetized animal morphology (Figure A.7A). Animals extend in linalool and in urethane and maintain their shape for at least one hour, facilitating precision cuts and grafting experiments (Figure A.2); in contrast, animals in heptanol or chloretone appear contracted and mis-shapen and change morphology over time (Figure A.7Aii and 7Aiv). As grafting requires precise manipulations that are most easily executed on an evenly extended animal, chloretone and heptanol are suboptimal for such applications. The morphological differences that we observed between the various anesthetics can be important when

choosing an anesthetic for a specific application. The demonstrated lack of cellular damage or other harm to the animal with linalool provides an advantage for repeated imaging or for particularly sensitive experiments.

In terms of long-term applications, we find that a 3-day continuous exposure without media exchange is lethal in urethane within 24 h, partially lethal in chloretone, and harmless in linalool and heptanol. Surviving chloretone and heptanol-treated animals showed normal morphology and pinch response, whereas linalool-treated animals do not. The observed detrimental effect on animal health of urethane may be due to an overly broad mechanism of action that impacts other aspects of the animal's physiology. Urethane has been shown to act in *Hydra* by reversing the sodium polarity across the cell membrane, leading to structural damage [125]. While chloretone has been proposed to act directly on nerves [133], its mechanism of action in *Hydra* remains unclear. It is possible that the gross anatomical changes that are observed in exposure to chloretone cause functional problems that ultimately cause death. Heptanol is a gap junction blocker that effectively blocks ectodermal epithelial cell-cell communication in the body column at 0.04% v/v [134]. As a small alcohol, its effect may be lost over long incubations due to its volatility. Exchanging the media every 24 h drastically changed the outcome of incubation in chloretone and heptanol, with all chloretone-treated and most heptanol-treated animals dying within 3 days. This result suggests that the survival and loss of anesthesia seen in animals incubated 72 h in heptanol or chloretone without medium changes is due to evaporation or degradation of the chemical, and that continuous exposure to active concentrations is toxic to the animals. In summary, these data suggest that urethane, chloretone, and heptanol cannot be used for continuous 3-day exposure and long-term imaging. Thus, for long-term experiments, linalool is the only viable option among the four anesthetics tested.

In contrast to intact polyps, regenerating body columns continuously exposed to 1 mM linalool over 3 days showed abnormal morphology (Figure A.6Eii) and suppressed regeneration (Figure A.6D). Both, head and foot regeneration were delayed (Figure A.6E and A.15). Affected

animals healed their wounds but did not develop the structures associated with the missing body part–decapitated animals mostly did not form tentacles or hypostomes, and animals lacking feet did not regain a peduncle or the ability to adhere to the substrate. A small fraction of animals showed one or two tentacle buds at 3 days of regeneration in 1mM linalool (Figure A.14), whereas some animals died under the same conditions, suggesting sensitivity differences among individuals of the same strain. Regeneration could be rescued by transferring the regenerating animals back to HM after linalool exposure (Figure A.6E). While these findings prevent the use of linalool for continuous long-term imaging of regeneration, they indicate that linalool could potentially be a useful tool for regeneration studies if the mechanism of action can be elucidated.

Because nerve-free animals in linalool do not show delayed regeneration (Figure A.16), these data suggest that nerve or interstitial cells are the target for the regeneration defect. The precise role of the interstitial cell lineage in regeneration and morphogenesis is unknown. Nerve-free *Hydra* are capable of regeneration and budding [167]. Marcum and Campbell propose several possible explanations for this observation– 1. that nerve cells are not involved in development, 2. that nerve cells modulate developmental processes initiated by epithelial cells, 3. that nerve cells play an essential role in patterning but that their absence can be compensated for, or 4. that nerve and epithelial cells both have critical but overlapping roles in development. Head regeneration is delayed in *Hydra* treated with double-stranded RNA from a gene encoding a neuronal progenitor marker [153]. The authors take this result to support the third possibility laid out by Marcum and Campbell–that neurons are critical for regeneration, but that in their complete absence nerve-free animals can employ an alternate pathway. Our finding that linalool strongly suppresses head regeneration in wild type animals while having no effect on nerve-free animals supports this idea that neuronal signals play an important role for head regeneration under normal circumstances. It will be exciting to dissect this relationship between nerve signaling and axial patterning. One possible starting point for investigation is linalool's known

mechanism of action in other systems.

Linalool has been found to inhibit glutamatergic signaling in the central nervous system [168] and to modify nicotinic receptors at neuromuscular junctions in rodents, leading to modulated acetylcholine release [169]. While it is unclear whether the mechanism of anesthesia in *Hydra* is the same as that in rodents, the cellular machinery targeted is sufficiently conserved that this is a possibility. *Hydra* has been shown to possess GABA receptors [170], and to have specific glutamate-binding abilities likely corresponding to at least two types of glutamate receptors [171]. GABA, glutamate, and their agonists and antagonists have been shown to influence behaviors such as contraction bursts [172], as well as nematocyst activity [173]. On the other hand, *Hydra* homogenate was found to contain an enzyme that hydrolyzes acetylcholine [174]. Nicotinic acetylcholinesterase antagonists were found to decrease contraction bursts while a muscarinic acetylcholinergic antagonist increased them [175]. A cDNA sequence for acetylcholinesterase has also been cloned, though its expression and localization have not been confirmed [127]. Thus, the targets of linalool's mechanism of action appear to be conserved between *Hydra* and rodents, though further mechanistic studies will be needed to confirm a shared mode of action.

Finally, because different species are used in *Hydra* research, we also tested the suitability of linalool as a reversible anesthetic in other *Hydra* species – *H. oligactis* and *H. viridissima*. The results for induction and recovery times and effects on pinch and feeding responses are summarized in Figure A.18. We found similar effects as observed for *Hydra vulgaris* (Figure A.18) and conclude that linalool effectively anesthetizes these other *Hydra* species.

In summary, linalool offers a range of advantages over other available anesthetics by enabling new applications such as long term or repeated imaging while also being usable as a pre-fixation relaxant in the same way as current options. Linalool's lack of toxicity to both *Hydra* and researchers and the ease of use and preparation compared to current anesthetics render it an attractive tool for *Hydra* experimentation in the teaching setting. Excitingly, linalool makes

grafting experiments that can provide fundamental insights into regeneration and biological patterning accessible to students with no previous experience with *Hydra*.

A.6 Acknowledgments

A.7 Supplemental Material

A.7.1 Supplemental Figures
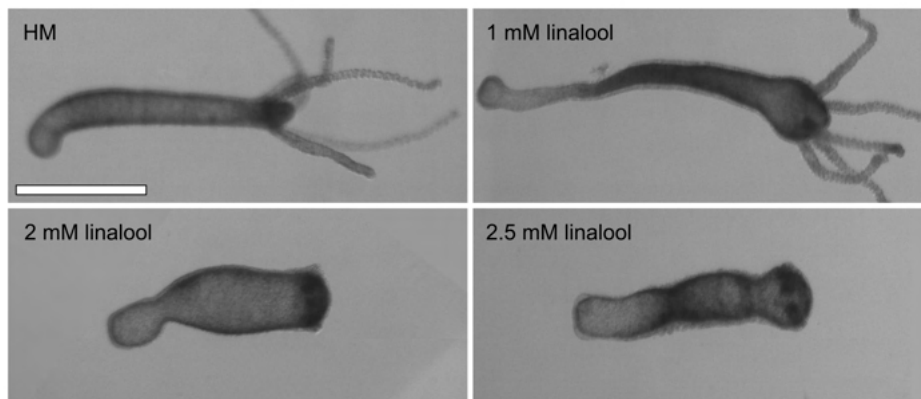
Figure A.9: Abnormal morphology of *Hydra* after 3 h incubation in linalool. Animals are contracted with stubby tentacles in concentrations of 2 mM and 2.5 mM. Images representative of 5/5 animals imaged at the different concentrations. HM denotes Hydra medium control. Scale bar: 1 mm.
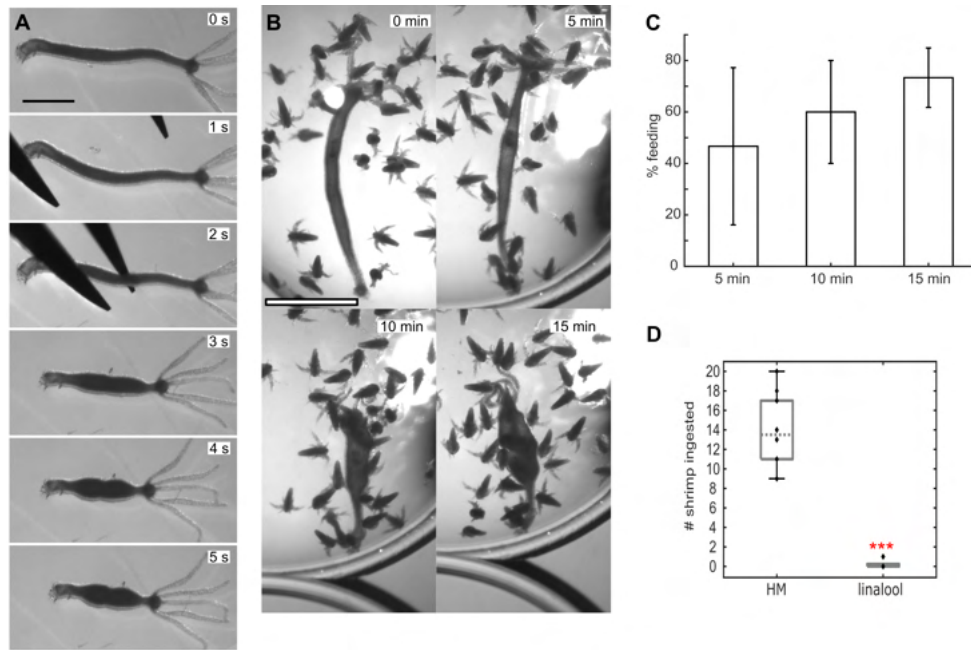
Figure A.10: *Hydra* pinch and feeding responses after recovery from 1 mM linalool. A. Animals display a normal pinch response after 5 min recovery in *Hydra* medium (HM). Image representative of 18/18 polyps across 3 technical replicates. Scale bar: 0.5 mm. B. Feeding after 0, 5, 10, and 15 min recovery in HM. Scale bar: 1 mm. C. Percentage of animals that feed after 5 min (47 $\pm$ 31% (mean $\pm$ SD)), 10 min (60 $\pm$ 20%) and 15 min (73 $\pm$ 12%) recovery in HM (averages over 3 technical replicates with 5 polyps each). Error bars represent SD. D. Median number of shrimp ingested by each animal incubated in HM for 30 minutes was 13 (11, 16; 25th percentile, 75th percentile) for n = 9 polyps across 2 technical replicates. On the other hand, only 2 out of 9 animals (across 2 technical replicates) kept in 1 mM linalool ingested shrimp in the 30 min. Both animals ingested only one shrimp each. (***) denotes statistically significant difference at p < 0.001 (Mann- Whitney U test).
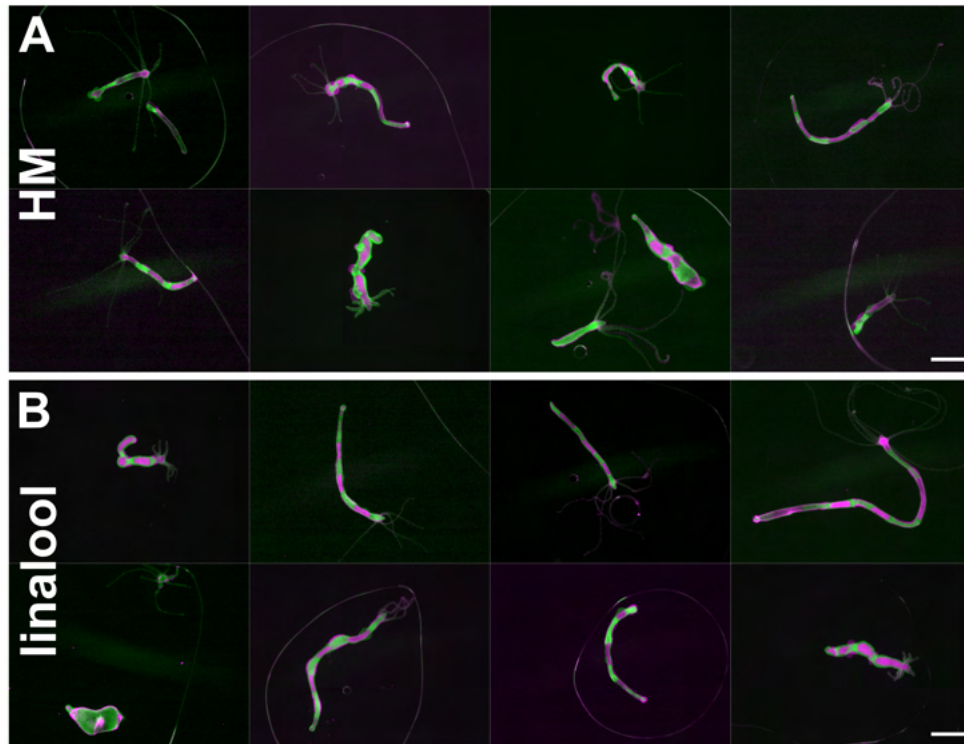
Figure A.11: Linalool improves outcome of zebra grafts. A. Zebra grafts conducted in *Hydra* medium (HM), imaged 24 h after grafting. Scale bar: 1 mm. B. Zebra grafts conducted in 1 mM linalool, imaged 24 h after grafting. Scale bar: 1 mm.
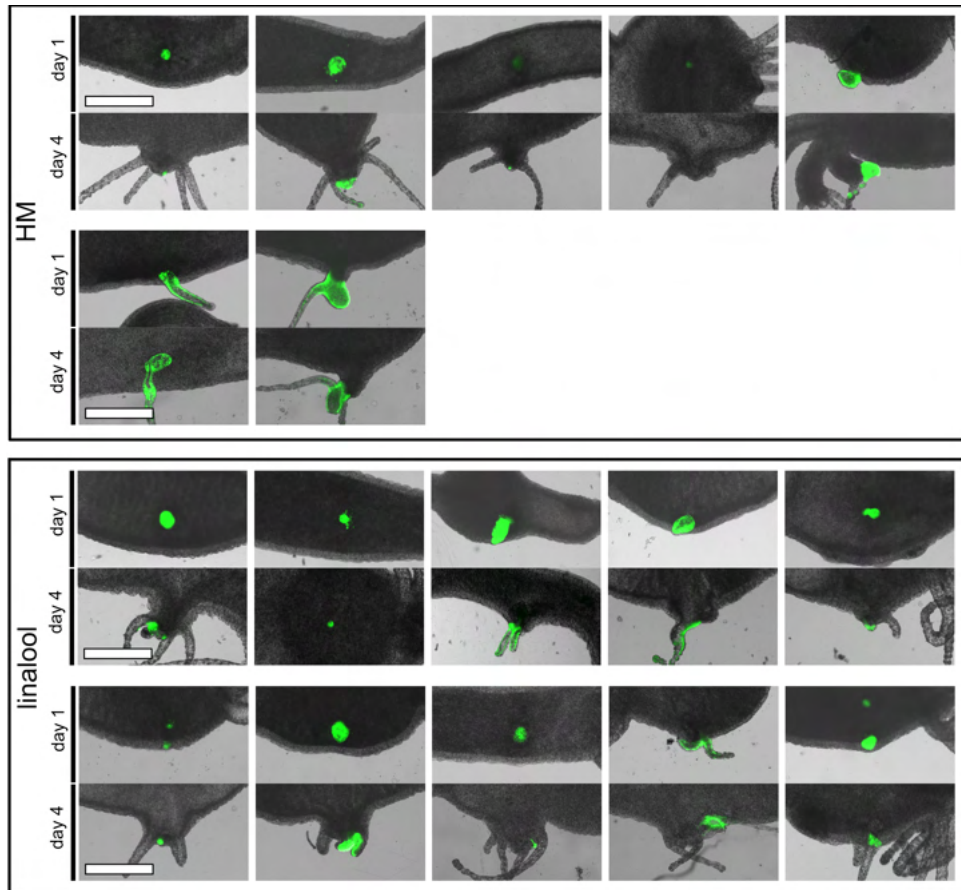
Figure A.12: Hypostome graft morphologies. Animals that retained the grafted tissue or formed an ectopic axis, with grafting performed in either *Hydra* medium (HM) or 1 mM linalool (from n = 17 attempts per condition) are shown. Scale bars: 0.5 mm.
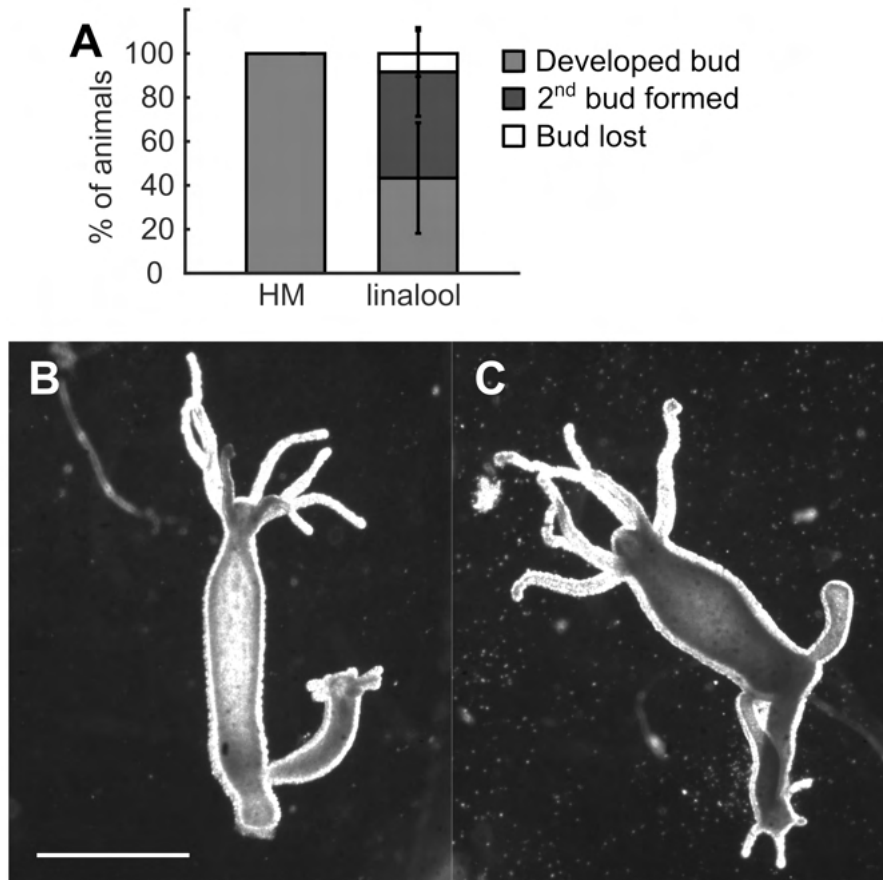
Figure A.13: Linalool does not impact budding rate. A. Bud development in budding animals incubated continuously for 3 days in HM or 1 mM linalool, 30 animals per condition across 3 technical replicates. There was no statistically significant difference between animals in HM and in linalool (2-tailed t-test). Error bars represent SD. B. Representative image of animal with fully developed bud. C. Representative image of animal with two buds. Scale bar: 1 mm.

Figure A.14: Head regeneration in linalool. 14/42 decapitated polyps across 4 technical replicates regenerated small tentacle buds at the end of 3-day incubation in linalool. Linalool solution was changed every day. The remaining animals did not regenerate head structures. Scale bar: 0.5 mm.
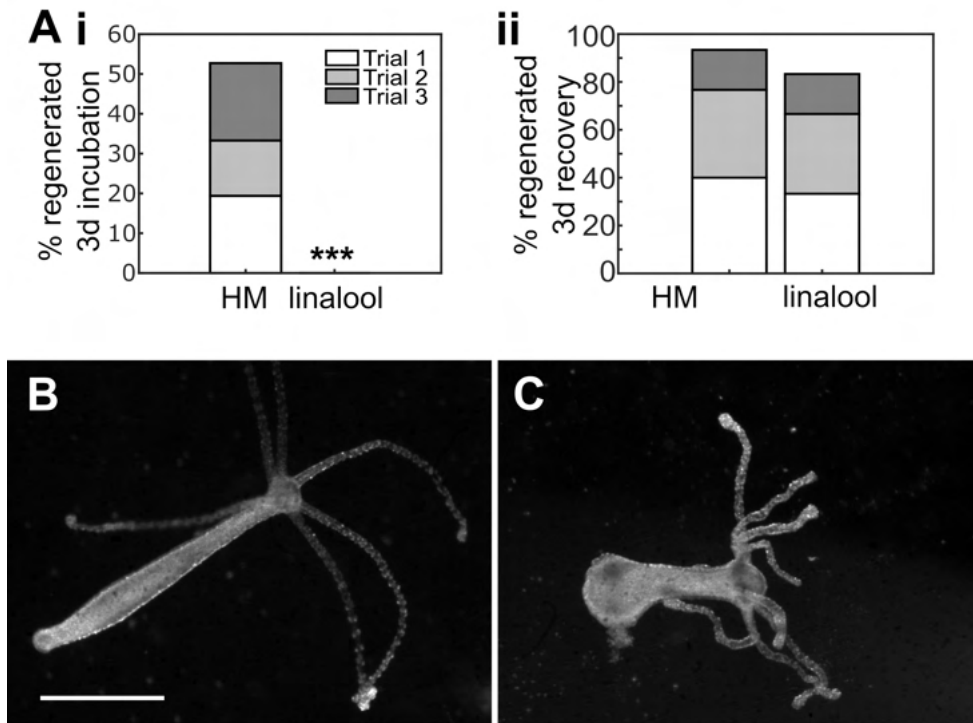
Figure A.15: Linalool inhibits foot regeneration. A. i. Three-day incubation in linalool prevents foot regeneration. Data from 36 polyps per condition across 3 technical replicates. (***) denotes statistically significant difference between percentage of animals with regenerated foot in HM and linalool at $p < 0.001$ (Fisher's exact test) when comparing overall numbers. ii. Phenotype is rescued after 3-day recovery in HM. Data from 30 polyps per condition across 3 technical replicates. B. Polyp incubated 3 days in HM after foot amputation. C. Polyp incubated 3 days in 1 mM linalool after foot amputation. Scale bar: 1 mm.
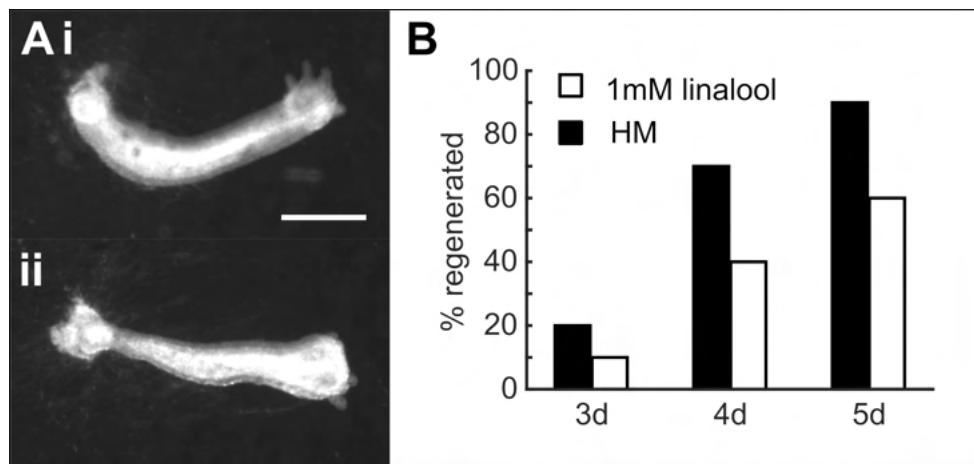
Figure A.16: Head regeneration in nerve-free *Hydra* is not negatively impacted by 5-day incubation in linalool. A. Representative images of nerve-free polyps regenerating their heads in i. HM and ii. linalool after 4-day incubation. Scale bar: 1 mm. B. Percentage of animals with at least one regenerated tentacle over time (n = 10 animals in 2 technical replicates). There is no statistically significant difference between animals regenerating in HM compared to those regenerating in linalool (Fisher's Exact test).
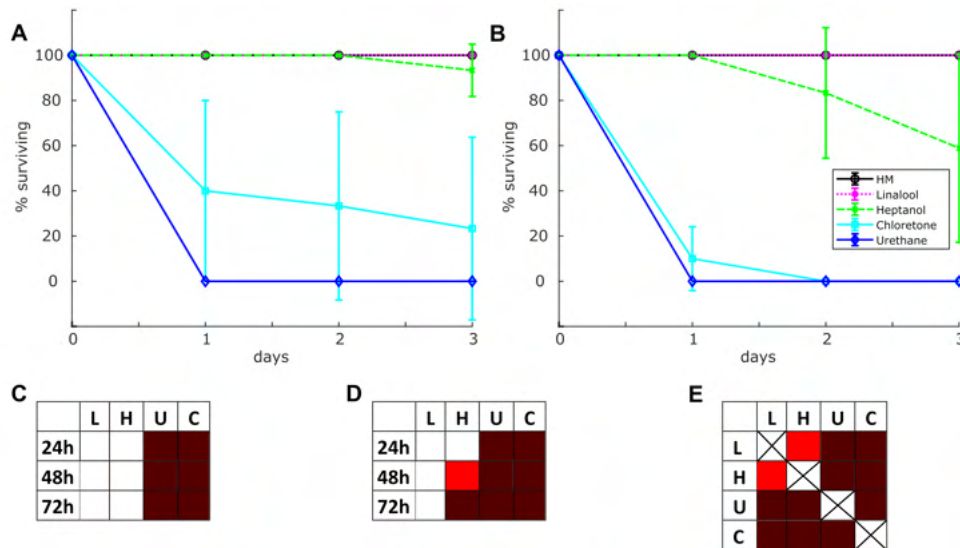
Figure A.17: Lethality of 3-day incubation in various anesthetics. A. Incubation without changing media. n = 20 animals per condition across 3 technical replicates. Surviving heptanol and chloretone animals had a normal pinch response at 3 days. Surviving linalool animals remained anesthetized. B. Incubation with media exchanged every 24 h. n = 22 animals per condition across 3 technical replicates except for linalool and urethane where 2 technical replicates with 5 animals per replicate were performed. C. Statistical comparison of number of surviving animals at each time point in each anesthetic (without media changes) with the HM control as reference (Fisher's Exact test). D. Statistical comparison of number of surviving animals at each time point in each anesthetic (with media changes) with the HM control as reference (Fisher's Exact test). E. Pairwise statistical comparisons of number of animals surviving at the end of the 3-day incubation in the anesthetics (with media changes) (Fisher's Exact test). (C-E) Pink, red and dark red indicate a statistically significant difference at $p<0.05$, $p<0.01$ and $p<0.001$ respectively, determined using the Fisher's Exact test between pairs of anesthetics.
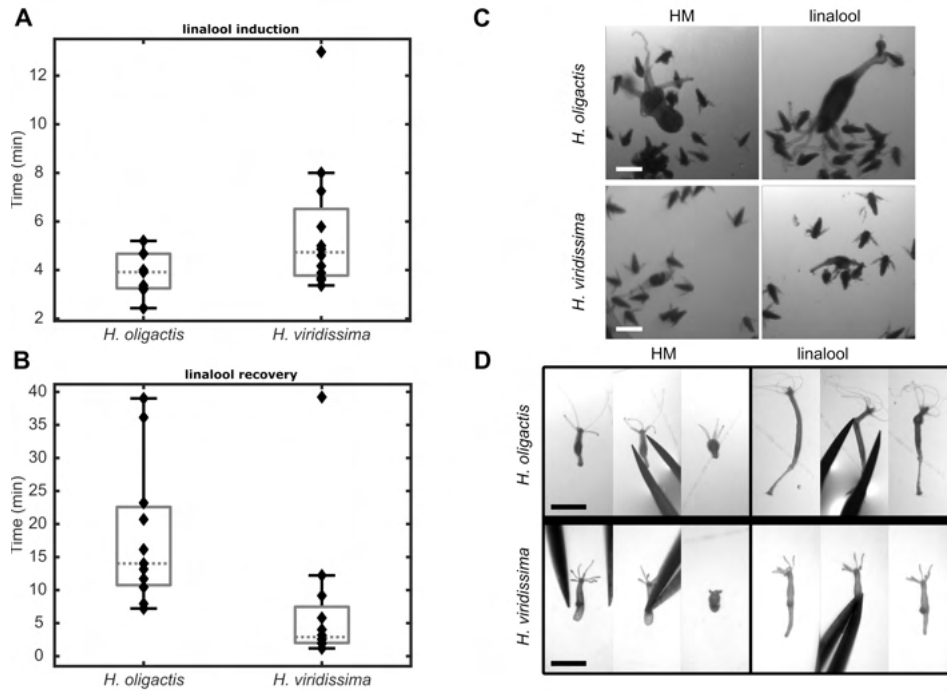
Figure A.18: Response of *H. oligactis* and *H. viridissima* to 1 mM linalool. A. Time for induction of anesthesia, measured as time of full extension after last observed contraction burst, in 1 mM linalool (n = 9 for *H. oligactis* across 3 technical replicates, n = 12 for *H. viridissima* across 3 technical replicates). B. Time for recovery from anesthesia, measured as time of first observed contraction burst, after being moved to HM from 1 mM linalool (n = 11 for *H. oligactis* across 3 technical replicates, n = 12 for *H. viridissima* across 3 technical replicates). C. Feeding assay. Feeding is inhibited due to linalool incubation. While animals in linalool have shrimp stuck to their tentacles, they do not have any in their body column, contrary to what is seen with animals in HM. Scale bar 0.5 mm. D. Pinch responses in HM and 1 mM linalool. Pinch response is inhibited by linalool incubation. Scale bar 1 mm.

A.7.2 Supplemental Movies

Movie file link: https://github.com/tapangoel1994/ThesisMovies.git.

Movie 1. 1 mM linalool prevents pinch response. Time-lapse movie of *Hydra* polyp incubated in either Hydra medium (HM; left) or in 1 mM linalool for 10 minutes (right). Experimental details provided in Methods in main text. Movie is representative of 10/10 animals across 2 technical replicates. Video playback: 1fps. Scale bar: 1 mm.

Movie 2. 1 mM linalool prevents pinch response in nerve-free animals. Time-lapse movie of nerve free Hydra polyp incubated in either Hydra medium (HM; left) or in 1 mM linalool for 10 minutes (right). Experimental details provided in Methods in main text. Movie is representative of 6/6 tested nerve-free animals across 2 technical replicates. Video playback: 1fps. Scale bar: 1 mm.

Movie 3. Linalool incubation allows for low magnification time-lapse imaging. Time-lapse movie of freely moving GCaMP6s animals in either *Hydra* medium (HM; left) or incubated for at least 10 min in 1 mM linalool (LL; right). Experimental details are provided in Methods in the main text and Figure A.3A,Bi-iii shows a Maximum Intensity Projection of the video. Video playback: 10fps. Scale bar: 100 μm.

Movie 4. Linalool allows for high magnification time-lapse imaging. Time-lapse movie showing a z-stack through the body column of a GCaMP6s animal in either *Hydra* medium (HM; left) or incubated for at least 10 min in 1 mM linalool (LL; right). Experimental details are provided in Methods in the main text and Figure A.3A,Biv-v shows a single slice and the Maximum Intensity Projection of the video. Video playback: 10fps. Scale bar: 10 μm.

Movie 5. Linalool treatment allows for multi-channel fluorescence time-lapse imaging. Time-lapse movie of a 3-channel acquisition of a watermelon animal stained with Hoechst nuclear dye. The head was mounted as described in [83] in 1 mM linalool and flushed with 2 mM reduced glutathione to trigger a feeding reaction. While the mouth stays closed during recording, one can clearly see the quality of imaging that can be obtained in linalool,

allowing for simultaneous imaging of cell shapes and nuclear positions. Video playback: 10fps. Scale bar: 100 μm.

Movie 6. Linalool does not interfere with calcium imaging. Time-lapse movie showing calcium activity in epithelial GCaMP animal during chemically induced mouth opening. The head was mounted as described in [83] in 1 mM linalool and flushed with 2 mM reduced glutathione to trigger a feeding reaction. Video playback: 10fps. Scale bar: 100 μm.

Movie 7. Linalool does not sufficiently immobilize polyps for long term imaging. Shown first, an unconstrained animal in *Hydra* medium, which exits the field of view within 90 min of recording. In contrast, it is possible to take a 24 h time lapse movie of an unconstrained *Hydra* in 1 mM linalool. However, while linalool incubation significantly improves stability for imaging, the animal moves too much for experiments requiring cellular resolution. Video playback: 10fps. Scale bar: 0.5 mm.

Movie 8. Calcium activity in response to pinching. Time-lapse movie showing calcium activity in epithelial GCaMP animal in response to pinching. Animal in *Hydra* medium (HM) shows the global contraction accompanied by calcium activity in the entire body column. Animal incubated in linalool only shows calcium activity at the site of pinching. Video playback: 10fps. Scale bar: 1 mm.

Table A.3: Coefficient of variation calculated for t-stacks of GCaMP animals imaged at 4x and z-stacks of GCaMP animals imaged at 60x., (**) indicates statistically significant difference from corresponding imaging in *Hydra* medium at p <0.01 as determined by a two-tailed t-test.

	Hydra Medium		1 mM Linalool	
	4x	60x	4x	60x
	.222	.152	.154	.136
	.168	.199	.145	.149
	.195	.158	.143	.099
	.176	.183	.147	.113
	.163	.268	.139	.144
	.172	.170	.137	.084
	.163		.143	
	.148		.142	
	.202		.127	
	.137		.156	
Mean	.175	.188	.143**	.121**
stdev	.025	.042	.008	.026

Bibliography

1. Thompson, D. W. *On growth and form* 1942nd ed. (Cambrige University Press, 1917).

2. Ball, P. In retrospect: On Growth and Form. *Nature* **494,** 32–33 (Feb. 2013).

3. The 100-year-old challenge to Darwin that is still making waves in research. *Nature* **544,** 138–139 (Apr. 1, 2017).

4. Turing, A. M. The Chemical Basis of Morphogenesis. *Philosophical Transactions of the Royal Society of London. Series B, Biological Sciences* **237,** 37–72 (1952).

5. Farge, E. in *Current Topics in Developmental Biology* (ed Labouesse, M.) 243–265 (Academic Press, Jan. 1, 2011).

6. Goodwin, K. & Nelson, C. M. Mechanics of Development. *Developmental Cell* **56,** 240–250 (Jan. 25, 2021).

7. Wong, K. C. L., Summers, R. M., Kebebew, E. & Yao, J. Tumor growth prediction with reaction-diffusion and hyperelastic biomechanical model by physiological data fusion. *Medical Image Analysis* **25,** 72–85 (Oct. 1, 2015).

8. Abler, D., Rockne, R. C. & Büchler, P. in *New Developments on Computational Methods and Imaging in Biomechanics and Biomedical Engineering* (eds Tavares, J. M. R. S. & Fernandes, P. R.) 37–48 (Springer International Publishing, Cham, 2019).

9. Ben Isaac, E., Manor, U., Kachar, B., Yochelis, A. & Gov, N. S. Linking actin networks and cell membrane via a reaction-diffusion-elastic description of nonlinear filopodia initiation. *Physical Review E* **88,** 022718 (Aug. 29, 2013).

10. Keldermann, R. H., Nash, M. P. & Panfilov, A. V. Modeling cardiac mechano-electrical feedback using reaction-diffusion-mechanics systems. *Physica D: Nonlinear Phenomena. Nonlinear Waves in Excitable Media: Approaches to Cardiac Arrhythmias* **238,** 1000–1007 (June 1, 2009).

11. Mercker, M., Marciniak-Czochra, A., Richter, T. & Hartmann, D. Modeling and Computing of Deformation Dynamics of Inhomogeneous Biological Surfaces. *SIAM Journal on Applied Mathematics* **73,** 1768–1792 (Jan. 2013).

12. Bays, J. L., Campbell, H. K., Heidema, C., Sebbagh, M. & DeMali, K. A. Linking E-cadherin mechanotransduction to cell metabolism through force-mediated activation of AMPK. *Nature Cell Biology* **19,** 724–731 (June 2017).

13. Carter, J. A., Lind, C. H., Truong, M. P. & Collins, E.-M. S. To Each His Own. *Journal of Statistical Physics* **161,** 250–272 (Oct. 1, 2015).

14. Arnold, C. P. *et al.* Hox genes regulate asexual reproductive behavior and tissue segmentation in adult animals. *bioRxiv,* 2021.01.24.427972 (Jan. 1, 2021).

15. Arnold, C. P., Benham-Pyle, B. W., Lange, J. J., Wood, C. J. & Sánchez Alvarado, A. Wnt and TGFβ coordinate growth and patterning to regulate size-dependent behaviour. *Nature* **572,** 655–659 (Aug. 2019).

16. Herath, S. & Lobo, D. Cross-inhibition of Turing patterns explains the self-organized regulatory mechanism of planarian fission. *Journal of Theoretical Biology* **485,** 110042–110042 (Jan. 2020).

17. Goel, T. *et al.* Let it rip: the mechanics of self-bisection in asexual planarians determines their population reproductive strategies. *Physical Biology* **19,** 016002 (Nov. 2021).

18. Wang, R. On the mechanisms of axis specification in Hydra (2021).

19. Mercker, M., Köthe, A. & Marciniak-Czochra, A. Mechanochemical Symmetry Breaking in Hydra Aggregates. *Biophysical Journal* **108,** 2396–2407 (May 5, 2015).

20. Nakamura, Y., Tsiairis, C. D., Ozbek, S. & Holstein, T. W. Autoregulatory and repressive inputs localize Hydra Wnt3 to the head organizer. *Proceedings of the National Academy of Sciences* **108,** 9137–9142 (May 31, 2011).

21. Gierer, A. & Meinhardt, H. A theory of biological pattern formation. *Kybernetik* **12,** 30–39 (Dec. 1972).

22. Wang, H. *et al. From neuron to muscle to movement: a complete biomechanical model of Hydra contractile behaviors* (bioRxiv, Dec. 15, 2020), 2020.12.14.422784.

23. Goel, T., Wang, R., Martin, S., Lanphear, E. & Collins, E.-M. S. Linalool acts as a fast and reversible anesthetic in Hydra. *PLOS ONE* **14,** e0224221 (Oct. 24, 2019).

24. *Planarian regeneration: methods and protocols* (ed Rink, J. C.) *Methods in molecular biology* **1774** (Humana Press, New York, NY, 2018). 573 pp.

25. Cebrià, F. Planarian Body-Wall Muscle: Regeneration and Function beyond a Simple Skeletal Support. *Frontiers in Cell and Developmental Biology* **4,** 8 (2016).

26. Hirshfeld, A. *The electric life of Michael Faraday* 258 pp. (Walker, New York, 2006).

27. Quinodoz, S., Thomas, M. A., Dunkel, J. & Schötz, E.-M. The More the Merrier?: Entropy and Statistics of Asexual Reproduction in Freshwater Planarians. *Journal of Statistical Physics* **142,** 1324–1336 (Apr. 2011).

28. Dunkel, J., Talbot, J. & Schötz, E.-M. Memory and obesity affect the population dynamics of asexual freshwater planarians. *Physical Biology* **8,** 026003 (Apr. 2011).

29. Thomas, M. A., Quinodoz, S. & Schötz, E.-M. Size Matters!: Birth Size and a Size-Independent Stochastic Term Determine Asexual Reproduction Dynamics in Freshwater Planarians. *Journal of Statistical Physics* **148,** 664–676 (Sept. 2012).

30. Yang, X., Kaj, K. J., Schwab, D. J. & Collins, E. M. S. Coordination of size-control, reproduction and generational memory in freshwater planarians. *Physical Biology* **14** (2017).

31. Davison, J. Population Growth in Planaria Dugesia tigrina (Gerard) : Regulation by the absolute number in the population. *Journal of General Physiology* **61,** 767–785 (June 1, 1973).

32. Malinowski, P. T. *et al.* Mechanics dictate where and how freshwater planarians fission. *Proceedings of the National Academy of Sciences* **114,** 10888–10893 (Oct. 2017).

33. Cebrià, F. & Newmark, P. A. Planarian homologs of netrin and netrin receptor are required for proper regeneration of the central nervous system and the maintenance of nervous system architecture. *Development* **132,** 3691–3703 (Aug. 15, 2005).

34. Morita, M. & Best, J. B. Effects of photoperiods and melatonin on planarian asexual reproduction. *Journal of Experimental Zoology* **231,** 273–282 (1984).

35. Best, J. B., Goodman, A. B. & Pigon, A. Fissioning in Planarians: Control by the Brain. *Science* **164,** 565–566 (May 2, 1969).

36. Pigon, A., Morita, M. & Best, J. B. Localization and identification of the receptors by electron micrographic and ablation studies. *Journal of Neurobiology* **5,** 443–462 (1974).

37. Best, J. B., Abelein, M., Kreutzer, E. & Pigon, A. Cephalic mechanism for social control of fissioning in planarians: III. Central nervous system centers of facilitation and inhibition. *Journal of Comparative and Physiological Psychology* **89,** 923–932 (1975).

38. Best, J. B. & Morita, M. Planarians as a model system for in vitro teratogenesis studies. *Teratogenesis, Carcinogenesis, and Mutagenesis* **2,** 277–291 (1982).

39. Stowell, N. C., Goel, T., Shetty, V., Noveral, J. & Collins, E.-M. S. Quantifying Planarian Behavior as an Introduction to Object Tracking and Signal Processing. *The Biophysicist* (Apr. 27, 2021).

40. Schindelin, J. *et al.* Fiji: an open-source platform for biological-image analysis. *Nature Methods* **9,** 676–682 (July 2012).

41. Ireland, D. *et al.* Dugesia japonica is the best suited of three planarian species for high-throughput toxicology screening. *Chemosphere* **253,** 126718 (Aug. 1, 2020).

42. Cochet-Escartin, O., Mickolajczyk, K. J. & Collins, E.-M. S. Scrunching: a novel escape gait in planarians. *Physical Biology* **12,** 056010 (Sept. 10, 2015).

43. Sikes, J. M. & Bely, A. E. Radical modification of the A-P axis and the evolution of asexual reproduction in Convolutriloba acoels. *Evolution & Development* **10,** 619–631 (Oct. 2008).

44. Mead, R. W. Proportioning and regeneration in fissioned and unfissioned individuals of the planarian Dugesia tigrina. *Journal of Experimental Zoology* **235,** 45–54 (1985).

45. Sheiman, I. M., Sedel'nikov, Z. V., Shkutin, M. F. & Kreshchenko, N. D. Asexual reproduction of planarians: Metric studies. *Russian Journal of Developmental Biology* **37,** 102–107 (Mar. 1, 2006).

46. Hagstrom, D. *et al.* Planarian cholinesterase: molecular and functional characterization of an evolutionarily ancient enzyme to study organophosphorus pesticide toxicity. *Archives of Toxicology* **92,** 1161–1176 (Mar. 1, 2018).

47. Stückemann, T. *et al.* Antagonistic Self-Organizing Patterning Systems Control Maintenance and Regeneration of the Anteroposterior Axis in Planarians. *Developmental Cell* **40,** 248–263.e4 (Feb. 6, 2017).

48. Marsal, M., Pineda, D. & Saló, E. Gtwnt-5 a member of the wnt family expressed in a subpopulation of the nervous system of the planarian Girardia tigrina. *Gene expression patterns: GEP* **3,** 489–495 (Aug. 2003).

49. Yazawa, S., Umesono, Y., Hayashi, T., Tarui, H. & Agata, K. Planarian Hedgehog/Patched establishes anterior-posterior polarity by regulating Wnt signaling. *Proceedings of the National Academy of Sciences of the United States of America* **106,** 22329–22334 (Dec. 29, 2009).

50. Umesono, Y. *et al.* The molecular logic for planarian regeneration along the anterior–posterior axis. *Nature* **500,** 73–76 (Aug. 2013).

51. Witchley, J. N., Mayer, M., Wagner, D. E., Owen, J. H. & Reddien, P. W. Muscle Cells Provide Instructions for Planarian Regeneration. *Cell reports* **4,** 633–641 (Aug. 29, 2013).

52. Bueno, D., Fernàndez-Rodríguez, J., Cardona, A., Hernàndez-Hernàndez, V. & Romero, R. A novel invertebrate trophic factor related to invertebrate neurotrophins is involved in planarian body regional survival and asexual reproduction. *Developmental Biology* **252,** 188–201 (Dec. 15, 2002).

53. West, D. L. The epitheliomuscular cell of hydra: Its fine structure, three-dimensional architecture and relation to morphogenesis. *Tissue and Cell* **10,** 629–646 (Jan. 1, 1978).

54. Galliot, B. The Hydra Model System. *International Journal of Developmental Biology* **56,** 407–409 (July 20, 2012).

55. Chapman, J. A. *et al.* The dynamic genome of Hydra. *Nature* **464,** 592–596 (Mar. 25, 2010).

56. Juliano, C. E., Lin, H. & Steele, R. E. Generation of transgenic Hydra by embryo microinjection. *Journal of Visualized Experiments: JoVE,* 51888 (Sept. 11, 2014).

57. Glauber, K. M. *et al.* A small molecule screen identifies a novel compound that induces a homeotic transformation in Hydra. *Development* **140,** 4788–4796 (Dec. 1, 2013).

58. Lommel, M., Tursch, A., Rustarazo-Calvo, L., Trageser, B. & Holstein, T. W. *Genetic knockdown and knockout approaches in Hydra* (Dec. 7, 2017), 230300.

59. Shimizu, H., Sawada, Y. & Sugiyama, T. Minimum Tissue Size Required for Hydra Regeneration. *Developmental Biology* **155,** 287–296 (Feb. 1993).

60. Kücken, M., Soriano, J., Pullarkat, P. A., Ott, A. & Nicola, E. M. An Osmoregulatory Basis for Shape Oscillations in Regenerating Hydra. *Biophysical Journal* **95,** 978–985 (July 15, 2008).

61. Fütterer, C., Colombo, C., Jülicher, F. & Ott, A. Morphogenetic oscillations during symmetry breaking of regenerating Hydra vulgaris cells. *Europhysics Letters* **64,** 137 (Oct. 1, 2003).

62. Sato-Maeda, M. & Tashiro, H. Development of Oriented Motion in Regenerating Hydra Cell Aggregates. *Zoological Science* **16,** 327–334 (Apr. 1999).

63. Benos, D. J., Kirk, R. G., Barba, W. P. & Goldner, M. M. Hyposmotic fluid formation in Hydra. *Tissue & Cell* **9,** 11–22 (1977).

64. Soriano, J., Rüdiger, S., Pullarkat, P. & Ott, A. Mechanogenetic Coupling of Hydra Symmetry Breaking and Driven Turing Instability Model. *Biophysical Journal* **96,** 1649–1660 (Feb. 18, 2009).

65. Hobmayer, B. *et al.* WNT signalling molecules act in axis formation in the diploblastic metazoan Hydra. *Nature* **407,** 186–189 (Sept. 2000).

66. Livshits, A., Shani-Zerbib, L., Maroudas-Sacks, Y., Braun, E. & Keren, K. Structural Inheritance of the Actin Cytoskeletal Organization Determines the Body Axis in Regenerating Hydra. *Cell Reports* **18,** 1410–1421 (Feb. 7, 2017).

67. Gamba, A., Nicodemi, M., Soriano, J. & Ott, A. Critical Behavior and Axis Defining Symmetry Breaking in Hydra Embryonic Development. *Physical Review Letters* **108,** 158103 (Apr. 10, 2012).

68. Soriano, J., Colombo, C. & Ott, A. Hydra Molecular Network Reaches Criticality at the Symmetry-Breaking Axis-Defining Moment. *Physical Review Letters* **97,** 258102 (Dec. 18, 2006).

69. Brunet, T. *et al.* Evolutionary conservation of early mesoderm specification by mechanotransduction in Bilateria. *Nature Communications* **4,** 2821 (Nov. 27, 2013).

70. Broun, M., Gee, L., Reinhardt, B. & Bode, H. R. Formation of the head organizer in hydra involves the canonical Wnt pathway. *Development* **132,** 2907–2916 (June 15, 2005).

71. Bode, H. Axis Formation in Hydra. *Annual Review of Genetics* **45,** 105–117 (2011).

72. Lengfeld, T. *et al.* Multiple Wnts are involved in Hydra organizer formation and regeneration. *Developmental Biology* **330,** 186–199 (June 1, 2009).

73. Shimizu, H., Koizumi, O. & Fujisawa, T. Three digestive movements in Hydra regulated by the diffuse nerve net in the body column. *Journal of Comparative Physiology A* **190,** 623–630 (Aug. 1, 2004).

74. Lenhoff, H. M. & Brown, R. D. Mass culture of hydra: an improved method and its application to other aquatic invertebrates. *Laboratory Animals* **4,** 139–154 (Apr. 1, 1970).

75. Tran, C. M., Fu, S., Rowe, T. & Collins, E.-M. S. Generation and Long-term Maintenance of Nerve-free Hydra. *JoVE (Journal of Visualized Experiments),* e56115 (July 7, 2017).

76. Sugiyama, T. & Fujisawa, T. Genetic analysis of developmental mechanisms in Hydra. II. Isolation and characterization of an interstitial cell-deficient strain. *Journal of Cell Science* **29,** 35–52 (Feb. 1, 1978).

77. Fujisawa, T. Hydra regeneration and epitheliopeptides. *Developmental Dynamics* **226,** 182–189 (2003).

78. Culp, P., Nusslein-Volhard, C. & Hopkins, N. High-frequency germ-line transmission of plasmid DNA sequences injected into fertilized zebrafish eggs. *Proceedings of the National Academy of Sciences* **88,** 7953–7957 (Sept. 15, 1991).

79. Veschgini, M. *et al.* Tracking mechanical and morphological dynamics of regenerating Hydra tissue fragments using a two fingered micro-robotic hand. *Applied Physics Letters* **108,** 103702 (Mar. 7, 2016).

80. Buzgariu, W., Al Haddad, S., Tomczyk, S., Wenger, Y. & Galliot, B. Multi-functionality and plasticity characterize epithelial cells in Hydra. *Tissue Barriers* **3,** 1–13 (2015).

81. Benos, D. J. & Prusch, R. D. Osmoregulation in fresh-water Hydra. *Comparative Biochemistry and Physiology Part A: Physiology* **43,** 165–171 (Sept. 1972).

82. Benos, D. J. & Prusch, R. D. Osmoregulation in Hydra: Column contraction as a function of external osmolality. *Comparative Biochemistry and Physiology – Part A: Physiology* **44,** 1397–1400 (Apr. 1973).

83. Carter, J. A., Hyland, C., Steele, R. E. & Collins, E.-M. S. Dynamics of Mouth Opening in Hydra. *Biophysical Journal* **110,** 1191–1201 (Mar. 8, 2016).

84. Wood, R. L. The fine structure of the hypostome and mouth of hydra, 20.

85. Shimizu, H., Takaku, Y., Zhang, X. & Fujisawa, T. The aboral pore of hydra: evidence that the digestive tract of hydra is a tube not a sac. *Development Genes and Evolution* **217,** 563–568 (Aug. 1, 2007).

86. Bode, H. *et al.* Quantitative analysis of cell types during growth and morphogenesis in Hydra. *Wilhelm Roux' Archiv Fur Entwicklungsmechanik Der Organismen* **171,** 269–285 (Dec. 1973).

87. Lenhoff, H. M. Activation of the Feeding Reflex in Hydra littoralis : I. Role played by reduced glutathione, and quantitative assay of the feeding reflex. *Journal of General Physiology* **45,** 331–344 (Nov. 1, 1961).

88. Forrest, H. Lack of dependence of the feeding reaction in hydra on reduced glutathione. *The Biological Bulletin* **122,** 343–361 (June 1, 1962).

89. Campbell, R. D., Josephson, R. K., Schwab, W. E. & Rushforth, N. B. Excitability of nerve-free hydra. *Nature* **262,** 388–390 (July 1976).

90. Bode, H. R. The interstitial cell lineage of hydra: a stem cell system that arose early in evolution. *Journal of cell science* **109,** 1155–64 (June 1996).

91. Vedula, S. R. K. *et al.* Quantifying Forces Mediated by Integral Tight Junction Proteins in Cell–Cell Adhesion. *Experimental Mechanics* **49,** 3–9 (Feb. 1, 2009).

92. Alberts, B. *et al. Molecular Biology of the Cell* 4th (Garland Science, 2002).

93. Nerurkar, N. L., Mahadevan, L. & Tabin, C. J. BMP signaling controls buckling forces to modulate looping morphogenesis of the gut. *Proceedings of the National Academy of Sciences of the United States of America* **114,** 2277–2282 (Feb. 2017).

94. Höhn, S., Honerkamp-Smith, A. R., Haas, P. A., Trong, P. K. & Goldstein, R. E. Dynamics of a Volvox Embryo Turning Itself Inside Out. *Physical Review Letters* **114,** 178101 (Apr. 27, 2015).

95. Harris, A. R. *et al.* Characterizing the mechanics of cultured cell monolayers. *Proceedings of the National Academy of Sciences* **109,** 16449–16454 (Oct. 9, 2012).

96. Armon, S., Bull, M. S., Aranda-Diaz, A. & Prakash, M. Ultrafast epithelial contractions provide insights into contraction speed limits and tissue integrity. *Proceedings of the National Academy of Sciences of the United States of America* **115,** E10333–E10341 (Oct. 2018).

97. Dupre, C. & Yuste, R. Non-overlapping Neural Networks in Hydra vulgaris. *Current biology: CB* **27,** 1085–1097 (Apr. 24, 2017).

98. Szymanski, J. R. & Yuste, R. Mapping the Whole-Body Muscle Activity of Hydra vulgaris. *Current biology: CB* **29,** 1807–1817.e3 (June 3, 2019).

99. Wood, R. L. The fine structure of the hypostome and mouth of hydra - II. Transmission electron microscopy. *Cell and Tissue Research* **199,** 319–338 (June 1979).

100. Wang, R. *et al.* Mouth Function Determines the Shape Oscillation Pattern in Regenerating Hydra Tissue Spheres. *Biophysical Journal* **117,** 1145–1155 (Sept. 17, 2019).

101. Lenhoff, S. G. & Lenhoff, H. M. *Hydra and the Birth of Experimental Biology - 1744* 192 pp. (1986).

102. Campbell, R. D. & David, C. N. Cell cycle kinetics and development of Hydra attenuata. II. Interstitial cells. *Journal of Cell Science* **16,** 349–358 (Nov. 1974).

103. GIERER, A. *et al.* Regeneration of Hydra from Reaggregated Cells. *Nature New Biology* **239,** 98–101 (Sept. 1972).

104. Steele, R. E. Developmental Signaling in Hydra: What Does It Take to Build a "Simple" Animal? *Developmental Biology* **248,** 199–219 (Aug. 15, 2002).

105. David, C. N. & Murphy, S. Characterization of interstitial stem cells in hydra by cloning. *Developmental Biology* **58,** 372–383 (July 15, 1977).

106. Bosch, T. C. G. Hydra and the evolution of stem cells. *BioEssays* **31,** 478–486 (2009).

107. Bosch, T. C. G. Why polyps regenerate and we don't: Towards a cellular and molecular framework for Hydra regeneration. *Developmental Biology* **303,** 421–433 (Mar. 15, 2007).

108. Galliot, B., Buzgariu, W., Schenkelaars, Q. & Wenger, Y. Non-developmental dimensions of adult regeneration in Hydra. *The International Journal of Developmental Biology* **62,** 373–381 (2018).

109. Cochet-Escartin, O., Locke, T. T., Shi, W. H., Steele, R. E. & Collins, E.-M. S. Physical Mechanisms Driving Cell Sorting in Hydra. *Biophysical Journal* **113,** 2827–2841 (Dec. 19, 2017).

110. Petersen, H. O. *et al.* A Comprehensive Transcriptomic and Proteomic Analysis of Hydra Head Regeneration. *Molecular Biology and Evolution* **32,** 1928–1947 (Aug. 2015).

111. Burnett, A. L. & Diehl, N. A. THE NERVOUS SYSTEM OF HYDRA. I. TYPES, DISTRIBU-TION AND ORIGIN OF NERVE ELEMENTS. *The Journal of Experimental Zoology* **157,** 217–226 (Nov. 1964).

112. David, C. N. A quantitative method for maceration of hydra tissue. *Wilhelm Roux' Archiv Fur Entwicklungsmechanik Der Organismen* **171,** 259–268 (Dec. 1973).

113. Noro, Y. *et al.* Regionalized nervous system in Hydra and the mechanism of its development. *Gene expression patterns: GEP* **31,** 42–59 (Jan. 2019).

114. Koizumi, O. & Koizumi, O. Developmental neurobiology of hydra, a model animal of cnidarians 1 Introduction to the nerve net of hydra: unique features of the diffuse nervous system. *Can. J. Zool* **80,** 1678–1689 (2002).

115. Han, S., Taralova, E., Dupre, C. & Yuste, R. Comprehensive machine learning analysis of Hydra behavior reveals a stable basal behavioral repertoire. *eLife* **7,** e32605 (Mar. 28, 2018).

116. Ando, H., Sawada, Y., Shimizu, H. & Sugiyama, T. Pattern formation in hydra tissue without developmental gradients. *Developmental Biology* **133,** 405–414 (June 1989).

117. Browne, E. N. The production of new hydranths in Hydra by the insertion of small grafts. *Journal of Experimental Zoology* **7,** 1–23 (Aug. 1909).

118. Yao, T. Studies on the Organizer Problem in Pelmatohydra Oligactis: I. The Induction Potency of the Implants and the Nature of the Induced Hydranth. *Journal of experimental Biology* **21,** 147–150 (Aug. 1945).

119. Bode, H. R. The head organizer in Hydra. *The International Journal of Developmental Biology* **56,** 473–478 (2012).

120. MacWilliams, H. K. Hydra transplantation phenomena and the mechanism of Hydra head regeneration. II. Properties of the head activation. *Developmental Biology* **96,** 239–257 (Mar. 1983).

121. Technau, U. *et al.* Parameters of self-organization in Hydra aggregates. *Proceedings of the National Academy of Sciences of the United States of America* **97,** 12127–12131 (Oct. 24, 2000).

122. Siebert, S. *et al.* Stem cell differentiation trajectories in Hydra resolved at single-cell resolution. *bioRxiv,* 460154–460154 (Nov. 2018).

123. Wittlieb, J., Khalturin, K., Lohmann, J. U., Anton-Erxleben, F. & Bosch, T. C. G. Transgenic Hydra allow in vivo tracking of individual stem cells during morphogenesis. *Proceedings of the National Academy of Sciences of the United States of America* **103,** 6208–6211 (Apr. 18, 2006).

124. Rushforth, N. B., Burnett, A. L. & Maynard, R. Behavior in Hydra: Contraction Responses of Hydra pirardi to Mechanical and Light Stimuli. *Science* (Feb. 22, 1963).

125. Macklin, M. The effect of urethan on hydra. *The Biological bulletin* **150,** 442–52 (June 1976).

126. Münder, S. *et al.* Notch-signalling is required for head regeneration and tentacle patterning in Hydra. *Developmental Biology* **383,** 146–157 (Nov. 1, 2013).

127. Takahashi, T. & Hamaue, N. Molecular characterization of Hydra acetylcholinesterase and its catalytic activity. *FEBS letters* **584,** 511–516 (Feb. 5, 2010).

128. Buzgariu, W., Wenger, Y., Tcaciuc, N., Catunda-Lemos, A.-P. & Galliot, B. Impact of cycling cells and cell cycle regulation on Hydra regeneration. *Developmental Biology* **433,** 240–253 (Jan. 15, 2018).

129. Smith, K. M., Gee, L. & Bode, H. R. HyAlx, an aristaless-related gene, is involved in tentacle formation in Hydra. *Development* **127,** 4743–4752 (Nov. 2000).

130. Rentzsch, F., Hobmayer, B. & Holstein, T. W. Glycogen synthase kinase 3 has a proapoptotic function in Hydra gametogenesis. *Developmental Biology* **278,** 1–12 (Feb. 1, 2005).

131. Badhiwala, K. N., Gonzales, D. L., Vercosa, D. G., Avants, B. W. & Robinson, J. T. Microfluidics for electrophysiology, imaging, and behavioral analysis of Hydra. *Lab on a Chip* **18,** 2523–2539 (Aug. 21, 2018).

132. Loomis, W. F. Glutathione Control of the Specific Feeding Reactions of Hydra. *Annals of the New York Academy of Sciences* **62,** 211–227 (1955).

133. Kepner, W. A. & Hopkins, D. L. Reactions of Hydra to chloretone. *Journal of Experimental Zoology* **38,** 437–448 (1924).

134. Takaku, Y. *et al.* Innexin gap junctions in nerve cells coordinate spontaneous contractile behavior in Hydra polyps. *Scientific Reports* **4,** 3573 (Jan. 7, 2014).

135. Aprotosoaie, A. C., Hăncianu, M., Costache, I.-I. & Miron, A. Linalool: a review on a key odorant molecule with valuable biological properties. *Flavour and Fragrance Journal* **29,** 193–219 (2014).

136. Linck, V. M. *et al.* Inhaled linalool-induced sedation in mice. *Phytomedicine: International Journal of Phytotherapy and Phytopharmacology* **16,** 303–307 (Apr. 2009).

137. Heldwein, C. G. *et al.* S-(+)-Linalool from Lippia alba: sedative and anesthetic for silver catfish (Rhamdia quelen). *Veterinary Anaesthesia and Analgesia* **41,** 621–629 (Nov. 2014).

138. Boothe, T. *et al.* A tunable refractive index matching medium for live imaging cells, tissues and model organisms. *eLife* **6** (ed Waterman, C. M.) e27240 (July 14, 2017).

139. Höferl, M., Krist, S. & Buchbauer, G. Chirality influences the effects of linalool on physiological parameters of stress. *Planta Medica* **72,** 1188–1192 (Oct. 2006).

140. Rodenak-Kladniew, B. *et al.* Linalool induces cell cycle arrest and apoptosis in HepG2 cells through oxidative stress generation and modulation of Ras/MAPK and Akt/mTOR pathways. *Life Sciences* **199,** 48–59 (Apr. 15, 2018).

141. Martin, V. J., Littlefield, C. L., Archer, W. E. & Bode, H. R. Embryogenesis in Hydra. *The Biological Bulletin* **192,** 345–363 (June 1, 1997).

142. Technau, U., Miller, M. A., Bridge, D. & Steele, R. E. Arrested apoptosis of nurse cells during Hydra oogenesis and embryogenesis. *Developmental Biology* **260,** 191–206 (Aug. 1, 2003).

143. Hagstrom, D., Cochet-Escartin, O., Zhang, S., Khuu, C. & Collins, E.-M. S. Freshwater Planarians as an Alternative Animal Model for Neurotoxicology. *Toxicological Sciences: An Official Journal of the Society of Toxicology* **147,** 270–285 (Sept. 2015).

144. Thévenaz, P., Ruttimann, U. E. & Unser, M. A pyramid approach to subpixel registration based on intensity. *IEEE transactions on image processing: a publication of the IEEE Signal Processing Society* **7,** 27–41 (1998).

145. Otto, J. J. & Campbell, R. D. Budding in Hydra attenuata: bud stages and fate map. *The Journal of Experimental Zoology* **200,** 417–428 (June 1977).

146. Cikala, M., Wilm, B., Hobmayer, E., Böttger, A. & David, C. N. Identification of caspases and apoptosis in the simple metazoan Hydra. *Current biology: CB* **9,** 959–962 (Sept. 9, 1999).

147. Kanaya, H. J., Kobayakawa, Y. & Itoh, T. Q. Hydra vulgaris exhibits day-night variation in behavior and gene expression levels. *Zoological Letters* **5,** 1–12 (2019).

148. McLaughlin, S. Evidence that polycystins are involved in Hydra cnidocyte discharge. *Invertebrate neuroscience: IN* **17,** 1 (Mar. 2017).

149. Shimizu, H. & Sawada, Y. Transplantation phenomena in hydra: Cooperation of position-dependent and structure-dependent factors determines the transplantation result. *Developmental Biology* **122,** 113–119 (July 1, 1987).

150. Rand, H. W., Bovard, J. F. & Minnich, D. E. Localization of Formative Agencies in Hydra. *Proceedings of the National Academy of Sciences of the United States of America* **12,** 565–570 (Sept. 1926).

151. Engel, U. *et al.* Nowa, a novel protein with minicollagen Cys-rich domains, is involved in nematocyst formation in Hydra. *Journal of Cell Science* **115,** 3923–3934 (Pt 20 Oct. 15, 2002).

152. David, C. N. & Campbell, R. D. Cell cycle kinetics and development of Hydra attenuata. I. Epithelial cells. *Journal of Cell Science* **11,** 557–568 (Sept. 1972).

153. Miljkovic-Licina, M., Chera, S., Ghila, L. & Galliot, B. Head regeneration in wild-type hydra requires de novo neurogenesis. *Development (Cambridge, England)* **134,** 1191–1201 (Mar. 2007).

154. Hausman, R. E. & Burnett, A. L. The mesoglea of Hydra. IV. A qualitative radioautographic study of the protein component. *Journal of Experimental Zoology* **177,** 435–446 (1971).

155. Shimizu, H. *et al.* Epithelial morphogenesis in hydra requires de novo expression of extracellular matrix components and matrix metalloproteinases. *Development* **129,** 1521–1532 (Mar. 15, 2002).

156. Hufnagel, L. A., Kass-Simon, G. & Lyon, M. K. Functional organization of battery cell complexes in tentacles of Hydra attenuata. *Journal of Morphology* **184,** 323–341 (1985).

157. Hufnagel, L. A. & Myhal, M. L. Observations on a Spirochaete Symbiotic in Hydra. *Transactions of the American Microscopical Society* **96,** 406–411 (1977).

158. Dexter, J. P., Tamme, M. B., Lind, C. H. & Collins, E.-M. S. On-chip immobilization of planarians for in vivo imaging. *Scientific Reports* **4,** 6388 (Sept. 17, 2014).

159. Letizia, C. S., Cocchiara, J., Lalko, J. & Api, A. M. Fragrance material review on linalool. *Food and Chemical Toxicology: An International Journal Published for the British Industrial Biological Research Association* **41,** 943–964 (July 2003).

160. Nordt, S. P. Chlorobutanol toxicity. *The Annals of Pharmacotherapy* **30,** 1179–1180 (Oct. 1996).

161. Tuveson, D. A. & Jacks, T. Modeling human lung cancer in mice: similarities and shortcomings. *Oncogene* **18,** 5318–5324 (Sept. 20, 1999).

162. Salaman, M. H. & Roe, F. J. Incomplete carcinogens: ethyl carbamate (urethane) as an initiator of skin tumour formation in the mouse. *British Journal of Cancer* **7,** 472–481 (Dec. 1953).

163. Sakano, K., Oikawa, S., Hiraku, Y. & Kawanishi, S. Metabolism of carcinogenic urethane to nitric oxide is involved in oxidative DNA damage. *Free Radical Biology & Medicine* **33,** 703–714 (Sept. 1, 2002).

164. Bernardini, G., Vismara, C., Boracchi, P. & Camatini, M. Lethality, teratogenicity and growth inhibition of heptanol in Xenopus assayed by a modified frog embryo teratogenesis assay-Xenopus (FETAX) procedure. *The Science of the Total Environment* **151,** 1–8 (July 4, 1994).

165. Slooff, W., Canton, J. H. & Hermens, J. L. M. Comparison of the susceptibility of 22 freshwater species to 15 chemical compounds. I. (Sub)acute toxicity tests. *Aquatic Toxicology* **4,** 113–128 (Sept. 1, 1983).

166. Nogi, T. & Levin, M. Characterization of innexin gene expression and functional roles of gap-junctional communication in planarian regeneration. *Developmental Biology* **287,** 314–335 (Nov. 15, 2005).

167. Marcum, B. & Campbell, R. Development of Hydra lacking nerve and interstitial cells. *Journal of Cell Science* **29,** 17–33 (Feb. 1, 1978).

168. Elisabetsky, E., Marschner, J. & Souza, D. O. Effects of Linalool on glutamatergic system in the rat cerebral cortex. *Neurochemical Research* **20,** 461–465 (Apr. 1995).

169. Re, L. *et al.* Linalool modifies the nicotinic receptor-ion channel kinetics at the mouse neuromuscular junction. *Pharmacological Research* **42,** 177–182 (Aug. 2000).

170. Pierobon, P. *et al.* Biochemical and functional identification of GABA receptors in Hydra vulgaris. *Life Sciences* **56,** 1485–1497 (1995).

171. Bellis, S. L., Grosvenor, W., Kass-Simon, G. & Rhoads, D. E. Chemoreception in Hydra vulgaris (attenuata): initial characterization of two distinct binding sites for l-glutamic acid. *Biochimica et Biophysica Acta (BBA) - Biomembranes* **1061,** 89–94 (Jan. 9, 1991).

172. Kass-Simon, G., Pannaccione, A. & Pierobon, P. GABA and glutamate receptors are involved in modulating pacemaker activity in hydra. *Comparative Biochemistry and Physiology. Part A, Molecular & Integrative Physiology* **136,** 329–342 (Oct. 2003).

173. Kass-Simon, G. & Scappaticci, A. A. Glutamatergic and GABAnergic control in the tentacle effector systems of Hydra vulgaris. *Hydrobiologia* **530,** 67–71 (Nov. 1, 2004).

174. Eržen, I. & Brzin, M. Cholinergic mechanisms in hydra. *Comparative Biochemistry and Physiology Part C: Comparative Pharmacology* **59,** 39–43 (Jan. 1, 1978).

175. Kass-Simon, G. & Passano, L. M. A neuropharmacological analysis of the pacemakers and conducting tissues ofHydra attenuata. *Journal of comparative physiology* **128,** 71–79 (Mar. 1, 1978).